

UNIVERSITY OF CALIFORNIA SAN DIEGO

Small-Scale Oceanic Variability from Satellite Altimetry

A dissertation submitted in partial satisfaction of the  
requirements for the degree  
Doctor of Philosophy

in

Earth Sciences

by

Yao Yu

Committee in charge:

Professor David T. Sandwell, Chair  
Professor Sarah T. Gille, Co-Chair  
Professor Duncan C. Agnew  
Professor Matthias Morzfeld  
Professor Julian J. McAuley

2023

Copyright

Yao Yu, 2023

All rights reserved.

The Dissertation of Yao Yu is approved, and it is acceptable in quality and form for publication on microfilm and electronically.

University of California San Diego

2023

## DEDICATION

This dissertation is dedicated to my nainai.



## EPIGRAPH

When you meet a virtuous person,  
think of becoming like them;  
when you meet an unvirtuous person,  
reflect on your own faults.

*Confucius*

Stay hungry.  
Stay foolish.

*Steve Jobs*

If you shut the door to all errors,  
truth will be shut out.

*Rabindranath Tagore*

I'm just like my country  
I'm young, scrappy, and hungry,  
and I am not throwing away my shot.

*Hamilton musical*

## TABLE OF CONTENTS

Dissertation Approval Page .....	iii
Dedication .....	iv
Epigraph .....	v
Table of Contents .....	vi
List of Figures .....	viii
List of Figures .....	viii
List of Tables .....	xv
List of Tables .....	xv
Preface .....	xvi
Acknowledgements .....	xvii
Vita .....	xviii
Abstract of the Dissertation .....	xx
Chapter 1     Introduction .....	1
Chapter 2     Assessment of ICESat-2 for the Recovery of Ocean Topography .....	11
2.1     Introduction .....	12
2.2     Wavenumber Domain Analysis .....	15
2.3     Space Domain Analysis .....	20
2.3.1     Long Wavelength Mean Sea Surface .....	20
2.3.2     Short Wavelength: Surface Gravity Waves .....	21
2.3.3     Sea Level Anomalies at Wavelengths >3 km .....	27
2.4     Discussion and Conclusions .....	35
2.5     Acknowledgements .....	37
2.6     Appendix .....	38
Chapter 3     Global Mesoscale Ocean Variability from Multi-Year Altimetry: an Analysis of the Influencing Factors .....	40
3.1     Introduction .....	41
3.2     Data and Methods .....	45
3.2.1     Data .....	45
3.2.2     Methods .....	55
3.3     Results .....	60

3.3.1	Correlation with Roughness .....	60
3.3.2	Predicted SSS Variability .....	62
3.3.3	Feature Importance .....	66
3.4	Discussion and Conclusions .....	69
3.5	Acknowledgements .....	74
3.6	Appendix .....	76
Chapter 4	Seasonality of the Sub-Mesoscale to Mesoscale Sea Surface Variability from Multiple Satellite Altimetry .....	79
4.1	Introduction .....	80
4.2	Datasets .....	83
4.2.1	Sea Surface Slope from Altimetry .....	83
4.2.2	Impacts from Wave Height Noise .....	85
4.2.3	Sea Surface Slope from llc4320 .....	90
4.2.4	Surface Wind Speed .....	90
4.2.5	Thermocline Depth .....	91
4.3	Results .....	91
4.3.1	Seasonality: Annual Variability .....	91
4.3.2	Seasonality: Semi-Annual Variability .....	94
4.3.3	Seasonality: Assessment .....	96
4.3.4	Spectral analysis .....	97
4.3.5	Impacts from SWH .....	100
4.4	Discussion and Conclusions .....	102
4.4.1	Interpretation of the Mean SSS .....	104
4.4.2	Interpretation of the Annual SSS .....	104
4.4.3	Interpretation of the Semi-Annual SSS .....	107
4.4.4	Future Work Needed to Resolve These Issues .....	108
4.5	Acknowledgements .....	108
4.6	Appendix .....	110
Chapter 5	Future work .....	116
5.1	High-resolution small-scale variability at the Foundation Seamounts from SWOT .....	116
5.1.1	First glimpses of SWOT images .....	116
5.1.2	Foundation Seamounts investigation plan .....	118
5.2	Tidal conversion over rough topography .....	119
5.2.1	Motivation .....	119
5.2.2	Research plan .....	120
Bibliography	.....	122
Bibliography	.....	122

## LIST OF FIGURES

Figure 1.1.	Time and space scales of physical oceanographic phenomena from bubbles and capillary waves to changes in ocean circulation associated with Earth's orbit variations. Credit: Talley 2011. ....	2
Figure 1.2.	Altimeter satellite missions' timeline overview along with the missions' orbit reportativity and information about their countries of origin. Cited from Grgić and Bašić, 2021. ....	3
Figure 1.3.	Principle of Satellite Altimeter (Courtesy of AVISO).....	4
Figure 1.4.	This graphic shows the six-beam pattern from the Advanced Topographic Altimeter System (ATLAS) instrument and how it measures ice thickness. Each pair consists of a strong and weak beam, with an energy ratio of about 4:1. The beams are separated by 90 meters in the cross-track direction and approximately 2.5 kilometers in the along-track direction. The three beam pairs are 3.3 kilometers apart in the cross-track direction. The photon beams that reflect from the ocean surface provide estimates of height above a reference ellipsoid, with a horizontal accuracy of 10 meters and a vertical precision of 0.03 meters. ICESat-2 has a high sampling rate of 10 kHz, a narrow footprint of 15 meters in diameter, near-global coverage with a 92° inclination, and a 91-day repeat. Credit: Smith et al., 2020. ....	7
Figure 1.5.	The configuration of the measurement system of the SWOT mission. The red and blue dashed lines represent the path of the transmission and reception of radar signals, respectively, over the two 50-km-wide swaths for interferometry between the two interferometer antennas. The green dashed lines represent the reception of radar signals near the nadir for interferometry between the nadir altimeter antenna and one of the interferometer antennas for observing the near-nadir regions where the targets have nearly equal distance to the two interferometer antennas. Both swaths have the same capability of making observations either over the ocean or the land surface water. (cited from Fu and Ubelmann, 2014) .....	10
Figure 2.1.	Averaged SSH power spectral density in the Pacific box. The spectrum can be divided into three bands representing long wavelength MSS signals (20-500 km), surface gravity waves (<3 km), and the more poorly understood intermediate wavelength band (3-20 km). The 99% confidence interval is shaded in red. ....	16

Figure 2.2.	(a) CMS and (c) phase between beams 11-21, 21-31, 11-31 of a selected ICESat-2 track (ground track: 0394, cycle: 02). CMS falls to below 95% CL at $\sim 25$ km. (b) CMS and (d) phase between MSS and each strong beam. Black line is the spectral CMS and phase between 20Hz Jason-2 and MSS. CMS falls to below 95% CL at $\sim 20$ km for both the ICESat-2 and the Jason-2 cases. ....	18
Figure 2.3.	(a) SSH of ICESat-2 3 strong beams (ground track: 0394, cycle: 02) along with MSS at beam 21's position. Data are low-pass filtered at 20 km, and the linear trend of beam 21 has been removed from all four height series. The MSS is offset for plotting. (b) a shorter segment with no MSS offset. Tracks run almost north-south so $1^\circ$ in latitude corresponds to $\sim 110$ km along track. ....	21
Figure 2.4.	(a) SLA of ICESat-2 3 strong beams (ground track: 0394, cycle: 02). (b) a shorter segment of (a) showing peak to trough variations having wavelengths of a few hundreds of meters. Tracks run almost N-S so $1^\circ$ corresponds to $\sim 110$ km along track and each $0.002^\circ$ grid in (b) is about 200 m. ....	22
Figure 2.5.	(a) SWH calculated from 3-km-running standard deviation of SLA from ICESat-2 3 strong beams (ground track: 0394, cycle: 02). Background light dots are SWH before filtering and darker lines are low-pass filtered at 6 km so that they resemble the 1Hz averaged SWH in radar altimetry. (b) a shorter segment of (a). Tracks run almost N-S so $1^\circ$ corresponds to $\sim 110$ km along track. ....	23
Figure 2.6.	(a) a small segment of ICESat-2 photon height data w.r.t WGS 84. (ground track: 0326, cycle: 01). The strong and weak beams are separated by 90 m and both are low-pass filtered at 30 m. (b) CMS and (c) phase between beams 11 and 1r. Coherence peaks around 465 m, and the corresponding phase shift is $-70.3^\circ$ . The 99% and 95% CL are labeled. ....	25
Figure 2.7.	Joint probability histograms for (a) wavelength, (b) wave directions and (c) SWH of WAVEWATCH III (WW3) predictions and ICESat-2 (IS2) reconstructions. The black dotted line is the 1:1 relationship and the red line is the best fitted slope. Histogram of (d) wavelength, (e) direction and (f) SWH differences between IS2 reconstructions and WW3 predictions. The mean $\mu$ and RMSE of wavelength/direction/SWH differences are shown in (d)-(f). ....	27
Figure 2.8.	(a) Low-pass filtered (3 km and sampled at 50 m) SLA. Missing data were not included in the filter. (b) a shorter segment of (a). Tracks run almost N-S so $1^\circ$ corresponds to $\sim 110$ km along track. ....	28

- Figure 2.9. (a) Directional spectrum from CDIP station Point Reyes at time: 2019-09-29, 19:00 UTC. Energy density is in dB so as to show a large range of energy levels. The directional spectrum was computed using the maximum entropy method (Lygre and Krogstad, 1986). ICESat-2 orbit inclination is  $92^\circ$  and here we show a synthetic descending track (in red). Panel (b) gray: along-track PSD; blue: true PSD. Both are derived from the directional spectrum in (a). ..... 32
- Figure 2.10. (a) Synthetic SLA using CDIP directional spectrum in Figure 2.9a and the positions of ICESat-2 track (ground track: 0394, cycle: 02). (b) 3 km low-pass filtered synthetic SLA for a 100-km segment. .... 33
- Figure 2.11. Averaged power spectral density of ICESat-2 sea level anomaly (w.r.t. to the mean sea surface) in a Pacific box  $[-120^\circ/-100^\circ/-11^\circ/-1^\circ]$  using the Lomb-Scargle method. This analysis uses 341 strong beams having more than 70 % cloud-free data. ICESat-2 photon height data are first low-pass filtered at 30 m. Vertical dashed lines indicate the separations between the three bands considered in this paper: large-scale flows (20-500 km), the shorter wavelength gravity waves ( $< 3$  km) and the more poorly understood intermediate wavelength (3-20 km) band. The  $k^{-1}$  and  $k^{-2}$  spectral slopes are labeled. The relative flat spectral slopes suggest that the long wavelength band is dominated by unbalanced flows and internal tides. 38
- Figure 2.12. Sketch of a pair of ICESat-2 descending beams (flying from  $\theta = 2^\circ$ ) and a wave coming from southwest, forming an angle  $\alpha$ . Beam l and beam r are separated by a cross-track distance  $d$  of 90 m. The wavelength  $L_0$  is projected to be  $L' = L_0/|\cos \alpha|$  in the orbit direction. The wave in the observation of beam l leads beam r by a phase shift  $\beta$ , where  $\beta = 360^\circ d |\tan \alpha| / L' = 360^\circ d |\sin \alpha| / L_0$ . The true wavelength  $L_0$  and wave direction  $\theta = \alpha + \theta_0$  could be reconstructed from the projected wavelength  $L'$  and phase shift  $\beta$ , though comes with a  $180^\circ$  ambiguity. The along-track distance between beam l and beam r is about 2.5 km, which corresponds to  $\sim 0.35$  s shift in time during which surface waves only travel a few meters. This time shift appears in the coherence as a phase offset between the strong and weak beams. We neglected this phase offset and identified it as errors in the wave reconstruction. The  $\sim 2.5$  km along-track offset between the strong and weak beams is not shown here. There are 4 cases with the combination of ascending/descending track and beam l leads/lags beam r. Here we illustrate the descending track, with beam l leading beam r. The wave reconstruction scheme for the other three could be similarly derived. .... 39

Figure 3.1.	(a) Mesoscale SSS variability (30-100 km). (b) large-scale SSS variability (>100 km). 1 microradian equals 1 cm change in height over a horizontal distance of 10 km. All plots are at 7 by 5 arc minute resolution using a Mercator projection. All land is gray. Note that the color scales for (a) and (b) are different. ....	47
Figure 3.2.	Normalized environmental parameters used in this study. Land is masked as light gray. All areas excluded (lakes, ponds, inland ocean and coastal areas) are masked as dark gray. All plots are at 7 by 5 arc minute resolution using a Mercator projection. ....	55
Figure 3.3.	Correlation coefficients of seafloor roughness versus SSS variability in three wavelength bands (>30km or full band, 30-100km, > 100km) as a function of ocean depth. Black dashed lines are the 95% confidence intervals beyond which correlation coefficients are statistically reliable. ..	61
Figure 3.4.	(a) The predicted mesoscale SSS variability map (30-100km) and (b) the associated prediction error using the correlation between seafloor roughness and SSS variability (30-100km) as a function of seafloor depth. (c) and (d) are the same as (a) and (b) except for using the linear regression model. (e) and (f) are the same as (a) and (b) except for using the boosted trees model. Regions with prediction failures are enclosed in red boxes in (b), (d) and (e). ....	64
Figure 3.5.	(a) The predicted SSS variability map (>100km) and (b) the associated prediction error using the correlation between seafloor roughness and SSS variability (> 100 km) as a function of seafloor depth. (c) and (d) are the same as (a) and (b) except for using the linear regression model. (e) and (f) are the same as (a) and (b) except for using the boosted trees model. ....	66
Figure 3.6.	Ranks of features of the mesoscale SSS variability (30-100 km) from the linear regression model using the forward selection and the feature ablation; from the boosted trees model using the feature ablation and the feature importance returned by the model. Features with smaller ranks have higher importance. Features and their full name are introduced in Section 3.2.1. ..	67
Figure 3.7.	Same as Figure 3.6 but for ranks of features of the large-scale SSS variability (>100 km). ....	68
Figure 3.8.	Equal-area block separation. Each block is assigned with a unique ID from 0 to 63. The longitude (0° to 360 °) and latitude (-60 ° to 60 °) are linearly normalized to -1 and 1. ....	76

Figure 3.9.	The Pearson correlation coefficient for the mean significant wave height and the SSS variability in multiple sub-bands (10-15 km, 15-25 km, 25-39 km, 39-63 km, 63-100 km, 100-158 km, 158-251 km, 251-398 km, 398-630 km, 630-1000 km). A coefficient of $\pm 0.5$ means strong correlation. ....	77
Figure 3.10.	(a) The predicted SSS variability map (30-100km) and (b) the associated prediction error using the linear regression model with 27 features of random animals. (c) and (d) are the same as (a) and (b) except for using the boosted trees model. The MSE and $R^2$ for the linear regression model are $0.023 \mu\text{rad}^2$ and 0.080, for the boosted trees model are $0.018 \mu\text{rad}^2$ and 0.273. (e) The predicted SSS variability map (30-100km) and (f) the associated prediction error using the linear regression model with 27 features of random gaussian noise. (g) and (h) are the same as (e) and (f) except for using the boosted trees model. The MSE and $R^2$ for both models are $0.025 \mu\text{rad}^2$ and -0.007. ....	78
Figure 4.1.	(a) Long-term average significant wave height (SWH) is large in the Southern Ocean and high-latitude Northern Hemisphere. (b) SSS variability in the 10-15 km wavelength band shows similar patterns as (a), yet with more detailed patterns. (c) Correlation between average SWH and band-pass filtered SSS variability. Correlation is higher than 0.5 at wavelengths shorter than 30 km. Error bars indicate the 99% confidence interval. ....	87
Figure 4.2.	(a) SSS variability in the 100-158 km wavelength band shows high variability associated with western boundary currents and the Antarctic Circumpolar current. (b) SSS variability in the 39-63 km wavelength band shows high variability over mid-ocean ridges, large seamounts chains, trenches and the Amazon shelf. Regions masked out are in gray. (c) Locations of prominent bathymetric features mentioned in text. Land is in gray and blue shading illuminates ocean topography. ....	89
Figure 4.3.	(a) Amplitude and (b) phase for annual SSS variability in the 30-100 km wavelength band from satellite altimetry. (c) and (d) are the same as (a) and (b) but from the llc4320 output. (e) and (f) for are the annual amplitude and phase for the SWH. (g) and (h) are the annual amplitude and phase for the thermocline depth. Streak patterns in (e) and (f) are artifacts of the altimeter sampling patterns. Regions masked out are in gray. ....	93
Figure 4.4.	The amplitude (a) and phase (b) for semi-annual SSS variability in the 30-100 km wavelength band from satellite altimetry. Regions masked out are in gray. Panels (c) and (d) show the amplitude and phase along a meridional profile averaged over $150^\circ\text{W}$ to $90^\circ\text{W}$ as shown in the red boxes in (a) and (b). ....	96



Figure 4.5.	The PSD of the seasonal SSS variability in (a) the Kuroshio region; (b) the north Atlantic Ocean; (c) the California coast; (d) the Bay of Bengal; (e) the west of Australia; and (f) the Atlantic equatorial area. The 99% confidence intervals are provided at the center of each band. The $k$ and $k^2$ spectral slopes are indicated for reference. ....	99
Figure 4.6.	The normalized time series of the mean SSS variability (30-100 km, thick black line with rounds dots), SWH (blue line with triangle dots), WSP (orange line with round dots), and the thermocline depth (green line with triangle dots) in (a) the Kuroshio region; (b) the north Atlantic Ocean; (c) the California coast; (d) the Bay of Bengal; (e) the west of Australia; and (f) the Atlantic equatorial area. ....	101
Figure 4.7.	(a) Correlation between the mean SWH and mean band-pass filtered SSS (black curve); correlation between the annual amplitude of SWH and annual amplitude of the band-pass filtered SSS (red curve); (b) same as (a) but for the correlation between the thermocline depth and the SSS. Error bars indicate the 99% confidence interval. ....	106
Figure 4.8.	Mean SSS variability in the 10 sub-bands. ....	110
Figure 4.9.	The mean SSS variability in the 30-100 km wavelength band from (a) multi-year satellite altimetry along track data and (b) llc4320. The color scales are different. Llc4320 shows much smaller signals in general. Both show high variabilities in the western boundary currents, the north Atlantic ocean, and highly-stratified zones by river flows (Amazon outlet, Gulf of Bengal). Satellite altimetry shows strong variabilities over rough topography (Hawaiian Seamount chains, Mid-Atlantic Ocean Ridge) and the ITCZ which are missing in the llc4320. Llc4320 shows strong variability in several regions on the Pacific equatorial area (longitude centers are around $165^\circ$ E, $165^\circ$ W, $135^\circ$ W) that are invisible in the satellite altimetry results. ....	111
Figure 4.10.	The semi-annual (a) amplitude and (b) phase of the SSS variability from 30 km to 100km wavelength bands using llc4320 model outputs. ....	112
Figure 4.11.	Fractions of variance explained by the annual and semi-annual least-squares fit for 10 sub-bands. ....	113
Figure 4.12.	The annual amplitudes of SSS variability in the 10 sub-bands. Note the reduction in the color scale as the wavelength band increases. ....	114
Figure 4.13.	The semi-annual amplitudes of SSS variability in the 10 sub-bands. ....	115

Figure 5.1.	Sea level data gathered March 16, 2023 in the Gulf Stream by SWOT's KaRIn instrument, visualized at right, has 10 times the spatial resolution of data taken over the same area by altimeters on seven other satellites, visualized at right. Red represents sea levels higher than the global average, while blue is lower. Credit: left: NASA/JPL-Caltech/Copernicus Marine Service of ESA; right: NASA/JPL-Caltech. ....	117
Figure 5.2.	Same as Figure 5.1 but collected in January 21, 2023. Credit: left: NASA/JPL-Caltech/Copernicus Marine Service of ESA; right: NASA/JPL-Caltech. ....	117
Figure 5.3.	Bathymetry of Foundation seamounts first mapped in 1997 using multi-beam sonar (a) and shipboard gravity (b) (Maia et al., 2000). Many of these seamounts are more than 3000 m tall and produce gravity anomalies (b) and sea surface slopes of more than 100 mGal and 100 $\mu$ rad, respectively. The satellite-derived gravity (green) does not completely resolve the shipboard gravity (red) at the tops of the seamounts. The full amplitude gravity (and SSS) can be reconstructed using a combination of altimeter-derived gravity for wavelengths > 40 km and gravity calculated from the multibeam bathymetry for the shorter wavelengths (blue). Note the very small spatial scale wiggles in the ship data are errors due to unmodeled ship motions. .	119

## LIST OF TABLES

Table 4.1.	Sea Surface Slope Statistics .....	98
------------	------------------------------------	----

## PREFACE

Almost nothing is said in the manual about the preface. There is no indication about how it is to be typeset. Given that, one is forced to simply typeset it and hope it is accepted. It is, however, optional and may be omitted.

## ACKNOWLEDGEMENTS

David and Sarah lab mates SWOT group Ole Anderson, Walter Smith, Ed Zaron, Shengjun Zhang, Ana Beatriz Villas Bôas

field trips and cruise committee members, course instructors, Adrian Borsa, Wenyan Fan, Karen Scott, netops GMT, MATLAB, python, chatgpt scripps community friends family Hanna

Chapter 2, in full, is a reprint of the material as it appears in *Geophysical Journal International* 2021. Yu, Yao; Sandwell, David T.; Gille, Sarah T.; Villas Bôas, Ana Beatriz, Oxford University Press, 2021. The dissertation author was the primary author of this paper.

Chapter 3, in full, is a reprint of the material as it appears in *Artificial Intelligence for the Earth Systems*, 2022, Yu, Yao; Gille, Sarah T.; Sandwell, David T.; McAuley, Julian, American Meteorological Society, 2022. The dissertation author was the primary author of this paper.

Chapter 4, in full, is a reprint of the material as it appears in *Journal of Geophysical Research: Oceans*, 2022, Yu, Yao; Sandwell, David T.; Gille, Sarah T., 2022. The dissertation author was the primary author of this paper.

## VITA

April 6, 1994 Born, Dingyuan, Anhui, China

2015 Bachelor of Engineering, Wuhan University, China

2016-2018 Visiting student, Academia Sinica, Taiwan

2018 Master of Engineering, Wuhan University, China

2020 Master of Science, University of California, San Diego

2022 Teaching Assistant, Scripps Institution of Oceanography  
University of California, San Diego

2019–2023 Research Assistant, University of California, San Diego

2023 Doctor of Philosophy, University of California, San Diego

## PUBLICATIONS

Gevorgian, J., Sandwell, D. T., **Yu, Y.**, Kim, S. S., Wessel, P. (2023). Global distribution and morphology of small seamounts. *Earth and Space Science*, 10(4), e2022EA002331.

**Yu, Y.**, Sandwell, D. T., Gille, S. T. (2022). Seasonality of the Sub-mesoscale to Mesoscale Sea Surface Variability from Multi-Year Satellite Altimetry. *Journal of Geophysical Research: Oceans*, e2022JC019486.

**Yu, Y.**, Gille, S. T., Sandwell, D. T., McAuley, J. (2022). Global Mesoscale Ocean Variability from Multiyear Altimetry: An Analysis of the Influencing Factors. *Artificial Intelligence for the Earth Systems*, 1(3), e210008.

Sandwell, D. T., Goff, J. A., Gevorgian, J., Harper, H., Kim, S. S., **Yu, Y.**, Tozer, B., Wessel, P., Smith, W. H. (2022). Improved bathymetric prediction using geological information: SYNBATH. *Earth and Space Science*, 9(2), e2021EA002069.

**Yu, Y.**, Sandwell, D. T., Gille, S. T., Villas Bôas, A. B. (2021). Assessment of ICESat-2 for the recovery of ocean topography. *Geophysical Journal International*, 226(1), 456-467.

Chao, B. F., **Yu, Y.** (2020). Variation of the equatorial moments of inertia associated with a 6-year westward rotary motion in the Earth. *Earth and Planetary Science Letters*, 542, 116316.

Chao, B. F., **Yu, Y.**, Chung, C. H. (2020). Variation of Earth's oblateness  $J_2$  on interannual-to-decadal timescales. *Journal of Geophysical Research: Solid Earth*, 125(6), e2020JB019421.

Tanaka, Y., **Yu, Y.**, Chao, B. F. (2019). Gravity and geoid changes by the 2004 and 2012 Sumatra earthquakes from satellite gravimetry and ocean altimetry. TAO: Terrestrial, Atmospheric and Oceanic Sciences, 30(4), 5.

**Yu, Y.**, Chao, B. F., García-García, D., Luo, Z. (2018). Variations of the Argentine Gyre observed in the GRACE time-variable gravity and ocean altimetry measurements. Journal of Geophysical Research: Oceans, 123(8), 5375-5387.

## FIELDS OF STUDY

Major Field: Earth Sciences

Studies in geophysics  
Professors David Sandwell and Duncan Agnew

Studies in physical oceanography  
Professor Sarah Gille

Studies in computer sciences  
Professor Julian McAuley

## ABSTRACT OF THE DISSERTATION

Small-Scale Oceanic Variability from Satellite Altimetry

by

Yao Yu

Doctor of Philosophy in Earth Sciences

University of California San Diego, 2023

Professor David T. Sandwell, Chair

Professor Sarah T. Gille, Co-Chair

Satellite altimetry has revolutionized our understanding of upper-ocean circulation dynamics and sea level change. However, there is limited understanding of sub-mesoscale to mesoscale ocean dynamics because they are too small to be detected globally with today's technology. Mesoscale ocean activities are associated with eddy kinetic energy generation and dissipation, and play an important role in the dynamics of ocean energy transfer and mixing (Ferrari and Wunsch, 2009) and local and global budgets of heat and carbon (Morrow et al., 2019). The Surface Water and Ocean Topography (SWOT) satellite altimetry mission, launched in December 2022, will provide an opportunity to refine the measured sea surface height resolu-



tion down to 15 km, allowing for direct global observations of mesoscale oceanic activity. This new capability motivates investigations of submesoscale to mesoscale oceanic activities, and the separation between balanced geostrophic flows and unbalanced wave motions. This thesis uses the ICESat-2 photon height data and radar altimetry data collected over the past thirty years to study small-scale ocean surface variability, its influencing factors, and seasonality. The results in Chapter 2 show that an ICESat-2 single track can recover the marine geoid at wavelengths  $> 20$  km, which is similar to the best radar altimeter data. However, the wavelength and propagation direction of surface gravity waves are sometimes well resolved by using a combination of the strong and weak beams, which are separated by 90 m. In Chapter 3, we identify the most important factors that influence mesoscale ocean variability to be the distance to the nearest thermocline boundary, significant wave height, mean dynamic topography gradient, and M2 tidal speed. Nonetheless, some regions such as the Amazon outflow cannot be predicted by the model, suggesting that these regions are governed by local processes not represented in the input features. In Chapter 4 we found that the high-latitude Northern Hemisphere and the south Indian Ocean are associated with large annual cycles at mesoscales. The variability is higher in local wintertime, except for a few regions such as the Bay of Bengal, which shows high variability in the boreal spring and fall.

# Chapter 1

## Introduction

The ocean serves as the primary repository of the Earth's heat and carbon dioxide. Advances in Earth-observing satellite technology have revealed crucial connections between climate change and the ocean. Sea level rise is one of the most widely studied and discussed phenomena within the context of climate change. The rate of sea level rise varies from region to region and is related to thermal expansion, melting of ice sheets and glaciers and ocean mass redistribution, geological patterns, and ocean/atmospheric dynamics (Kopp et al., 2015).

Ocean dynamics have a wide range of temporal and spatial scales (Figure 1.1). At the smallest scales, molecular mixing occurs. When winds blow over the ocean surface, capillary waves are generated at the scale of centimeters, which can grow into surface gravity waves with wavelengths ranging from tens to a few hundreds of meters. These waves can be short-period, locally generated wind seas, occurring in all directions, or propagating over long distance developing into long-period, narrow-banded swells. Surface gravity waves can reach heights of several meters, making them a major source of error in radar altimetry observations. At submesoscales to mesoscales, (including the 30-100 km range which is the focus of this dissertation), there are internal waves and tides, as well as instabilities of currents such as eddies, fronts, and meanders. Internal gravity waves are characterized by water parcels oscillating in stratified water, with restoring by the buoyancy force. They are typically generated by tides interacting with rough

topography or by winds stirring the mixed layer, producing internal waves with near-tidal or near-inertial frequency. Strong ocean currents such as the Gulf Stream have spatial scales of hundreds of kilometers and are balanced by the Coriolis force and pressure gradient force. Small pockets of water breaking off from the main body of a current may form eddies, fronts, or meanders, having scales on  $O(100\text{km})$  and traveling for months across thousands of kilometers. Ocean general circulation represents the time-mean features of the ocean, with basin to global spatial scales. These features are major errors in constructing a marine gravity field.

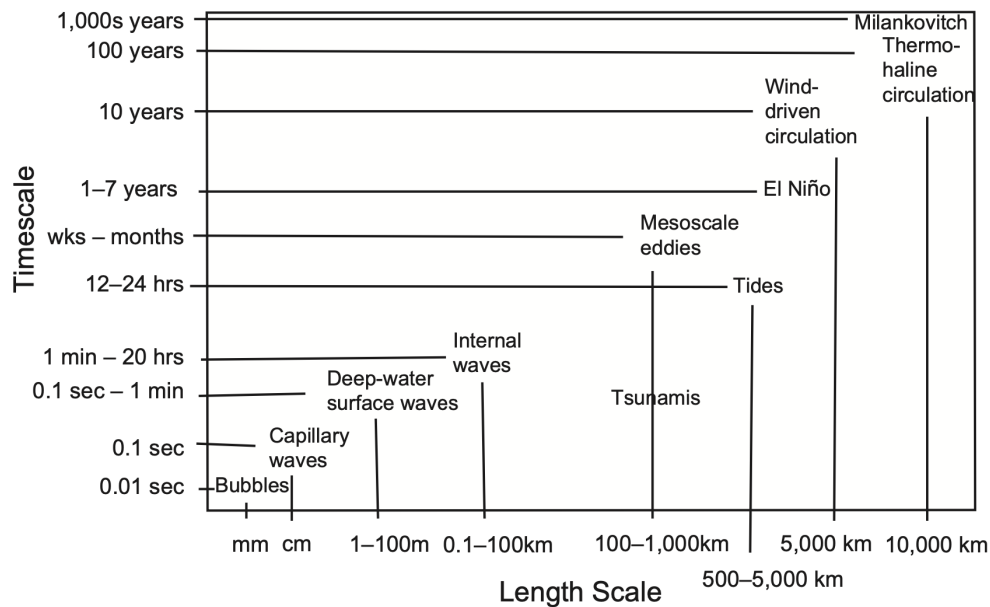


**Figure 1.1.** Time and space scales of physical oceanographic phenomena from bubbles and capillary waves to changes in ocean circulation associated with Earth’s orbit variations. Credit: Talley 2011.

Since the 1990s, satellite altimetry has been providing continuous global measurements of the sea surface height (SSH), greatly advanced our understanding of ocean dynamics, climate variability, weather forecasting and marine navigation (Fu and Cazenave, 2000; Nerem et al., 2018; Schiller and Brassington, 2011). The first successful satellite altimetry mission SEASAT was launched in 1978. This mission provided the first global map of SSH, followed by GEOSAT

and ERS-1, which provided improved accuracy and precision. The modern era of satellite radar altimetry started with the launch of TOPEX/Poseidon in 1992, and was followed by Jason 1/2/3, Envisat, Cryosat-2, SARAL/ALtiKa and Sentinel-3A/B, HY-2, and Sentinel-6 (see Figure 1.2).

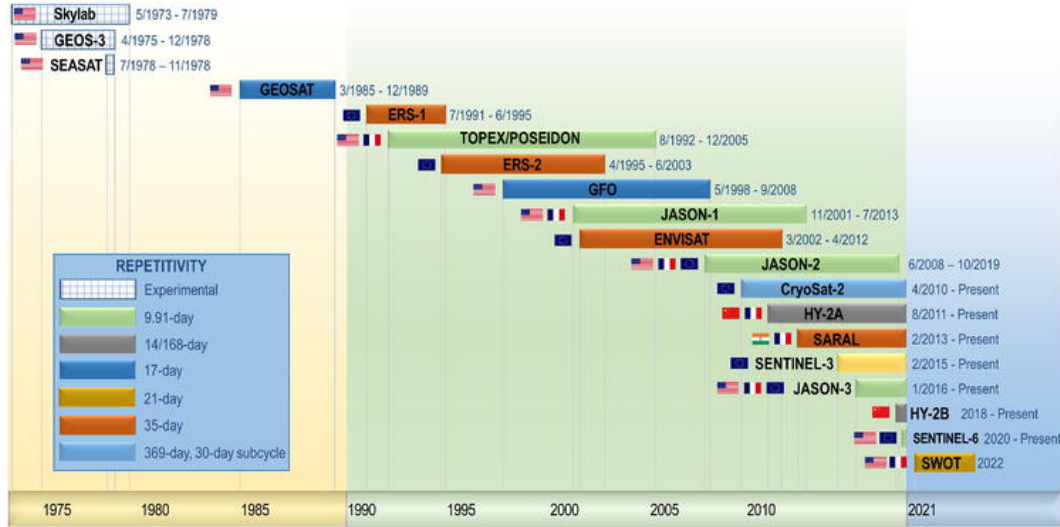


**Figure 1.2.** Altimeter satellite missions' timeline overview along with the missions' orbit reportativity and information about their countries of origin. Cited from Grgić and Bašić, 2021.

The fundamental principle of satellite altimetry is based on the transmission of a radar pulse from the satellite antenna to the Earth's surface. Upon reflection from the surface, the pulse is detected by the satellite receiver, and the time taken for the pulse to travel provides the range between the satellite and the ocean surface, as illustrated in Figure 1.3. The GPS tracking systems provide the altitude of the satellite with reference to a particular standard surface, typically the WGS84 ellipsoid. The SSH can be determined by subtracting the altimeter range from the satellite altitude, taking into account the geophysical corrections. The SSH represents the sum of the time-invariant marine geoid, dynamic ocean variabilities, and tides. The geoid is an equipotential surface of the Earth's gravity field, representing the non-uniform mass distribution of the Earth's interior. Barotropic ocean tides are generally well modeled in the open ocean (RMS error < 5cm) and less well modeled at coasts (RMS error < 10 cm) (Lyard et al., 2021; Stammer et al., 2014). For recovery of a static marine gravity field or predicting

the bathymetry, the critical measurement is the slope of the ocean surface (Sandwell and Smith, 2005), where the largest error comes from the satellite altitude measurement and wave height noise. To analyze oceanic dynamics, it is necessary to subtract the mean sea surface (MSS), which represents the geoid and the mean dynamic topography, from the satellite measurement.

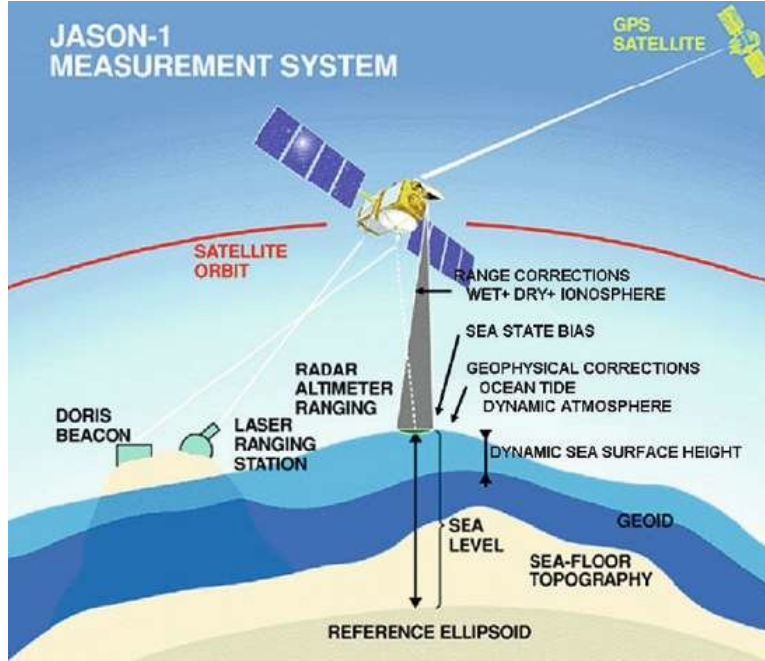


**Figure 1.3.** Principle of Satellite Altimeter (Courtesy of AVISO).

Ocean dynamics in the sub-mesoscale to mesoscale range, here defined as in 30-100 km wavelength band, are poorly understood because they are shorter than the  $O(100\text{km})$  spatial resolution of the most commonly used gridded multi-mission SSH products distributed by Copernicus Marine Environment Monitoring Service (CMEMS) (Le Traon et al., 1998; Le Traon and Dibarboure, 1999). The multi-mission SSH has a temporal resolution of  $\sim 10$  days and spatial resolution of 100-200 km, restricted by measurement noise and the wide separation between nadir tracks (Ballarotta et al., 2019; Taburet et al., 2019). High-resolution ocean general circulation models with  $\sim 2\text{km}$  spatial-resolution (Marshall et al., 1997b; Shchepetkin and McWilliams, 2005; Chassignet et al., 2003) generally lack surface wave forcing and have weak constraints of

large-scale features. Thus they cannot produce realistic realizations in this band. Ocean activities in this band are associated with the generation and dissipation of eddy kinetic energy, and contain most of the energy that powers ocean energy transfer and mixing (Ferrari and Wunsch, 2009), and local and global budgets of heat and carbon (Morrow et al., 2019). Ocean currents and eddies at these scales are important to coastal processes such as ship navigation, beach erosion, and dispersing pollutants. Therefore, this dissertation aims to narrow the research gaps in our understanding of sub-mesoscale to mesoscale ocean variability, and answer the following questions:

1. how well can we observe and understand sub-mesoscale to mesoscale ocean dynamics?
2. what are the driving forces of the ocean dynamics in this band?
3. what are the seasonal ocean dynamics in this wavelength band?

The main objective of this dissertation is to utilize satellite altimetry data to observe and examine changes in the sea surface resulting from ocean dynamics in the 30-100 km wavelength band. I use photon height data from the ICESat-2 (Ice, Cloud, and land Elevation Satellite-2) laser altimetry mission to explore its potential in reconstructing ocean topography. I also use 30 years of high-quality, repeated and non-repeated satellite radar altimetry data, to generate maps of sea surface variability with a spatial resolution of approximately 10 km and explore the seasonal variability. There are two critical components to our radar altimetry data analysis that enable the observation of small-scale ocean variability. The first is the two-step retracking of the raw waveform data from low-resolution mode (LRM) altimeters, where the footprint is circular and several kilometers in diameter. This technique improves the range precision and reduces the noise in the 10-45 km wavelength band by a factor of 1.5–1.7 (Zhang and Sandwell, 2017). This improves the along-track resolution. The second is the use of altimeter data with smaller cross-track spacing than that is normally used for oceanographic studies. These data were collected by Cryosat-2, SARAL/Altika and Jason-1/2 during their extended life phases. Using these improved data, I investigate the primary factors influencing ocean variability in

the 30-100 km band, along with its mean, annual, and semi-annual variations. The wide-swath SWOT (Surface Water and Oceanography Topography) mission, launched on December 16, 2022, will provide unprecedented details in measuring the world's surface water, both on land and in the ocean.

This dissertation comprises five chapters. This chapter serves as an introduction to the key concepts and altimeter data employed in this dissertation. In Chapter 2, I investigate the potential of ICESat-2 for measuring ocean topography and individual surface waves. Additionally, I highlight the challenges posed by one-dimensional observations of two-dimensional ocean surfaces. In Chapter 3, I present small-scale ocean variability maps constructed using satellite altimetry measurements. Furthermore, I employ machine learning techniques to identify the critical influencing factors of small-scale ocean dynamics. Chapter 4 explores the seasonal variations of ocean dynamics and establishes that they are related to changes in SWH and thermocline depth. In Chapter 5, I outline the future work, introducing the investigation of SWOT data to be collected over the Foundation Seamounts and the tidal conversion over rough topography.

Chapter 2 of this dissertation explores the potential of ICESat-2 in measuring the ocean topography and surface waves. ICESat-2 is a NASA laser altimetry mission that was launched in September 2018. It utilizes lidar tracks with a very fine spatial resolution of approximately 15 meters to measure the topography of ice, water, and land surfaces elevations. The mission's primary instrument is the Advanced Topographic Laser Altimeter System (ATLAS), which splits the green laser into six beams arranged in three pairs (refer to Figure 1.4). Compared to radar altimeters, which have a footprint of 5-10 kilometers, ICESat-2 has the ability to measure individual sea surface waves and reveal much higher resolution 1-D profiles of the ocean surface. Our results show that: (i) an ICESat-2 single track can recover the marine geoid at wavelengths  $>20$  km which is similar to the best radar altimeter data; (ii) the wavelength and propagation direction of the dominant surface gravity waves are sometimes well resolved by using a combination of the

strong and weak beams; (iii) there is higher than expected power in the 3-20 km wavelength band where geoid and ocean signals should be small. This artificial power is caused by the projection of 2-D surface waves with  $\sim 300$  m wavelengths into longer wavelengths (5-10 km) because of the 1-D sampling along the narrow ICESat-2 profile. Thus ICESat-2 will not provide major improvements to the geoid recovery in most of the ocean.

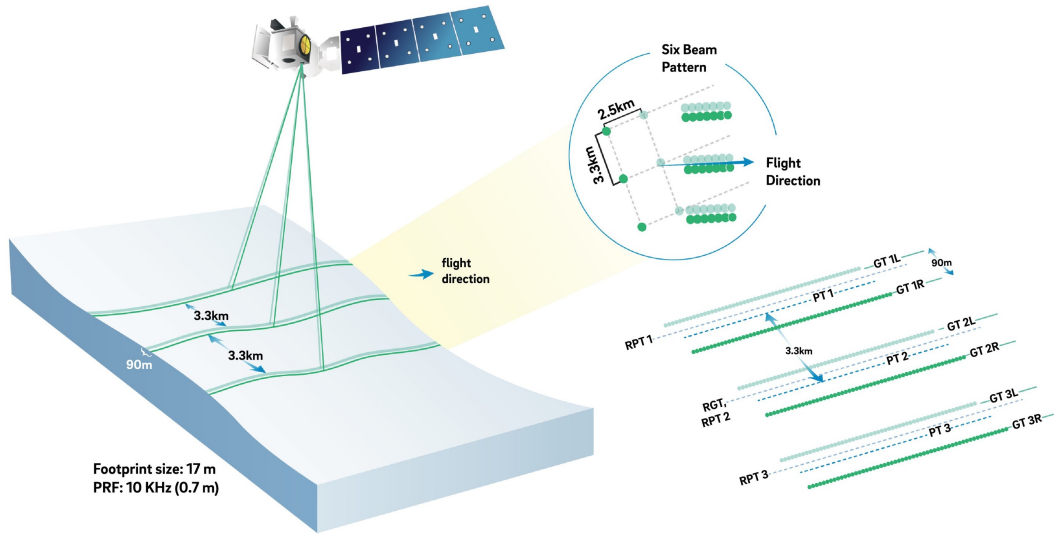


**Figure 1.4.** This graphic shows the six-beam pattern from the Advanced Topographic Altimeter System (ATLAS) instrument and how it measures ice thickness. Each pair consists of a strong and weak beam, with an energy ratio of about 4:1. The beams are separated by 90 meters in the cross-track direction and approximately 2.5 kilometers in the along-track direction. The three beam pairs are 3.3 kilometers apart in the cross-track direction. The photon beams that reflect from the ocean surface provide estimates of height above a reference ellipsoid, with a horizontal accuracy of 10 meters and a vertical precision of 0.03 meters. ICESat-2 has a high sampling rate of 10 kHz, a narrow footprint of 15 meters in diameter, near-global coverage with a  $92^\circ$  inclination, and a 91-day repeat. Credit: Smith et al., 2020.

Chapter 3 of this dissertation utilizes satellite radar altimetry waveform data collected over the past three decades to create sea surface slope (SSS) maps. SSS is the spatial derivative of SSH. Computing the spatial derivative enhances high-wavenumber signals and “whitens” the power spectral density (PSD) by  $k^2$ . We focus on focus on small resolvable scales in the 30-100 km wavelength band and use machine learning algorithms to identify the environmental



factors that influence the SSS variability. We identify the dominant factors to be the distance to the nearest thermocline boundary, significant wave height (SWH), mean dynamic topography gradient, and M2 tidal speed. However, there are individual regions, such as, the Amazon outflow, that cannot be predicted by our model, suggesting that these regions are governed by processes that are not represented in our input features. This study highlights both the value of machine learning and its shortcomings in identifying mechanisms governing oceanic phenomena.

Chapter 4 of this dissertation explores the seasonal variability of the SSS variability in the 30-100 km band using satellite altimetry data. We derive the mean, annual, and semi-annual components of SSS variability in multiple wavelength sub-bands from 10 to 1,000 km. The results show that: (i) the seasonal components are generally small ( $<10\%$  in amplitude) compared to the mean variability; (ii) at the 30–100 km wavelength band, there is high variability over western boundary currents and regions of rough topography. In this band, the high-latitude Northern Hemisphere and the south Indian Ocean are associated with large annual cycles; (iii) the variability is higher in local wintertime except for a few regions, for example, the Bay of Bengal, which shows high variability in the boreal spring and fall; (iv) through power spectral density analysis of the seasonal SSS variability, we find that the energy differences between local winter and summer are stronger at smaller scales ( $<100$  km).

Chapter 5 of this dissertation introduces two future projects, focusing on SWOT data analysis and the tidal conversion over the Foundation Seamounts. This chapter also presents the preliminary data from the SWOT mission, showing details of the Gulf Stream in ways that satellite radar altimetry could not before. SWOT is a collaborative effort between NASA, the French space agency CNES, in partnership with the Canadian Space Agency and UK Space Agency, and is designed to provide high-resolution measurements of water surface elevation and its associated properties, with the aim of providing new insights into the dynamics of the world's water cycle, including how water is stored, transported, and exchanged between the oceans,

atmosphere, and land. The wide-swath SWOT system is designed to measure the elevation of water surfaces over a swath of approximately 120 km in width at 21-day repeat. The principal instrument on SWOT is a Radar Interferometer (KaRIn, 0.86 cm wavelength) which is a Ka-band ( 0.86 cm wavelength) SAR system with two antennas at each end of a 10-m long baseline. The observation geometry is illustrated in Figure 1.5. The SWOT KaRIn system operates by transmitting two radar signals at slightly different frequencies. The returning radar signals arrive at each antenna slightly out of phase and the phase difference between the two signals is measured by the interferometer, which can then be used to calculate the surface height with a very high degree of accuracy. Early commissioning phase shows that SWOT is able to measure rivers  $> 100$  m and ocean dynamics above 15 km wavelengths.

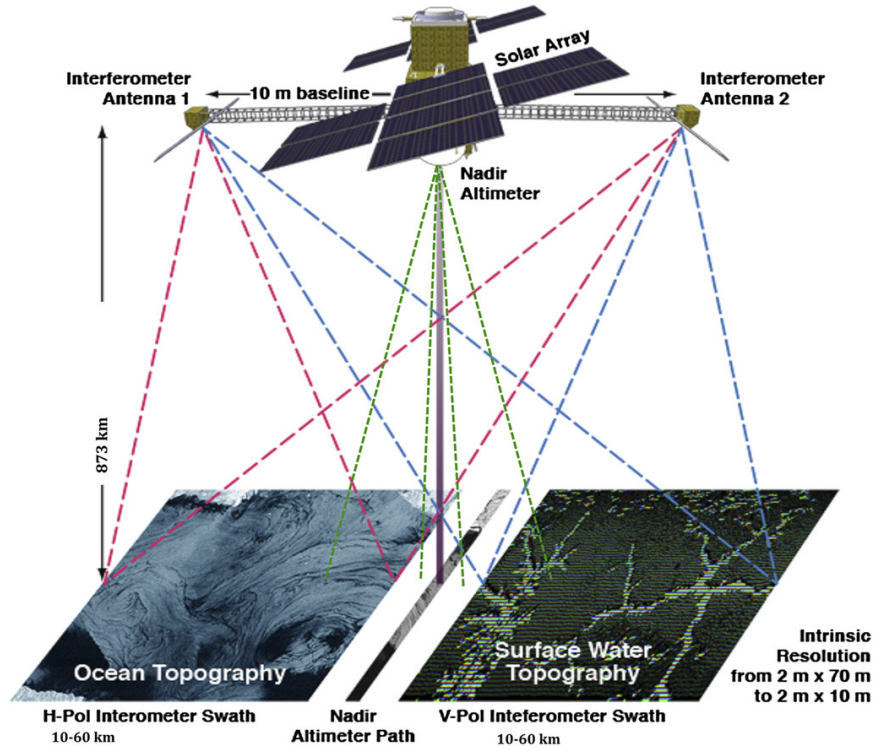


**Figure 1.5.** The configuration of the measurement system of the SWOT mission. The red and blue dashed lines represent the path of the transmission and reception of radar signals, respectively, over the two 50-km-wide swaths for interferometry between the two interferometer antennas. The green dashed lines represent the reception of radar signals near the nadir for interferometry between the nadir altimeter antenna and one of the interferometer antennas for observing the near-nadir regions where the targets have nearly equal distance to the two interferometer antennas. Both swaths have the same capability of making observations either over the ocean or the land surface water. (cited from Fu and Ubelmann, 2014)

In this dissertation, we utilized satellite radar and laser altimetry data, through careful data processing and analysis, to investigate small-scale ocean dynamics on a global scale. Our findings provide important insights into the variations and mechanisms of small-scale ocean dynamics, as well as advantages and caveats of different data analysis methods. Furthermore, this dissertation has laid the foundation for taking full advantage of the upcoming SWOT data, which will provide high-resolution, high-precision, wide-swath SSH measurements and enable significant discoveries in our understanding of ocean dynamics.

## Chapter 2

# Assessment of ICESat-2 for the Recovery of Ocean Topography

The Ice, Cloud and land Elevation Satellite 2 (ICESat-2) laser altimetry mission, launched in September 2018, uses six parallel lidar tracks with very fine along-track resolution (15 m) to measure the topography of ice, land and ocean surfaces. Here we assess the ability of ICESat-2 ocean data to recover oceanographic signals ranging from surface gravity waves to the marine geoid. We focus on a region in the tropical Pacific and study photon height data in both the wavenumber and space domain. Results show that an ICESat-2 single track can recover the marine geoid at wavelengths  $>20$  km which is similar to the best radar altimeter data. The wavelength and propagation direction of surface gravity waves are sometimes well resolved by using a combination of the strong and weak beams, which are separated by 90 m. We find higher than expected power in the 3-20 km wavelength band where geoid and ocean signals should be small. This artificial power is caused by the projection of 2-D surface waves with  $\sim 300$  m wavelengths into longer wavelengths (5-10 km) because of the 1-D sampling along the narrow ICESat-2 profile. Thus ICESat-2 will not provide major improvements to the geoid recovery in most of the ocean.

## 2.1 Introduction

Over the past four decades, radar altimetry has been providing high-accuracy global sea surface height (SSH) measurements associated with the time-invariant marine geoid as well as dynamic oceanic variabilities. Several recent studies have highlighted the need to achieve 1 mGal gravity accuracy at a half wavelength spatial resolution of about twice the mean ocean depth ( $\sim 8$  km) to map small-scale tectonics, seamounts and continental margin structure (e.g. Andersen et al., 2017; Sandwell et al., 2014). This 1 mGal objective corresponds to a sea surface slope accuracy of  $\sim 1 \mu\text{rad}$  or 8 mm over a distance of 8 km. The distance of 8 km corresponds to the optimal recoverable resolution of gravity anomaly from seafloor roughness, limited by the ocean depth due to upward continuation. The current best static gravity model based on all available repeat and non-repeat radar altimetry has reached an accuracy of 1 or 2 mGal in most ocean areas at a full-wavelength spatial resolution of 16-20 km (Sandwell et al., 2019).

At these small spatial scales, the largest error source in radar altimetry of SSH is related to ocean surface gravity waves. The sharp outgoing radar pulse is blurred by reflections from the peaks and troughs of the surface waves within the pulse-limited footprint of the radar altimeter (3 km at 2 m significant wave height, SWH). Individual radar waveforms at a 20 Hz sampling rate have a range error of  $\sim 40$  mm (Zhang and Sandwell, 2017). Better range precision of about 20 mm has been achieved by SARAL/ALtiKa which operates at a shorter wavelength and has a higher bandwidth and pulse repetition frequency. Further gravity improvements with pulse-limited radar altimetry will be gradual as the noise is reduced as the square root of the number of observations. Here we investigate the laser altimeter data from the Ice, Cloud and land Elevation Satellite 2 (ICESat-2) to better understand its potential contributions to gravity field recovery as well as to understand how surface waves and other oceanographic signals degrade radar range precision.

ICESat-2, which launched in September 2018, uses lidar to measure elevation with a primary focus on the cryosphere and a tertiary objective of ocean topography. The Advanced Topographic Laser Altimeter System (ATLAS) onboard splits the green laser into six beams arranged in three pairs. Each pair consists of a strong and a weak beam with an energy ratio about 4:1. The beams are separated by 90 m in the cross-track direction and by  $\sim 2.5$  km in the along-track direction. The three beam pairs are 3.3 km apart in the cross-track direction (Smith et al., 2020). The round-trip traveltimes of photon beams that reflect from the ocean surface provide estimates of height above a reference ellipsoid with 10 m horizontal accuracy and 0.03 m vertical precision (Smith et al., 2020). ICESat-2 has a high sampling rate (10 kHz), narrow footprint (15 m in diameter), near-global coverage ( $92^\circ$  inclination) and a 91-day repeat. Around  $10^{14}$  photons leave the ATLAS sensor per laser shot. Among photons that are reflected off the ocean surface, only 0-4 per laser shot travel back to the ATLAS because the open ocean has low reflectance in the visible spectrum (Hartmann 2015; Neumann et al., 2020). The ocean signal rates are similar to land. Neuenschwander and Magruder (2016) initially showed that ICESat-2 is able to accurately retrieve terrain heights from photon signal aggregation, which can be applied to surface wave characterization. Over the ocean, ICESat-2 is proven to allow for imaging individual waves (Klotz et al., 2019), and the signal that it detects is influenced by a mixture of surface and internal waves, tides and balanced flows.

Each ICESat-2 ATLAS data set begins with the prefix “ATL”. All products and related documents can be accessed through the National Snow & Ice Data Center. The ICESat-2 team provides a standard ocean height product ATL12 (Morison et al., 2019) which takes in ATL03 photon heights (Neumann et al., 2020) and outputs heights at a variable spacing (5-7 km over the tropical Pacific) along with SWH and statistics. Although ATL12 aims to achieve 10 mm accuracy for mean sea surface (MSS) height (Morison et al., 2019), the 5-7 km along-track sampling of that product is not adequate for our analysis which investigates the adverse effects of surface gravity waves on the recovery of the MSS.

The fine spatial resolution of ICESat-2 photon height data ( $\sim 15$  m) motivates us to investigate its potential for ocean topography recovery. In this paper, we divide the ocean topography signals into three wavelength bands: MSS (MSS = geoid + mean dynamic topography,  $> 20$  km); surface gravity wave band ( $< 3$  km); and the less well understood intermediate band (3-20 km). We address the following questions: (1) Can the ICESat-2 ocean data be used to improve the accuracy and resolution of the marine geoid and gravity field? (2) What type of filter is best for the recovery and removal of sea surface signals that have scales less than 3 km in wavelength? (3) What is the origin of the height signal in the intermediate band range (3-20 km)? We address these questions by investigating ICESat-2's photon height profiles in an area of the tropical Pacific (longitude  $-120^\circ$  to  $-100^\circ$ , latitude  $-11^\circ$  to  $-1^\circ$ ) having relatively low mesoscale ocean variability (Tchilibou et al., 2018) and calm sea state, with typical SWH less than 2 m (Stopa, 2019). These height profiles measure the MSS as well as temporal variations associated with tides, ocean currents, and gravity waves.

The ICESat-2 ATL03 photon height data are analysed in both the wavenumber domain and the space domain. The wavenumber domain analysis reveals the full spectrum of height variations over wavelengths from 50 m to 500 km. In addition, cross-spectral analysis among the three strong lidar beams, as well as a MSS height model (MSSCNESCLS19), which is based on all available radar altimeter data (Schaeffer et al., 2018) with 16-20 km spatial resolution, reveals the best spatial resolution that is consistently recorded in ICESat-2 tracks. This wavenumber analysis also provides the rationale for the design of along-track filters to separate the signal and noise components. We then use bandpass filters to analyse the signal and noise of the ICESat-2 data in the space domain. We also generate synthetic SSH fields using wave buoy data to assist understanding the 1-D sampling of 2-D surface waves. In addition, we show that there are errors related to ocean surface gravity waves contaminating ICESat-2 observations in two ways: (1) surface waves are energetic and need to be reduced by averaging repeating observations and (2)

surface waves in the 1-D sampling of laser altimeters could be projected to much longer apparent wavelengths and contaminate longer wavelength signals (5-10 km and longer).

## 2.2 Wavenumber Domain Analysis

We choose ATL03 geolocated photon heights in a  $20^\circ$  by  $10^\circ$  tropical Pacific box (longitude:  $-120^\circ$  to  $-100^\circ$ , latitude:  $-11^\circ$  to  $-1^\circ$ ), selected because of its low variability in dynamic ocean topography. We use the strong beam photon heights that have medium and high confidence values. We assembled all strong beam profiles having more than 70% cloud-free data spanning the time period from December 2018 to May 2020. About 15% of the profiles satisfy these criteria (341 out of 2325 profiles). Heights were corrected for solid earth tides, solid earth pole tides, ocean loading and ocean pole tides and referenced to the WGS84 ellipsoid (Neumann et al., 2020). We further apply ocean tides and inverse barometer corrections to the geolocated photons using geophysical corrections provided in the ATL03 data set. Original data are sampled at 10 kHz, which corresponds to roughly 0.7 m in the along-track direction. We resample the data at 5 m intervals using a robust median, low-pass Gaussian filter with 0.5 gain at 30 m wavelength with the robust option in the Generic Mapping Tools “filter1d” function (Wessel et al., 2013). Median filtering reduces potential contamination from large height outliers caused by scattering of photons in the atmosphere as well as reflections from the subsurface. The filtered heights are used for all the analysis that follows.

First, we calculate the power spectral density (PSD) of each height profile using the Lomb-Scargle method (Lomb 1976; Scargle 1982). Interpolating gaps in height profiles is not desirable considering the large percentage of missing data. The Lomb-Scargle method is a spectral analysis algorithm for irregularly sampled and gappy data that is widely used in the astronomy community. We finally average the 341 power spectra to obtain the PSD in the Pacific



box, which is shown in Figure 2.1. The 99% confidence interval is shaded in red.

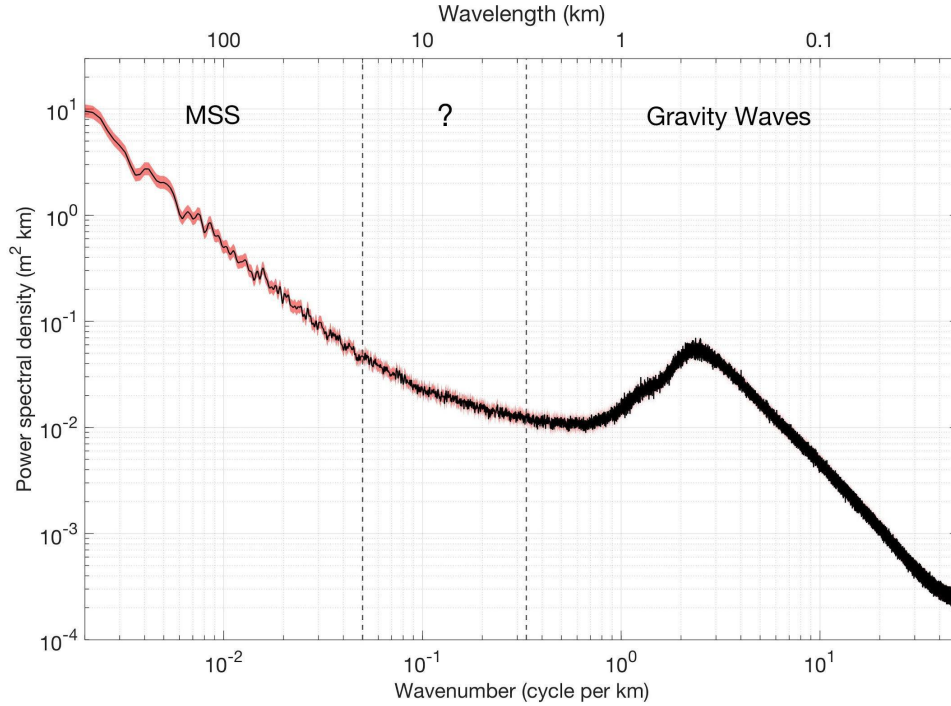


**Figure 2.1.** Averaged SSH power spectral density in the Pacific box. The spectrum can be divided into three bands representing long wavelength MSS signals (20-500 km), surface gravity waves ( $< 3$  km), and the more poorly understood intermediate wavelength band (3-20 km). The 99% confidence interval is shaded in red.

From the average spectra (Figure 2.1), we identify three main spectral bands:

1. The long-wavelength band ( $> 20$  km) mainly reflects the MSS height which is a combination of time-invariant geoid height and mean ocean dynamic topography. We also use the MSSCNESCLS19 MSS model as the reference to remove the MSS and isolate the power spectrum of the sea level anomaly (SLA, Figure 2.11). Since the barotropic tides have also been removed, and there is no strong current in this tropical Pacific box, the remaining sea level variations are hypothesized to be primarily attributable to unbalanced flows and internal tides. This hypothesis is supported by the  $k^{-1}$  to  $k^{-2}$  spectral slope of SLA (Figure 2.11).

2. The short wavelength part of the spectrum has a broad peak centered around 300 m. We show that this is mainly due to surface gravity waves. Note that the 341 profiles were collected at different times and thus sample different sea states, composed of waves with multiple wavelengths and directions. In particular, there is a wide range of possible wave directions  $\alpha$  with respect to the ascending and descending tracks of the ICESat-2 orbit. This causes an increase in the apparent wavelength of the waves due to a  $1/\cos \alpha$  trigonometric relation.
3. The power in the intermediate part of the spectrum is less well understood since this band is poorly sampled by radar altimeters because of their large pulse-limited footprint (3-5 km, Xu and Fu, 2012). *In situ* measurements, i.e., ocean buoys, profilers, suggest two dominant types of ocean phenomena in this band: (i) Infragravity waves with wavelengths  $> 1$  km typically have amplitudes of  $< 10$  mm in the tropical Pacific (Aucan and Ardhuin, 2013); (ii) High mode internal waves/tides are also common and have amplitudes  $\sim 10$  mm (Savage et al., 2017). Our more detailed, space-domain analysis of the ICESat-2 data, provided below, shows amplitudes of 100-200 mm in this band which is much larger than expected. A major focus of this paper is to understand the source of these large amplitude signals. If they are true oceanographic signals, they will be observed by the Surface Water and Ocean Topography mission (SWOT) due to SWOT's high spatial resolution and 50-fold decrease in noise level ( $2 \text{ cm}^2/(\text{cycle/km})$ ) (Desai et al., 2018). As we show further in this manuscript, it is more likely that these large amplitude signals in intermediate wavelengths are due to instrument or sampling issues.

To better understand the signal and noise characteristics of ICESat-2 as a function of wavelength we perform two types of cross-spectral analyses. The first inter-compares the three strong beams of individual tracks to understand the MSS resolution capability of ICESat-2. This type of cross-spectral analysis is commonly used by the marine geophysics community to characterize the shortest wavelength resolvable in the along-track altimeter data (Marks and

Sailor, 1986; Marks and Smith, 2006; Yale et al., 1995). We select one profile (reference ground track: 0394, cycle: 02, segment number: 08, sensing time: 2019/01/23) in the Pacific Ocean with latitudes ranging from  $-21.5^\circ$  to  $-11^\circ$  and compute cross-spectra for the height in the three parallel strong beams. We use data with latitudes shifted to  $-21.5^\circ$  to  $-11^\circ$  that is beyond the Pacific box because there is no gap larger than 10 km and fewer than 20% of data are missing for all 3 beams. We interpolate gaps, detrend, apply a Von Hann taper (also known as the Hanning window) to each 82 km segment, and use Welch's method to obtain the cross-spectrum (including the coherence magnitude squared, or CMS, and phase), which is shown in Figures 2.2a and 2.2c.

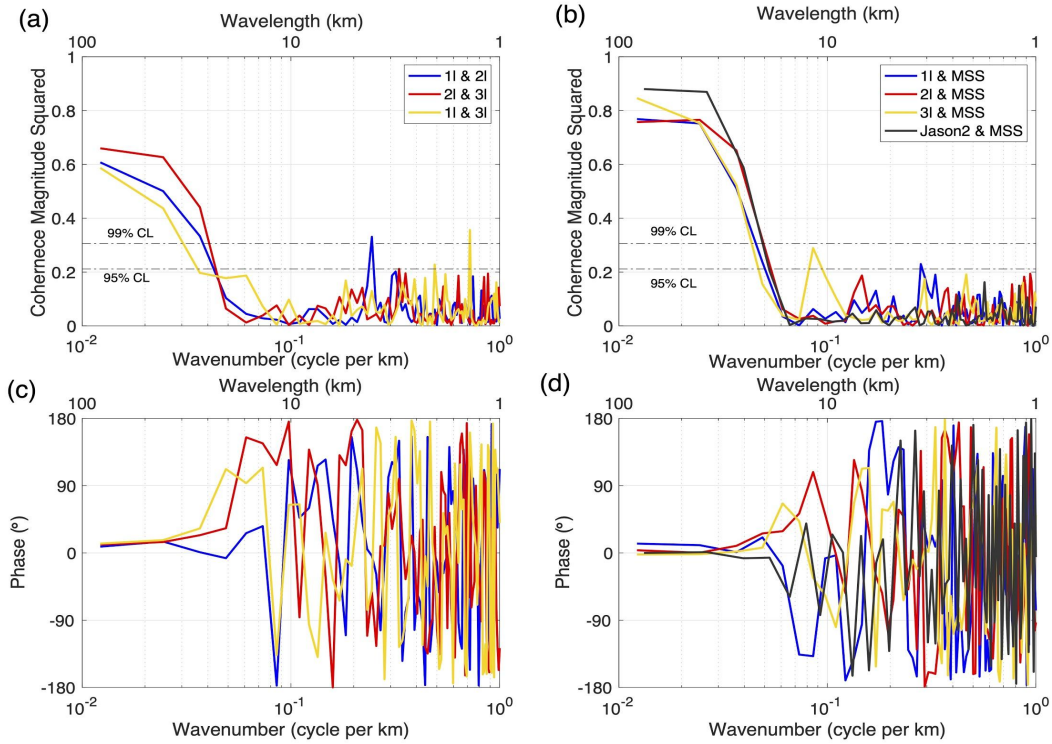


**Figure 2.2.** (a) CMS and (c) phase between beams 11-21, 21-31, 11-31 of a selected ICESat-2 track (ground track: 0394, cycle: 02). CMS falls to below 95% CL at  $\sim 25$  km. (b) CMS and (d) phase between MSS and each strong beam. Black line is the spectral CMS and phase between 20Hz Jason-2 and MSS. CMS falls to below 95% CL at  $\sim 20$  km for both the ICESat-2 and the Jason-2 cases.

In this intercomparison, CMS is large at longer wavelengths where the MSS signal

dominates, and it falls below the 95% confidence level (CL) at around 25 km (Figure 2.2a). The phase lag is around zero for the coherent wavelengths (Figure 2.2c). There are many factors that control resolution, including: gravity signal, oceanographic and instrument noise, ocean depth and number of cycles (Yale et al., 1995). Here we analyse only one track consisting of three beams, which are separated by 3.3 km in the cross-track direction and have slightly different MSS. Low CMS does not necessarily mean that measurement noise dominates. Below, in the space domain analysis, we will show an example of high CMS at  $\sim 300$  m wavelengths for strong and weak beams separated by 90 m in the cross-track direction; this high CMS is due to surface waves. Yet neighbouring strong beams separated by 3.3 km are generally not coherent in the surface wave band.

The second coherence analysis uses the MSSCNESCLS19 MSS model as the reference for each of the strong beams. This MSS model has spatial resolution of 16 km so we cannot expect the analysis to reveal shorter wavelength signals in the altimetry but we can evaluate the accuracy at longer wavelengths ( $\sim 20$  km) and also indirectly compare the resolution of ICESat-2 with other altimeter data. We correct for cross-track MSS differences by removing the MSS at the location of each of the three beams and adding back the MSS for the centre beam 2l. The spectral CMS and phase between each beam and the MSS are shown in Figures 2.2b and 2.2d. In this case, the signal is the time invariant MSS, which is common to all three beams, and noise arises from oceanic processes and measurement noise. This analysis shows statistically significant CMS and low phase for wavelengths longer than 20 km. The greater CMS between the ICESat-2 profiles and the MSS compared to the interbeam CMS is consistent with what we would expect if we assume that ICESat-2 SSH beams contain noise while the MSS is noise free (Bendat and Piersol, 2011). A higher CMS limit could be achieved with multitrack stacking.

To compare these ICESat-2 results with radar altimetry, we analysed 20 Hz sampled Jason-2 radar altimetry height profiles (cycle 233) and calculated their cross-spectrum with the

MSS. The along-track spacing of Jason-2 is 296 m. We apply a 256-point non-overlapping Von Hann window (segment length is about 76 km) and use Welch’s method to compute the spectral CMS and phase between Jason-2 and MSS, which is shown in Figures 2.2b and 2.2d in black lines. A shorter track is used in order to obtain the same number of segments as ICESat-2. We find that Jason-2/MSS drops to 99% and 95% CLs at similar wavelengths as the ICESat-2/MSS CMS. This suggests that ICESat-2 has signal and noise characteristics similar to those of Jason-2 in terms of MSS reconstruction, with a characteristic coherent length scale of about 20 km for a single pass. Although the analysis focuses on single ICESat-2 and Jason2 tracks, we have analysed more tracks in the Pacific box and see that the results shown in Figure 2.2 are representative, when all three beams show good quality and have no major data gaps larger than 10 km.

## 2.3 Space Domain Analysis

Given these wavenumber domain analyses, we examine the signal and noise of ICESat-2 data in each of the three bands in the space domain using the same three strong beams (reference ground track: 0394, cycle: 02, segment number: 08, sensing time: 2019/01/23) as in Figure 2.2.

### 2.3.1 Long Wavelength Mean Sea Surface

The coherence analyses (Figure 2.2) suggest that the three beams all measure the same MSS at wavelengths greater than 20 km. A space domain example is shown in Figure 2.3 where each of the three beams was low-pass filtered using a Gaussian with 0.5 gain at 20 km. As described above, beams 11 and 31 were corrected to the location of the beam 21, and a trend was removed from each. There is general agreement between ICESat-2 and radar altimeter derived MSS at long wavelengths. A shorter segment of the plotted beams (Figure 2.3b) reveals that the differences have amplitudes of  $\sim 0.03$  m.

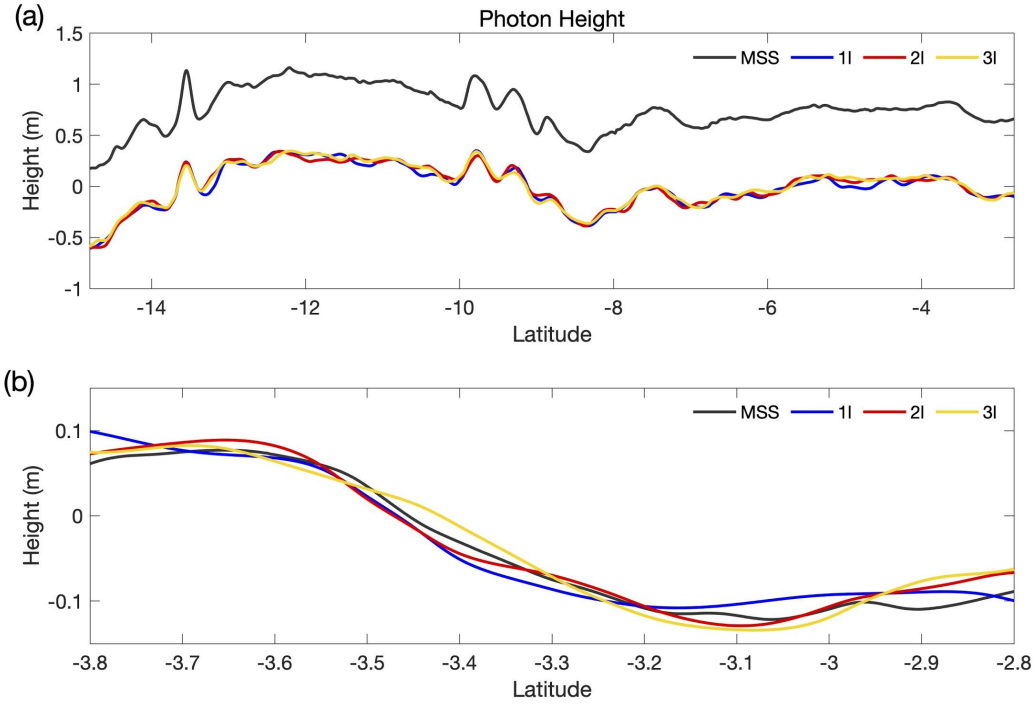


**Figure 2.3.** (a) SSH of ICESat-2 3 strong beams (ground track: 0394, cycle: 02) along with MSS at beam 2l's position. Data are low-pass filtered at 20 km, and the linear trend of beam 2l has been removed from all four height series. The MSS is offset for plotting. (b) a shorter segment with no MSS offset. Tracks run almost north-south so  $1^\circ$  in latitude corresponds to  $\sim 110$  km along track.

### 2.3.2 Short Wavelength: Surface Gravity Waves

To isolate the signals from surface waves, we first remove the MSS from each strong beam profile to create SLA (Figure 2.4). These profiles contain oceanographic signals and noise over the entire spectrum. Most of the cross-beam differences and along-track variations have a wavelength of a few hundred metres and are consistent with height signals from surface gravity waves (Figure 2.4b).

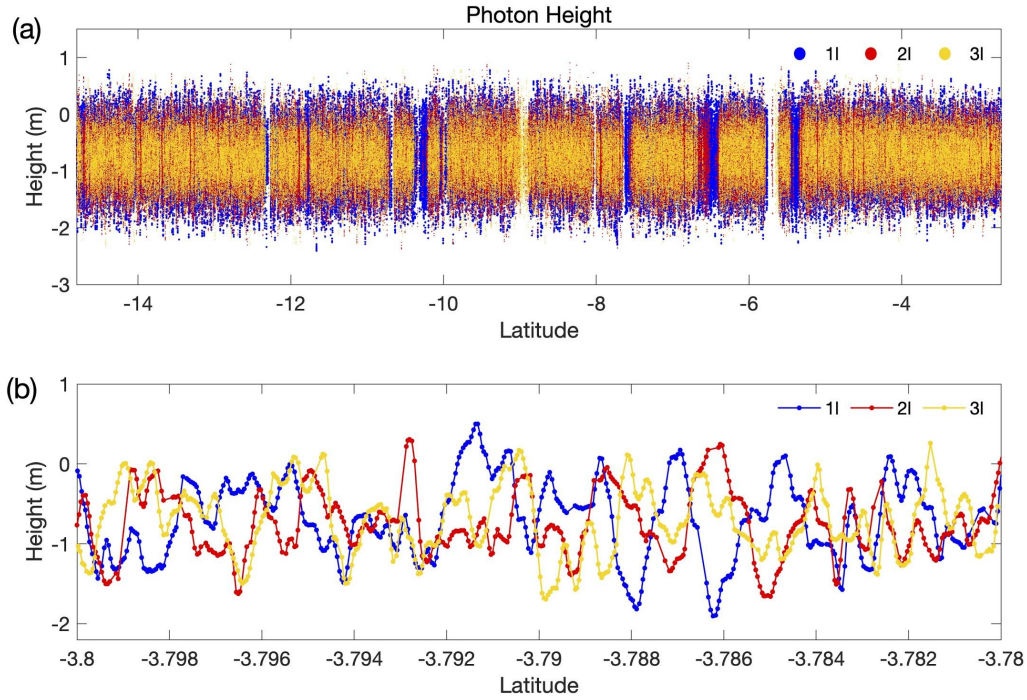


**Figure 2.4.** (a) SLA of ICESat-2 3 strong beams (ground track: 0394, cycle: 02). (b) a shorter segment of (a) showing peak to trough variations having wavelengths of a few hundreds of meters. Tracks run almost N-S so  $1^\circ$  corresponds to  $\sim 110$  km along track and each  $0.002^\circ$  grid in (b) is about 200 m.

### Significant wave height analysis

We further calculate the SWH from ICESat-2 SLA data. For radar altimetry, the SWH is four times the root-mean squared (rms) height variation in the 3-km pulse-limited footprint averaging area, and it is derived from the rise time of the fit to the return waveform. To calculate SWH for the ICESat-2 data, we first low-pass filter the SLA using a running mean over a 3 km window. This is done to simulate the 3-km pulse-limited footprint of a radar altimeter. The rms difference from the mean, times 4, is further low-pass filtered over 6 km to simulate the 1Hz averaged SWH in radar altimetry. The results are shown in Figure 2.5 where the SWH varies between 1.5 and 2 m, which is typical for this region (Stopa 2019; Dodet et al., 2020). Differences in SWH between the 3 beams can be up to  $\sim 0.3$  m. This is to be expected since there could be sea state gradients over scales of kilometres.

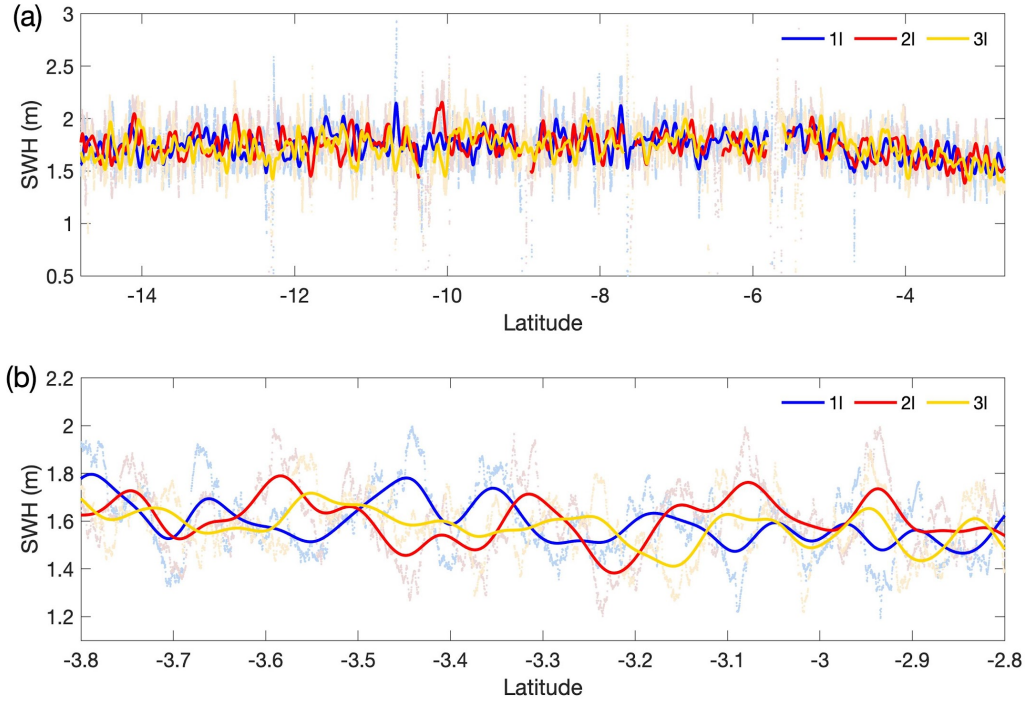


**Figure 2.5.** (a) SWH calculated from 3-km-running standard deviation of SLA from ICESat-2 3 strong beams (ground track: 0394, cycle: 02). Background light dots are SWH before filtering and darker lines are low-pass filtered at 6 km so that they resemble the 1Hz averaged SWH in radar altimetry. (b) a shorter segment of (a). Tracks run almost N-S so  $1^\circ$  corresponds to  $\sim 110$  km along track.

### Dominant ocean wave reconstruction

We can further analyse the surface gravity wave signal using the strong/weak beam pairs spaced at 90 m. Considering that weak beam data have very limited photon recovery from the ocean surface, the analysis here is applied to segments with a minimum length of 20 km, where a pair of strong and weak beams both have collected good-quality photon data. Each pair of strong and weak beams is generally highly coherent since the 90 m cross-track distance is less than the average wavelength of surface waves (including swell and wind seas) in this region (Young 1999; Arinaga and Cheung, 2012). The wavenumber of the CMS peak identifies the wavelength of the dominant wave projected in the orbit direction. The spectral phase is



the relative phase shift between two beams, and we can use it to reconstruct wave direction, though with a  $180^\circ$  ambiguity. We can further recover the true wavelength by combining wave direction and projected wavelength (details are provided in Figure 2.12 in Section 2.6). There is also  $\sim 2.5$  km along-track offset between each pair of strong and weak beams, as the weak and strong beam pairs are offset relative to each other. This corresponds to  $\sim 0.35$  second shift in time during which surface waves only travel a few metres. We identify phase shift from this time delay to error in wave reconstruction. This error has little influence on the CMS but will shift the phase by up to  $10^\circ$ . Figure 2.6 shows an example where a weak beam leads a strong beam in an ascending track. Statistically significant CMS over wavelengths in the swell band (100-1000 m) peaks around 465 m (observed wavelength in the orbit direction) with a phase shift of  $-70.3^\circ$ . These two effects are consistent with a  $327 \pm 16.8$  m swell wavelength coming from an azimuth of  $223.3 \pm 7.3^\circ$  (clockwise from north). The error ranges are obtained via the following steps: (1) dividing the beam pair into 11 equal-length segments, each subdivided into 10 short segments that are used to calculate the coherence between the strong and weak beams and (2) bootstrapping the 11 sets of coherence results over 100 realizations and calculating the 95% confidence interval. This reconstruction from ICESat-2 observations agrees with a WAVEWATCH III hindcast multigrid product (Chawla et al., 2012), which uses the operational National Centers for Environmental Prediction winds and ice fields as input forcing fields and is independent of altimetry observations. WAVEWATCH III provides a predicted wavelength of  $336.0 \pm 15.9$  m and azimuth of  $209.8 \pm 1.6^\circ$  at the nearest gridpoint and the closest time. The error ranges for WAVEWATCH III hindcast wavelength and direction come from the 95% confidence interval of data collected in a  $7^\circ \times 7^\circ$  region over 9 hours.

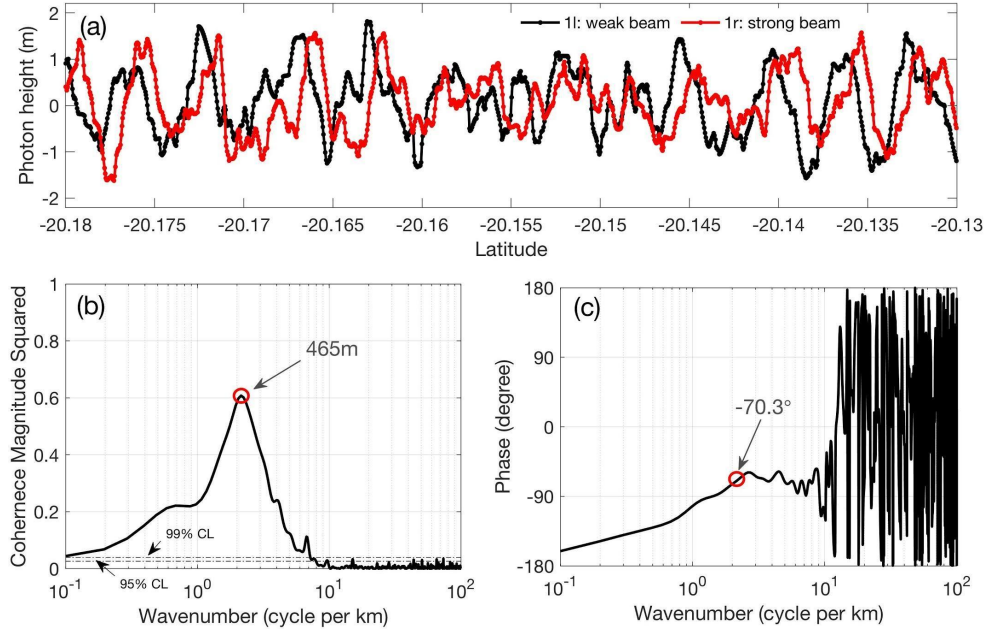


**Figure 2.6.** (a) a small segment of ICESat-2 photon height data w.r.t WGS 84. (ground track: 0326, cycle: 01). The strong and weak beams are separated by 90 m and both are low-pass filtered at 30 m. (b) CMS and (c) phase between beams 1l and 1r. Coherence peaks around 465 m, and the corresponding phase shift is  $-70.3^\circ$ . The 99% and 95% CL are labeled.

We have performed 456 sets of strong/weak beam analysis in the tropical Pacific region to establish the wavelength and wave direction from ICESat-2 photon data and compare the results with predictions of peak direction and peak wavelength from the WAVEWATCH III model at the gridpoint closest to the middle of each track. We also calculated the SWH from each set of beam pairs and made a comparison with the WAVEWATCH III model. The results are provided in Figure 2.7. Figures 2.7a-c shows joint probability histograms for wavelength, wave directions and SWH of WAVEWATCH III predictions and ICESat-2 pairs. In the histograms, wavelengths are binned by 50 m increments and directions by  $15^\circ$  increments. The SWHs are rounded to the nearest multiple of 0.2 m. Histograms of ICESat-2 and WAVEWATCH III differences are shown in Figures 2.7d-f, respectively. The ICESat-2 reconstructed wavelengths are slightly longer, and the best fit ICESat-2 to WAVEWATCH III wavelength slope is 1.11 with intercept set to zero. The histogram of wavelength differences (Figure 2.7d) has a quasi-Gaussian shape

and is slightly biased to the positive with a mean difference  $\mu$  of 57.3 m, and root mean square error (RMSE) of 151.0 m. The ICESat-2 reconstructed wave directions are generally between  $0^\circ$ - $60^\circ$  and  $120^\circ$ - $180^\circ$ , as waves propagating orthogonally to satellite ground tracks are less likely to show coherence between a pair of strong and weak beams. A regression of ICESat-2 to WAVEWATCH III directions shows that for the propagation directions from  $0^\circ$  to  $60^\circ$ , ICESat-2 propagation directions are about 81% of WAVEWATCH III directions. The histogram of wave directional differences (Figure 2.7d) centres around zero, although it spreads widely from  $-90^\circ$  to  $90^\circ$  (directional differences larger than  $\pm 90^\circ$  are indistinguishable from directional differences between  $-90^\circ$  and  $90^\circ$ ; the plot shows only the smallest possible directional difference). The mean value of direction differences  $\mu$  is  $20.5^\circ$ , and the RMSE is  $69.4^\circ$ . For SWH, the ICESat-2 values compare well with WAVEWATCH III, with a mean difference of -0.04 m and RMSE of 0.34 m, which is similar to the result in Klotz et al. (2019), who compared ICESat-2 and the ERA-5 reanalysis in the Atlantic Ocean. The ICESat-2 SWHs are slightly small and are about 0.96 of WAVEWATCH III SWH.

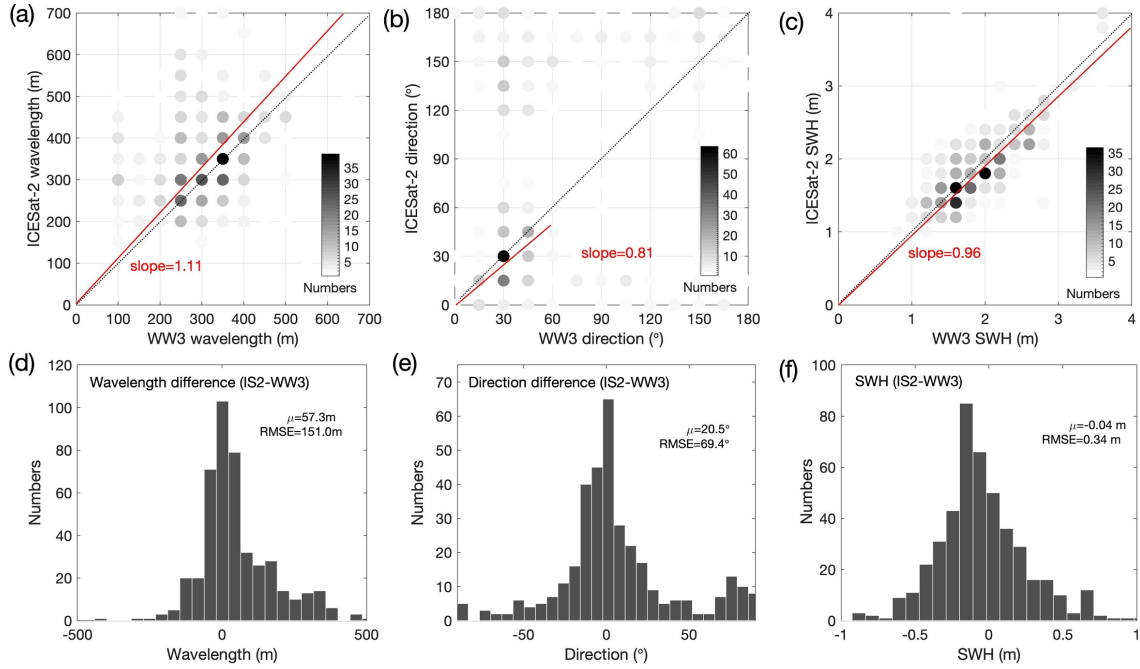


**Figure 2.7.** Joint probability histograms for (a) wavelength, (b) wave directions and (c) SWH of WAVEWATCH III (WW3) predictions and ICESat-2 (IS2) reconstructions. The black dotted line is the 1:1 relationship and the red line is the best fitted slope. Histogram of (d) wavelength, (e) direction and (f) SWH differences between IS2 reconstructions and WW3 predictions. The mean  $\mu$  and RMSE of wavelength/direction/SWH differences are shown in (d)-(f).

### 2.3.3 Sea Level Anomalies at Wavelengths $>3$ km

Finally, we investigate the SLA for wavelengths  $>3$  km. We low-pass filter ICESat-2 SLA using a Gaussian with a 0.5 gain at 3 km to remove most of the signals from the surface gravity waves and isolate other oceanography signals (see Figure 2.8). The low-pass filtered SLA shows much smaller amplitude (0.1-0.2 m) than the full band SLA in Figure 2.4 ( $\sim 1$  m). All three beams show a common undulation having a characteristic wavelength of about 400-500 km. This signal is likely due to the dynamic topography of the ocean caused by currents or tide-model error, as it also shows up in other cycles of the same ground track, but in different phases.

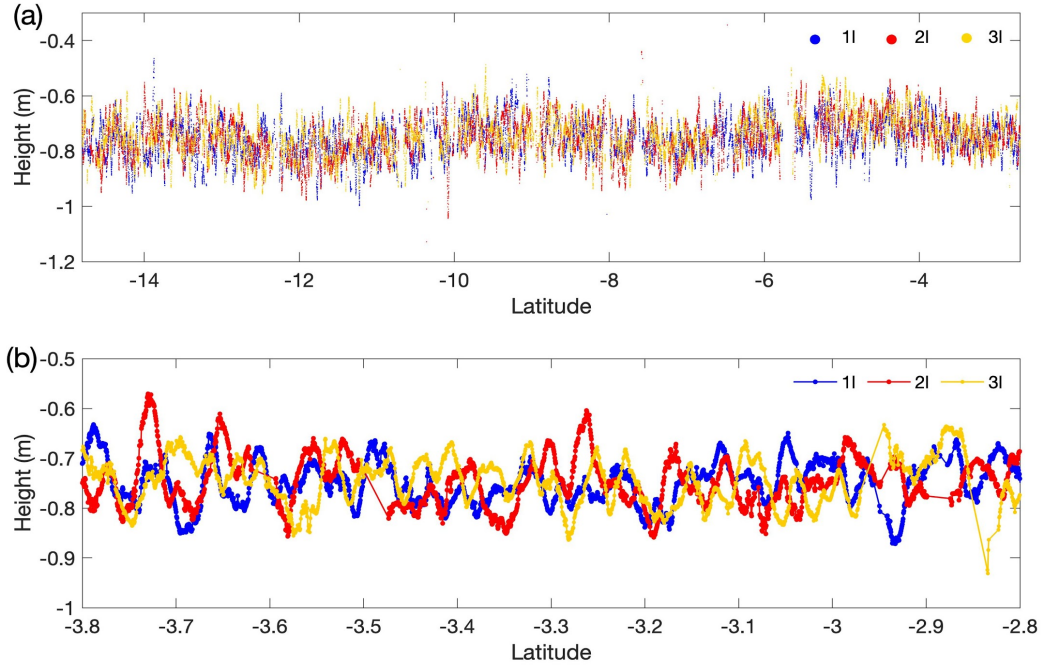


**Figure 2.8.** (a) Low-pass filtered (3 km and sampled at 50 m) SLA. Missing data were not included in the filter. (b) a shorter segment of (a). Tracks run almost N-S so  $1^\circ$  corresponds to  $\sim 110$  km along track.

In addition to this expected longer wavelength oceanographic signal, there are rather large signals (0.1-0.2 m) with wavelengths of 5-10 km (Figure 2.8b). As noted in the introduction we expected that oceanographic signals should be 10 times smaller in this wavelength band (Savage et al., 2017; Aucan and Ardhuin, 2013). Moreover, if they are due to ocean phenomena with length scales of 5-10 km, then the signals should be coherent among the three beams. However, in our coherence analysis (Figure 2.2), we show that the three beams are incoherent over this band. The remaining explanations for these signals are either that errors in the ICESat-2 photon data are different among the three beams or that shorter wavelength signals are projected into longer wavelengths. We note that the ICESat-2 sampling is a very narrow 1-D track sample of a 2-D ocean surface.

## 1-D sampling of a 2-D ocean waves

The largest signal in the ICESat-2 SLA data is due to surface waves. If the dominant wave direction is roughly aligned with the direction of an ICESat-2 track, then the 3 km low-pass filter will remove this signal, leaving behind an essentially flat SLA. However, if the wave direction is nearly perpendicular to the track, the ocean swell having characteristic wavelengths of a few hundred metres will be projected to wavelengths longer than 3 km. Next, we illustrate the extent of this projection.

Assume there is a plane wave with wavelength  $L_0$  and amplitude  $A$  coming from the north ( $\theta = 0^\circ$ ), then the SSH ( $\eta$ ) due to the wave can be described as:

$$\eta(x, y, t) = A \cos(ky - \omega t + \varphi), \quad (2.1)$$

where  $x$  is in the eastward direction and  $y$  is northward,  $k = \frac{2\pi}{L_0}$  is the horizontal wavenumber,  $\omega = \sqrt{gk}$  is the angular frequency ( $g = 9.81 \text{ m/s}^2$  is the gravitational acceleration), and  $\varphi$  is the initial phase. In the 1-D sampling of a satellite flying from direction  $\theta_0$  (north:  $0^\circ$ , east:  $90^\circ$ ) at a ground speed of  $V_s$  ( $\sim 7 \text{ km/s}$ ), the observed along track wave height should be:

$$\eta(S, t) = A \cos(kS \cos \alpha - \omega \frac{S}{V_s} + \varphi) \quad (2.2)$$

$$= A \cos((k \cos \alpha - \frac{\omega}{V_s})S + \varphi), \quad (2.3)$$

where  $\alpha = \theta - \theta_0$  is the angle between wave direction and orbit,  $S = y / \cos \alpha$  is the along-track distance. The observed wavenumber  $k'$  is:

$$k' = k \cos \alpha - \frac{\omega}{V_s}, \quad (2.4)$$

and the observed wavelength  $L'$  is:

$$L' = \frac{2\pi}{k \cos \alpha - \frac{\omega}{V_s}} = L_0 / (\cos \alpha - \frac{\omega L_0}{2\pi V_s}) \approx L_0 / \cos \alpha. \quad (2.5)$$

ICESat-2 has a ground velocity of 7 km/s so waves propagating at an angle  $\alpha$  with respect to the track will shown an apparent wavelength that is longer by around  $1/\cos \alpha$ . As  $\cos \alpha$  approaches zero, the satellite ground speed becomes increasingly important. For example, for a 200 m plane wave, when  $\alpha = 88^\circ$ , the satellite will observe an 8 km apparent wavelength; when  $\alpha = 90^\circ$ , the apparent wavelength is 79 km. This projection pattern is a particular challenge for ICESat-2's small footprint, as it implies that any component of 50-300 m surface wave crests aligned with the satellite orbit could project to wavelengths of 20 km or longer. Because surface gravity waves are energetic compared with the background large-scale SSH, even low-amplitude waves have the potential to fill in the intermediate portion of the spectrum.

In the extreme case of the waves propagating in a direction nearly perpendicular to the track with the relation  $\cos \alpha = \frac{\omega L_0}{2\pi V_s}$  ( $\alpha = 89.855^\circ$  if  $L_0 = 200$  m;  $\alpha = 89.771^\circ$  if  $L_0 = 500$  m), ICESat-2 will only sample a single height, so the observed wavelength will be shifted away from the true wavelength to infinitely long scales, and all three beams will be measured as different heights depending on the phase of the waves they sample. Here we assumed only a plane wave case which does not capture the complexity of true sea states, so we need to investigate how ICESat-2 would sample a more realistic ocean surface.

### **Synthetic wave field analysis**

To generate a realistic 2-D sea state we use a time series of ocean surface elevation collected from a 3-component GPS receiver on a wave buoy. There are no wave buoys in our South Pacific box so we selected buoy data from the Coastal Data Information Program (CDIP)

at station Point Reyes, off the California coast (latitude:  $37.94^{\circ}\text{N}$ , longitude:  $-123.46^{\circ}\text{E}$ , depth: 550 m, time: 2019-09-29, 19:00 UTC). This buoy is located in deep water, so we will assume that waves follow the deep water dispersion relation. Although the CDIP directional spectrum only reflects the wave conditions at a specific point, time-averaged over half an hour, it provides realistic statistics of waves coming from all directions to generate a surface wave only SSH field.

We generate finite length, 2-D synthetic sea surface elevations by assuming that the sea state results from the linear superposition of all wave components measured by the wave buoy and assigning random phases to the amplitudes. To avoid the extreme case of waves being projected to infinitely long scales in the ICESat-2 orbit direction ( $182^{\circ}$ ), we omit a  $2^{\circ}$  range of the 2-D wave spectrum ( $91-93^{\circ}$ ,  $271-273^{\circ}$ , white area in Figure 2.9a). The directional wave spectrum as a function of wave period and direction (Figure 2.9a) was computed from the angular moments provided by CDIP using the maximum entropy method (Lygre and Krogstad, 1986). The wave period varies between 1.72 and 40 s, with a corresponding wavelength between 5 and 2500 m. In this case study, most energy comes from  $330^{\circ}$  (northwest), and there is almost no energy for waves longer than 20 s ( $\sim 624$  m in wavelength). In addition to the most energetic wave systems, coming predominantly from  $330^{\circ}$ , the wavefield at this specific time and location also contains some wave energy at periods between 8 and 13 s (100-264 m in wavelengths) that is spread across directions between  $240^{\circ}$  and  $360^{\circ}$ . It is also worth noting that there is some energy in direction bins that are nearly perpendicular (e.g. from  $\sim 269^{\circ}$ ) to the ICESat-2 trackline. In this case, the 1-D sampling will increase the apparent wavelength of these waves by a factor of  $\sim 20$ , so the energy of a 300 m wave would appear as a 6 km wavelength signal. The questions now are: what is the amplitude of this effect, and can it explain the observations in the 3-20 km wavelength shown in Figure 2.8?



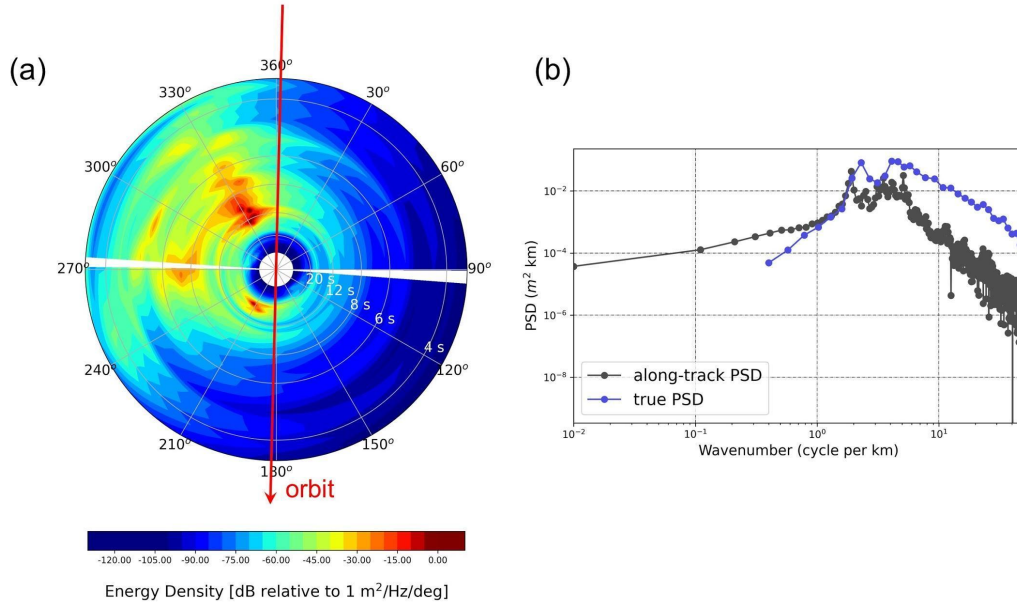


**Figure 2.9.** (a) Directional spectrum from CDIP station Point Reyes at time: 2019-09-29, 19:00 UTC. Energy density is in dB so as to show a large range of energy levels. The directional spectrum was computed using the maximum entropy method (Lygre and Krogstad, 1986). ICESat-2 orbit inclination is 92° and here we show a synthetic descending track (in red). Panel (b) gray: along-track PSD; blue: true PSD. Both are derived from the directional spectrum in (a).

We use the CDIP directional spectrum and positions of the ICESat-2 beams (ground track: 0394, cycle: 02) to take 1-D samples of the 2-D synthetic sea surface elevations in the ICESat-2 orbit direction. Following this method we generate three synthetic SLA profiles spaced by 3.3 km. We then apply a 3 km low-pass Gaussian filter. The synthetic profiles and 3 km low-pass filtered results are shown in Figure 2.10. We compute a 3 km running standard deviation of the synthetic SLA profiles and then multiply by 4 to get the SWH, which is around 1.95 with 0.4 m variation in amplitude. The SWH of synthetic along track SLA is smaller than the true SWH of 2.79 m from the CDIP buoy observations. While the synthetic SLA signals are realizations of surface gravity waves with wavelength less than 1 km, there are 0.2 m undulations with wavelengths of 5-10 km in the low-pass filtered SLA (Figure 2.10b), which result from short wavelength surface waves projected to much longer wavelengths in 1-D sampling profiles.

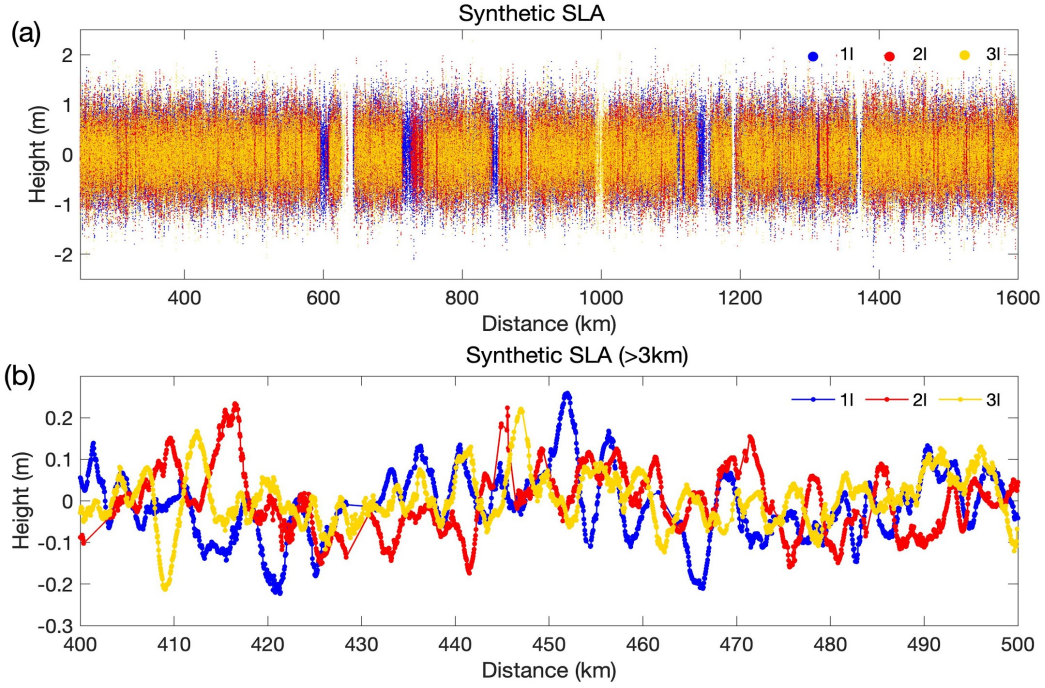


**Figure 2.10.** (a) Synthetic SLA using CDIP directional spectrum in Figure 2.9a and the positions of ICESat-2 track (ground track: 0394, cycle: 02). (b) 3 km low-pass filtered synthetic SLA for a 100-km segment.

To support our findings, we calculate the true PSD as well as the along-track PSD — as it would be observed by ICESat-2 — as a function of wavenumber (Figure 2.9b). The true wavenumber PSD  $E(q)$  (Figure 2.9b, blue) is obtained from the CDIP frequency spectrum  $E(f)$  using the deep water dispersion relation:

$$\omega^2 = \frac{2\pi g}{L} = 2\pi gq, \quad (2.6)$$

where  $\omega = 2\pi f$  is the angular frequency,  $L$  is the wavelength, and  $q = 1/L$  is the wavenumber, such that:

$$E(q) = \frac{g}{4\pi f} E(f). \quad (2.7)$$

We calculate the along-track PSD (Figure 2.9b, gray) that would be observed by ICESat-2 following the steps below:

1. Convert the observed directional wave spectrum  $E(f, \theta)$  with dimensions of  $\text{m}^2/\text{Hz}/\text{degree}$  in Figure 9a to a function of wavenumber and direction  $E(q, \theta)$  with dimensions of  $\text{m}^3/\text{degree}$ , following the deep water dispersion relation (2.6)

$$E(q, \theta) = \frac{g}{4\pi f} E(f, \theta). \quad (2.8)$$

2. Project the wavenumbers  $q$  from the wave direction  $\theta$  to the orbit direction  $\theta_0$

$$q' = q \cos \alpha, \quad (2.9)$$

where  $q'$  is the wavenumber projected to the along-track direction, and  $\alpha = \theta - \theta_0$  is the angle between the wave direction and the orbit direction.

3. We then create equally spaced along-track wavenumber bins  $q_s$  ranging from 0.01cpkm to 250.01cpkm with a spacing of 0.1 cpkm, and, for each bin, the along-track energy density  $E(q_s)$  is the integral of the projected energy density  $E(q, \theta) \cos \alpha$  over all grid points where  $q' = q_s$ .

As an example of the steps above, let us consider waves coming from  $\theta = 332^\circ$  with a period of 12 s and wavenumber  $q = 4.45$  cpkm ( $L = 225$  m). In the 1-D sampling from ICESat-2's descending orbit ( $\theta_0 = 2^\circ$ ), the satellite would observe an apparent wavenumber  $q' = 3.86$  cpkm ( $L' = 225\text{m}/\cos(330^\circ) = 259$  m). We would then integrate all projected wave energy

associated with an apparent wavenumber in the 3.81-3.91 cpkm bin to get the corresponding spectral energy at that bin in the along-track PSD (Figure 2.9b, in gray).

We compare the along-track PSD and the true PSD in Figure 2.9b to guide our interpretation of 1-D wave behaviour. In general, in the along-track PSD, there is decreased energy at the high wavenumber end ( $>5$  cpkm) and extra energy associated with low wavenumbers ( $<0.3$  cpkm) that are beyond the surface gravity wave range. Short-wavelength surface waves are projected to longer apparent wavelengths in the along-track direction; if they propagate in a direction nearly perpendicular to the orbit direction, surface waves could be projected to much longer wavelengths ( $>3$  km). There are several shifted swell peaks, including (1) the  $\sim 16$  s wave (430 m in wavelength, 2.3 cpkm in the true PSD) from direction  $213^\circ$  projected to 2 cpkm in the along-track direction and (2) the  $\sim 12.5$  s (244 m in wavelength, 4.1 cpkm in the true PSD) wave from direction  $330^\circ$  projected to 3.5 cpkm.

In the ocean, surface waves propagate from all directions with a broad range of frequencies and amplitudes of the order of 10 cm or more. If the wave field is fully isotropic, then an along-track spatial average of ICESat-2 measurements will minimize surface wave effects. As the example in Figure 2.9a indicates, often a single wavenumber and direction dominate the wave field. Problems will arise when the dominant surface wave crests align with the orbit direction, so that waves appear to have wavelengths of  $\sim 10$  km or more. In these cases a low-pass filter will not be able to suppress effects due to surface waves.

## 2.4 Discussion and Conclusions

We have studied the ability of ICESat-2 photon height data to recover oceanographic signals ranging from surface gravity waves to the marine geoid using data over a tropical Pacific

box in both the wavenumber domain and space domain. We analyse the data in three bands: long wavelengths (20-500 km), intermediate wavelengths (3-20 km) and short wavelengths (15 m-3 km).

At long wavelengths, we use coherence to compare the three parallel beams of ICESat-2, as well as a high resolution MSS model based on radar altimetry, to show that the single track can recovery along-track MSS with wavelength about 20 km, which is similar to the best radar altimeters. However, ICESat-2 data are not as continuous as radar altimeter data. There are large gaps due to clouds and smaller gaps because the open ocean has low reflectance in the visible spectrum. Data gaps complicate the usage of ICESat-2 photon data on global scales.

At short wavelengths we find that ICESat-2 provides accurate and high-resolution profiles of surface waves in agreement with previous studies (Klotz et al., 2019). Moreover, data from a pair of strong and weak beams, separated by 90 m, can be used to estimate the dominant wave direction and wavelength. The wave reconstruction in this study (see Figures 2.6 and 2.7) is only tentative, yet it demonstrates ICESat-2's potential in monitoring global ocean wave conditions, especially in the south Pacific Ocean where in situ wave measurements are not usually available. Estimates of SWH from ICESat-2 data generally agree well with WAVEWATCH III hindcasts and independent buoy measurements (Klotz et al., 2019). As directional wave spectrum measurements from the Chinese-French Oceanography Satellite (CFOSAT) become available, the method proposed here could be further validated in the open-ocean without having to rely exclusively on wave model output.

We find that signals in the intermediate wavelength band from 3 to 20 km provided by ICESat-2 are 10 to 20 times more energetic than expected (Aucan and Ardhuin, 2013; Savage et al., 2017). The sea state is generally determined by a superposition of long-period, narrow-banded swell and short-period, locally generated wind seas, having a wide range of wavelengths

and directions (Sverdrup and Munk, 1947; Villas Bôas et al., 2017). ICESat-2 samples this 2-D wave field with a narrow beam in 1-D so the wavelength of surface waves observed by ICESat-2 is always greater than the true wavelength. For example, a 300 m swell having a 0.2 m amplitude and an orientation of  $87^\circ$  with respect to the ICESat-2 track will project into a signal with the same amplitude at 6 km wavelength. The three beams have a wide enough spacing to provide independent estimates of this projected swell, so averaging the three beams could reduce this projection by 1.7 times but not the 10-20 times needed for accurate measurements in this band. Note that pulse-limited radar altimeters do not suffer from this projection. A typical footprint diameter of a radar altimeter is 3 km at a 2 m SWH. Therefore there is a natural 2-D low-pass filter applied during the interaction of the radar pulse with the ocean surface waves. This suppresses all the wave energy shown in the spectra in Figure 2.9a. Nevertheless the wave noise re-appears as a smoothing of the radar return pulse that reduces the precision of measurement of the arrival time of the radar pulse.

To conclude, ICESat-2 is a highly capable instrument with the potential to yield new information about along-track surface waves over distances of 10 km or less, but it will not provide major improvements to the geoid in the open ocean, where many years of radar altimeter observations are providing increasingly accurate global marine gravity maps approaching 12 km wavelength resolution. However, ICESat-2 data may be valuable in regions where surface gravity waves have low amplitude, and the broad radar altimeter waveforms are corrupted by land reflections in a 5 km radius.

## **2.5 Acknowledgements**

This work was supported by the NASA SWOT program (NNX16AH64G, NNX16AH67G and 80NSSC20K1136), the NASA Ocean Surface Topography Science Team (NNX17AH53G)

and the Office of Naval Research (N00014-17-1-2866). The Generic Mapping Tools (GMT, Wessel et al., 2013) were extensively used in data processing.

## 2.6 Appendix

This supporting document contains 2 figures. Figure 2.11 shows the average power spectral density of ICESat-2 sea level anomaly in a Pacific box  $[-120^{\circ}/-100^{\circ}/-11^{\circ}/-1^{\circ}]$ . Figure 2.12 shows a sketch of a surface wave projected in the 1-D ICESat-2 orbit and how to reconstruct the wave direction and wavelength from a pair of strong and weak beams.

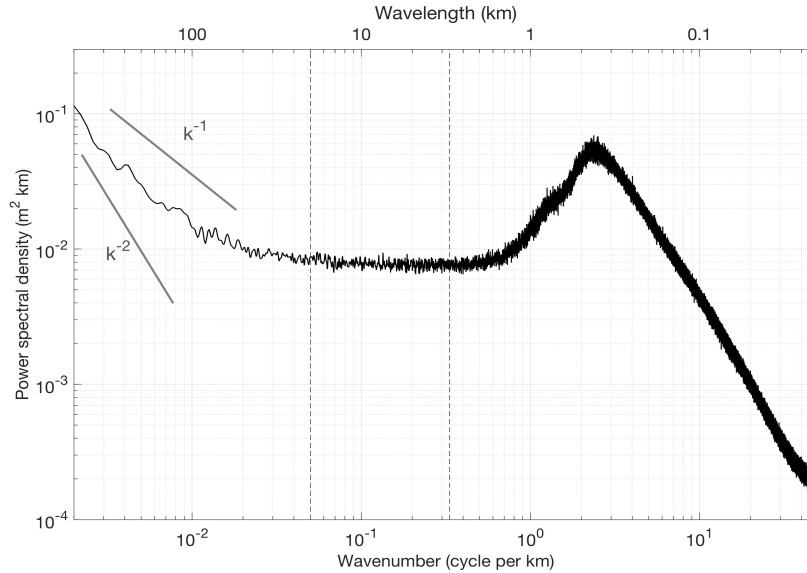


**Figure 2.11.** Averaged power spectral density of ICESat-2 sea level anomaly (w.r.t. to the mean sea surface) in a Pacific box  $[-120^{\circ}/-100^{\circ}/-11^{\circ}/-1^{\circ}]$  using the Lomb-Scargle method. This analysis uses 341 strong beams having more than 70 % cloud-free data. ICESat-2 photon height data are first low-pass filtered at 30 m. Vertical dashed lines indicate the separations between the three bands considered in this paper: large-scale flows (20-500 km), the shorter wavelength gravity waves ( $< 3$  km) and the more poorly understood intermediate wavelength (3-20 km) band. The  $k^{-1}$  and  $k^{-2}$  spectral slopes are labeled. The relative flat spectral slopes suggest that the long wavelength band is dominated by unbalanced flows and internal tides.

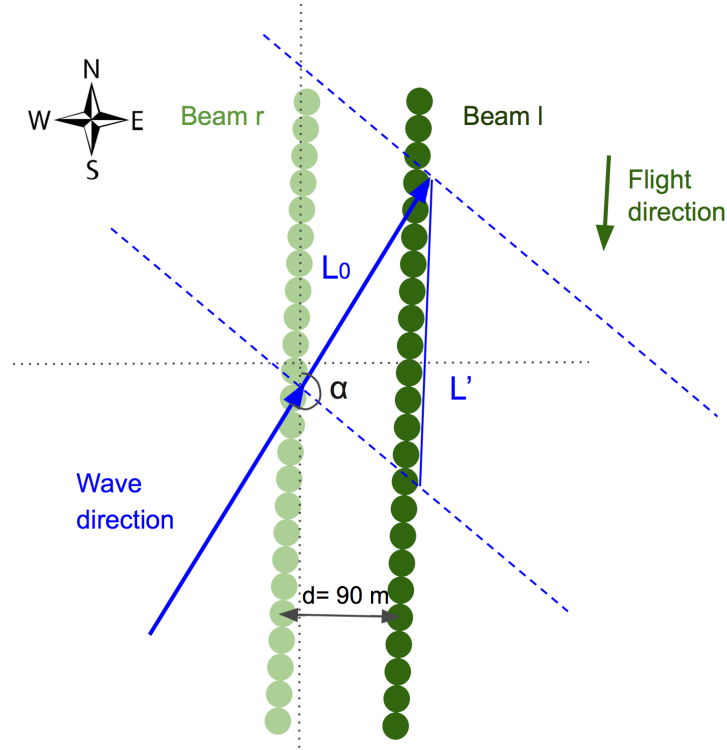


**Figure 2.12.** Sketch of a pair of ICESat-2 descending beams (flying from  $\theta = 2^\circ$ ) and a wave coming from southwest, forming an angle  $\alpha$ . Beam l and beam r are separated by a cross-track distance  $d$  of 90 m. The wavelength  $L_0$  is projected to be  $L' = L_0/|\cos \alpha|$  in the orbit direction. The wave in the observation of beam l leads beam r by a phase shift  $\beta$ , where  $\beta = 360^\circ d |\tan \alpha| / L' = 360^\circ d |\sin \alpha| / L_0$ . The true wavelength  $L_0$  and wave direction  $\theta = \alpha + \theta_0$  could be reconstructed from the projected wavelength  $L'$  and phase shift  $\beta$ , though comes with a  $180^\circ$  ambiguity. The along-track distance between beam l and beam r is about 2.5 km, which corresponds to  $\sim 0.35$  s shift in time during which surface waves only travel a few meters. This time shift appears in the coherence as a phase offset between the strong and weak beams. We neglected this phase offset and identified it as errors in the wave reconstruction. The  $\sim 2.5$  km along-track offset between the strong and weak beams is not shown here. There are 4 cases with the combination of ascending/descending track and beam l leads/lags beam r. Here we illustrate the descending track, with beam l leading beam r. The wave reconstruction scheme for the other three could be similarly derived.



## Chapter 3

# Global Mesoscale Ocean Variability from Multi-Year Altimetry: an Analysis of the Influencing Factors

Sea surface slope (SSS) responds to oceanic processes and other environmental parameters. This study aims to identify the parameters that influence SSS variability. We use SSS calculated from multiyear satellite altimeter observations and focus on small resolvable scales in the 30-100 km wavelength band. First, we revisit the correlation of mesoscale ocean variability with seafloor roughness as a function of depth, as proposed by Gille et al. (2000). Our results confirm that in shallow water there is statistically significant positive correlation between rough bathymetry and surface variability, whereas the opposite is true in the deep ocean. In the next step, we assemble 27 features as input variables to fit the SSS with a linear regression model and a boosted trees regression model, and then we make predictions. Model performance metrics for the linear regression model are  $R^2 = 0.381$  and mean square error =  $50.010 \mu\text{rad}$ . For the boosted trees model,  $R^2 = 0.563$  and mean square error =  $0.007 \mu\text{rad}$ . Using the hold-out data, we identify the most important influencing factors to be the distance to the nearest thermocline boundary, significant wave height, mean dynamic topography gradient, and  $M_2$  tidal speed. However, there are individual regions, that is, the Amazon outflow, that cannot be predicted by our model, suggesting that these regions are governed by processes that are not represented in our input features. The results highlight both the value of machine learning and its shortcomings

in identifying mechanisms governing oceanic phenomena.

### 3.1 Introduction

Sea surface slope (SSS) varies in response to a range of oceanic processes. On scales large enough to represent geostrophic flows, it is a measure of geostrophic velocity; on smaller scales, it varies with tides, surface waves, internal waves, eddies, etc. Large-scale ocean processes are generally well observed and have been studied since the era of satellite altimetry. Mesoscale oceanic variability (30-100 km), however, is less understood, as its signatures on the sea surface generally occur on scales smaller than the 100-200 km resolution of the widely used multimission sea surface height (SSH) product distributed by the Copernicus Marine Service (CMEMS; Ballarotta et al., 2019). Despite their small scales, mesoscale oceanic processes provide an essential link in the ocean's large-scale circulation and are associated with eddy kinetic energy generation and dissipation (Ferrari and Wunsch, 2009).

In this paper, our goal is to investigate the sea surface variability of small resolvable scales in the 30-100 km wavelength band and to contrast this with variability at scales greater than 100 km. We use SSS calculated from multiyear satellite altimeter observations as a metric for ocean variability. The major questions that we address are: how well can we characterize SSS variability, and what variables are needed to explain SSS variability? We know from previous studies (e.g., Gille et al. 2000; Nikurashin and Legg 2011) that surface variability is linked to bathymetry, seafloor roughness, and baroclinic instability, among other variables. Using satellite altimeter data, Gille et al. (2000) found evidence that mesoscale oceanic variability (with spatial scales from 80 to 160 km) is indirectly controlled by bathymetry: in ocean regions that are deeper than 4800 m, seafloor roughness is anticorrelated with SSS variability, implying that rough topography helps to dissipate mesoscale kinetic energy. In contrast, in shallow waters, seafloor

roughness and sea surface slope variability are correlated, implying that mesoscale variability is generated over rough topography. Nikurashin and Legg (2011) used numerical simulations to show that the energy from large-scale internal tides to smaller-scale internal waves depends on seafloor roughness, tidal amplitudes, and the Coriolis frequency. While the comparisons of Gille et al. (2000) provided a statistical assessment, depth-dependent impacts of roughness could explain less than 10% of the overall variability in SSS. Here we aim to learn what other parameters might influence small-scale SSS variability.

We address the major question in two ways: (i) How well can we predict oceanic variability on global scales, and what fraction of the global variance can we predict? (ii) Are there particular regions that are unusual and cannot be predicted? For places where the surface variability responds to a particular local effect, (e.g., the Amazon outflow), can the variability be represented using a statistical model derived with machine learning?

We aim to answer the above questions by using three statistical methods: (1) Correlation analysis, in which we revisit the conditional correlation between seafloor roughness versus SSS variability as a function of depth, as proposed in Gille et al. (2000), with updated datasets, and we explore linear correlations between sea surface variability and other variables. (2) Machine learning using a linear regression approach. (3) Machine learning with a boosted trees algorithm. Both machine learning methods take in multiple features to predict the sea surface variability, analyze the relevance of each feature, and discuss prediction failures. While conditional correlation analysis quantifies the linear dependence between variables, it lacks the flexibility to handle nonlinear dependencies on multiple variables. The linear regression model is straightforward, and it assumes that labels (what we are attempting to predict or forecast, i.e. SSS variability in this study), are a linear combination of different features. While this assumption will prove to be inadequate to explain all variability, the linear regression is a base model that is able to identify linear relations between the SSS variability and features. In contrast to conventional

linear regression, the boosted tree model can capture nonlinear relationships between the features and the outcome. It uses the boosting method that sequentially combines decision trees, in a way that each new tree fits the residuals from the previous step so that the model improves (Friedman, 2002). Decision trees use a greedy algorithm that finds the optimal data split solution for each node, which is a split on a feature at a specific value, resulting in the largest information gain (Quinlan, 1986). Both models assist in understanding the governing factors of SSS variability in our case. In Section 3.2.2 we introduce strategies for ranking features, i.e., selecting governing factors.

We estimate the global ocean variability in the form of SSS variability using satellite altimetry profiles from Geosat, Envisat, Cryosat-2, Jason 1/2, Altika and Sentinel-3A/B collected from 1993 to 2021 (an updated version of the dataset as in Sandwell et al., 2019). SSS is the along-track derivative of SSH. Thus it achieves finer spatial resolution than SSH by “whitening” the red spectrum slope of SSH and is more sensitive to high-wavenumber signals. Note that this is a 1-D along-track slope, so it only approximates a 2-D slope estimate. The slope estimates come from a variety of directions depending on the inclination of the satellite orbit. Sandwell et al. (2019) showed that SSS variability from multi-year repeat and non-repeat altimetry missions is able to reveal oceanic processes with scales as small as 25 km. The combination of multi-year satellite altimetry profiles provides a dense ground track coverage at the cost of losing temporal resolution. In contrast, the gridded SSH product using multi-satellite data distributed by CMEMS, has a temporal resolution of 10 to 33 days and a spatial resolution of about 100-200 km (Ballarotta et al., 2019; Taburet et al., 2019). The coarse spatial resolution of the multi-satellite data is restricted by the wide cross-track distance and instrument noise (Fu and Ubelmann, 2014). This product is not able to fully capture mesoscale oceanic activities and is thus not adopted in our study.

We study the SSS variability in two wavelength bands: (1) a band encompassing

mesoscale variability as well as larger submesoscale features (30-100 km). As a shorthand, we refer to this band as the mesoscale; (2) the large-scale band ( $>100$  km). The mesoscale band is generally hard to observe on a global scale. It contains the variation of unbalanced wave motions and the mesoscale eddies that include coherent vortices, filaments, squirts and spirals. Unbalanced wave motions are mostly attributed to internal tides or waves, and they are generally greater in amplitude over rough topography (i.e., the Hawaiian Ridge) or in highly stratified zones (i.e., the Amazon shelf). The mesoscale eddies emerge from the instabilities of strong geostrophic flows, and they contain the majority of oceanic kinetic energy (Zhang and Qiu, 2018). Large-scale SSS variability is well-characterized and it is related to balanced geostrophic flows which have large values of mean SSS, i.e. western boundary currents and the Antarctic Circumpolar Currents (ACC). Slight perturbations to the large-scale mean SSS lead to variability at large spatial scales. The transition scale that delineates balanced geostrophic flows and unbalanced wave motions depends sensitively on local mesoscale eddy variability and varies with time (Qiu et al., 2018). The 100 km delineation here is an empirical choice. While there is no consensus on the transition scale, it is generally short (below 40 km) in eddy-intensified western boundary currents and in the ACC, and it increases equatorward in relative stable regions (40-100 km in subtropical and subpolar gyres;  $> 200$  km in the tropical oceans) (Qiu et al., 2017; Qiu et al., 2018). The 30-100 km mesoscale band contains both unbalanced wave motions (internal tides, near-initial flows) and balanced geostrophic flows. The dominant component of the flow is geographically and temporally dependent.

## 3.2 Data and Methods

### 3.2.1 Data

#### Sea surface slope variability

In this paper, we calculate SSS variability in the mesoscale band (30-100 km) and large-scale band ( $>100$  km) using multi-year along-track altimetry. Calculation steps are described below.

We take the along-track profiles from Geosat, Envisat, Cryosat-2, Jason 1/2, SARAL/Altika and Sentinel-3A/B collected from 1992 to 2021. Standard 1 Hz geophysical data records are inadequate for this analysis because the retracking of the waveform does not account for the high correlation between significant wave height (SWH) and arrival time (Sandwell and Smith, 2005; Zaron and DeCarvalho, 2016). Moreover, the 1 Hz boxcar averaging aliases noise at less than 1 Hz ( $\sim 14$  km wavelength) into the 30-50 km wavelength band. Finally, to achieve a uniform quality among the various altimeters, one must retrack, filter, and edit the raw waveform data in a consistent way. To retrack raw waveform data (except for Cryosat SAR/SIN and Sentinel-3A/B), we adopt a two-pass method that effectively reduces the wave height noise and improves the range precision of altimeter echoes by a factor of 1.5-1.7 (García-García and Ummenhofer, 2015; Zhang and Sandwell, 2017). We edit 20 Hz waveform data using flags provided in the level 1 product. We then apply a Parks-McClellan low-pass filter with half gain at 6.7 km and downsample data to 5 Hz. We apply geophysical corrections, including wet and dry troposphere delay, inverse barometer effect, and solid Earth and ocean tides (FES2014, Carrère et al., 2016). We further edit data with residuals from the EGM 2008 model greater than 3 standard deviations (typically  $> 30$  microradians). We apply a second Parks-McClellan low-pass, derivative filter with half gain at 8.3 km to all profiles and form along-track SSS. We apply local geoid corrections (Sandwell and Smith, 2014) and remove the mean SSS to obtain slope anomalies that reflect oceanic variability, wave height noise, and tide model error.

For isotropic geostrophic flows, SSS variability is linearly related to eddy kinetic energy:  $E_k = \langle v'^2 \rangle = \langle (\partial \eta' / \partial l)^2 \rangle g^2 / f^2$ , where  $E_k$ , eddy kinetic energy, is defined as the time-averaging of squared surface geostrophic velocity perturbations  $\langle v'^2 \rangle$ ,  $g$  is gravity,  $f$  is the Coriolis parameter,  $\partial \eta' / \partial l$  is the along-track SSS anomaly. Thus SSS variability  $\sqrt{\langle (\partial \eta' / \partial l)^2 \rangle}$  represents eddy kinetic energy for flows on scales large enough to be geostrophically balanced. The relation does not apply for flows that are not geostrophically balanced, either because they represent small-scale ageostrophic motions or because they occur in equatorial regions, where the Coriolis parameter approaches zero. SSS variability with wavelengths shorter than 30 km is mostly buried in wave height noise. Thus we apply a 30-km Gaussian low-pass filter to reduce noise (Sandwell et al., 2019).

We sort the SSS anomalies into 7 by 5 arc minute blocks and use the absolute median value in each block to represent oceanic variability. The mesoscale and large-scale SSS variability are shown in Figure 3.1. In the mesoscale band, we can see patterns of variability that are potentially consistent with signals due to internal tides as well as horizontally sheared boundary current motions. For example, there is strong variability associated with internal tides over rough topography (the Mid-Atlantic Ridge, the Southwest Indian Ridge, and the Hawaiian Ridge) and continental shelves (the Amazon shelf and the Mascarene Basin). There is also strong SSS variability in the vicinity of western boundary currents and the ACC. On large scales, the strong SSS variabilities are always associated with western boundary currents and the ACC, where the mean SSS are large.

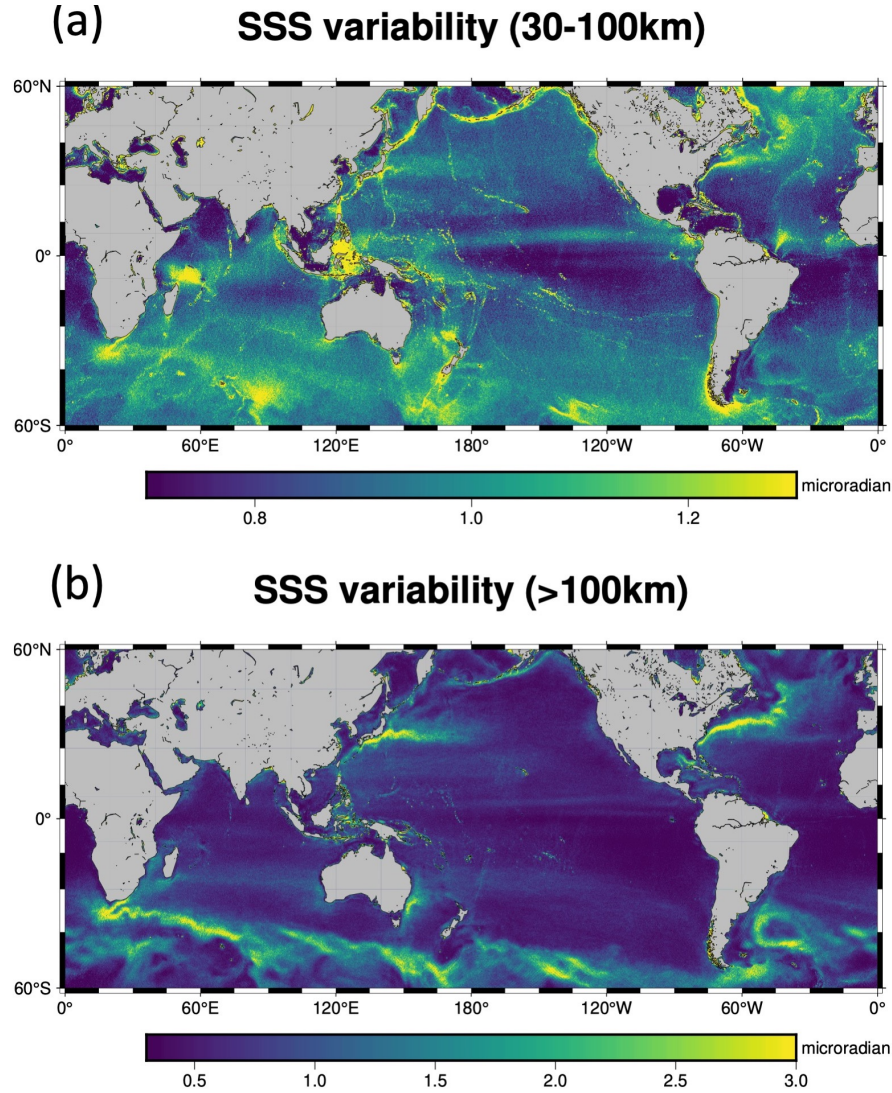


**Figure 3.1.** (a) Mesoscale SSS variability (30-100 km). (b) large-scale SSS variability (>100 km). 1 microradian equals 1 cm change in height over a horizontal distance of 10 km. All plots are at 7 by 5 arc minute resolution using a Mercator projection. All land is gray. Note that the color scales for (a) and (b) are different.

### environmental parameters

For the correlation analysis, we use bathymetry, seafloor roughness, and SSS variability, to revisit the relation between roughness and eddy kinetic variability as a function of seafloor depth as in Gille et al. (2000). For machine learning approaches, we use 27 features (listed below) as input variables to build a linear regression model and a boosted tree model to predict the SSS



variability. Our analysis screens out regions poleward of  $60^\circ$ , where strong seasonal sea ice contaminates oceanic signals. The Jason-1/2 orbit was designed with a  $66^\circ$  latitude inclination. We exclude all land, lakes, ponds, and semi-enclosed seas including the Mediterranean, Gulf of Mexico, and Caribbean Sea. We also exclude coastal regions where ocean depth is less than 100 m. All features are processed to have consistent spatial coverage ( $60^\circ\text{S}$  to  $60^\circ\text{N}$ ) and resolution (7 by 5 arc minutes). We normalize features such that the normalized features have similar ranges and comparable variances. We retain the sign of latitude; we linearly scale the absolute latitude to range from 0 to 2; we apply a scaler to all other features that subtracts the median, and we scale each feature to the interquartile range. The centering and scaling statistics of the scaler are based on percentiles and are therefore robust to large marginal outliers. The 27 features are either associated with the solid Earth or the dynamic ocean. Features are described below and shown in Figure 3.2.

### *1. Seafloor roughness*

Seafloor roughness is the root-mean-square, or RMS height of short wavelength bathymetry (we use a wavelength range of 50-160 km in this study). The roughness directly derived from SRTM15+V2.3 predicted bathymetry (Tozer et al., 2019) is underestimated, because the gravity anomalies from small structures including abyssal hills, small seamounts etc., are attenuated in altimetry measurements. Goff (2010) put forward that the statistical properties of abyssal morphology can be related to the gravity field that is derived from satellite altimetry using the upward continuation formulation. We produce a roughness map by adding back the latest abyssal hill RMS height from Goff (2020) to predicted bathymetry in the following steps:

- (i) square the Goff (2020) RMS height and replace with 0 over regions measured by ship soundings;
- (ii) apply a high-pass Gaussian filter to the SRTM15+V2.3 predicted bathymetry at 160

km then square the result;

(iii) combine the above two datasets and apply a low-pass Gaussian filter with 0.5 gain at 50 km to eliminate contamination from wave height noise in satellite measurements;

(iv) take the square root of the dataset in step (3) to get RMS roughness, which is the square-root of the average squared bathymetry deviation about a linear trend. We recovered the abyssal hill roughness while keeping all ship soundings untouched. The uncharted small seamounts are not taken into consideration in this study.

## *2. Smooth seafloor roughness*

Seafloor roughness is low-pass filtered using a Gaussian filter with half gain at 500 km to obtain the smooth seafloor roughness. This captures the locations of large-scale rough seafloor and is less sensitive to estimation errors than roughness itself.

## *3. Bathymetry*

We use the STRM15+V2.3 15 arcsecond resolution bathymetry map which includes > 33.6 million multibeam and single beam measurements (covering 15% of the ocean; Wöfl et al., 2019) and retracked range measurements from Geosat, Envisat, Cryosat-2, Jason-1/2 and SARAL/Altika (Tozer et al., 2019).

## *4. Ocean depth slope*

Internal tides are generally generated over variable bottom topography such as continental slopes (Baines 1982). Small topography structures like abyssal hills and seamounts associated with slopes up to 0.2, are not fully captured in the SRTM15+V2.3 bathymetry map. These features are potential sites for internal tide generation. The synthetic bathymetry map SYN BATH includes the statistics of abyssal hills and Gaussian-shaped small uncharted seamounts (Sandwell et al., 2022). We use the magnitude of the vector gradient of

the SYNBATH to represent the ocean depth slope.

#### *5. Vertical gravity gradient*

Vertical gravity gradient (VGG) is the vertical derivative of gravity anomaly and is linearly related to the derivative of the mean SSS through Laplace's equation (Sandwell, 2022). It describes the bumps and dips from the topography of the seafloor. We use the 1 arc minute marine VGG of the SRTM15+V2.3 product (Tozer et al., 2019).

#### *6. Free-air gravity*

Free-air gravity is the negative radial derivative of the disturbing potential evaluated on the geoid (Sandwell, 2022). We use the 1 arc minute marine free-air gravity anomalies of the SRTM15+V2.3 product (Tozer et al., 2019). In Figure 3.6 "FA\_gravity" represents free-air gravity.

#### *7-8. Seafloor spreading rate and crustal age*

Seafloor spreading rate and oceanic crustal age are two fundamental geophysical variables. Oceanic crusts are young at newly generated mid-ocean ridges. Spreading rate is the rate at which an ocean basin widens due to seafloor spreading. It ranges from less than 40 mm/year at the Mid-Atlantic Ridge to more than 100 mm/year at the East Pacific Rise. We use the seafloor spreading rate and oceanic crustal age from Seton et al. (2020). The dataset is based on magnetic anomaly identifications and the plate tectonic model of Müller et al. (2019). Regions of present-day deformation are not available and are replaced with zeros in the normalized datasets.

#### *9. Mean dynamic topography*

The mean dynamic topography (MDT) is the current relief that shows steady-state general circulation with gyres and associated western boundary currents. We use the DTU10 MDT, which is the difference between the 12-year averaged sea surface and the EGM2008 geoid (Andersen and Knudsen, 2009). It measures the expected sea surface height due to currents like the Gulf Stream and the Kuroshio.

#### *10. Mean dynamic topography gradient*

The gradient of dynamic topography is proportional to the geostrophic component of ocean surface current speed. We take the vector gradient of the MDT topography, and use the magnitude as MDT gradient.

#### *11-14. $K_1$ and $M_2$ tidal amplitude and current speed*

Barotropic tides are the major origin of internal tide generation, which leads to SSS variability. We use the two largest components, the  $K_1$  and  $M_2$  tides, with their tidal amplitude and surface current speed from the FES2014 tide model as features. FES2014 tide model is the latest finite element solution tide model assimilating long-term altimetry data and tidal gauges (Carrère et al., 2016). Note that barotropic tides are removed from along-track altimetry observations.

#### *15. Sediment thickness*

The seafloor is covered in varying amounts of sediment, and the thickness ranges from a few tens of meters in the open ocean, to several kilometers near the coasts. We use the global ocean sediment thickness map, GlobSed, derived from seismic reflection data (Straume et al., 2019).

### *16-18. Stratification $N^2$*

Internal tides are generated in stratified water by the interaction of barotropic tides over rough bottom topography (Garrett and Kunze, 2007), and stratification is a key factor in learning the SSS variability. Stratification can be represented by the buoyancy frequency  $N$ , or the Brunt–Väisälä frequency. Using the annual statistical mean salinity and temperature data from the World Ocean Atlas 2018 (WOA18), we evaluate the mean buoyancy frequency  $N$  for the mixed layer (0-100 m), upper ocean (100-300 m) and deep ocean (300-2000 m) with the Gibbs SeaWater (GSW) oceanographic toolbox (McDougall and Barker, 2011).

### *19. $M_2$ tide critical slope*

Critical slope is the bottom slope that equals the angle at which rays of internal waves of tidal frequency propagate. It is a key parameter governing the internal tide generation. We estimate the critical slope of the  $M_2$  tide following equation (1) of Becker and Sandwell (2008). The calculation uses WOA18 salinity and temperature data to calculate the buoyancy frequency  $N$  at different depths and then extrapolates  $N$  to the seafloor, assuming an exponential function of depth (St. Laurent and Garrett, 2002).

### *20. Fractions of slope above critical*

The smallest seamounts that are detectable in the satellite altimetry could be 800 m in height and 4 km in radius (Gevorgian et al., 2021). Our spatial resolution of 7 by 5 arc minutes is coarser than the scales of small tectonic structures including seamounts. We use the 15 arc second SYNBATH bathymetry map (Sandwell et al., 2022) to calculate seafloor slope, then calculate the fractions of super critical slope of  $M_2$  tide in each 7 by 5 arc minute grid. In Figure 3.6, we use “Fractions” to represent fractions of slope above critical.

## 21. *Mixed layer depth*

The ocean mixed layer is a surface layer of nearly uniform density resulting from stirring of surface waters by the wind or heat fluxes. As a feature, we use the 12-month average of the monthly mean mixed layer depth (MLD) product derived from almost 2,450,000 Argo profiles collected through March, 2021 (Holte et al., 2017).

## 22-23. *Absolute latitude and the sign of latitude*

Some ocean activities are tied to the latitude., i.e, ocean eddies scale with the Rossby radius, which varies with latitude; zonal jets are also shown to populate every part of the ocean (Maximenko et al., 2005). We use the absolute latitude and the sign of latitude (1 for the Northern Hemisphere and -1 for the Southern Hemisphere) as features in this study. We avoid using longitude as a feature. Using both the longitude and latitude as features would allow the model to take a shortcut using geographic coordinates in training, instead of learning the relations between input physical features and output labels as we expect.

## 24. *Reciprocal of latitude*

The reciprocal of Coriolis frequency connects the SSS to the EKE, or the average geostrophic flow speed. Coriolis frequency is defined as  $f = 2\omega \sin \psi$ , where  $\psi$  is the latitude,  $\omega$  is earth's angular speed. Coriolis frequency  $f$  sets the lower bound for the frequency of internal wave motions. For this study, we neglect the constants and slightly modify the term to be  $1/(\sin |\psi| + 0.2)$  where 0.2 is added to the denominator to avoid a singularity at the equator.

## 25. *Ocean basins*

Different basins of the ocean exhibit large-scale differences in stratification and circulation. To allow for the possibility of basin-scale variability that is not readily represented by the other variables, we identify each ocean basin with an integer from -1 to 4 to distinguish: the Southern Ocean, the Indian Ocean, the north Pacific, the south Pacific, the north Atlantic, and the south Atlantic.

#### *26. Distance to the nearest thermocline boundary*

A thermocline is the transition layer where temperature decreases rapidly from the mixed upper layer of the ocean to much colder deep water. It is associated with high stratification and creates conditions for internal tide generation. We use the 12 month average of the monthly maximum mean mixed-layer depth product collected from Argo profiles to represent the thermocline depth (Holte et al., 2017). We pick out the boundary where the thermocline intersects the ocean floor, and we calculate the nearest distance to the boundary as a feature. In Figure 3.6, “Distance” denotes distance to the nearest thermocline boundary.

#### *27. Significant wave height*

Winds and wave heights are highly correlated. Most ocean surface currents are caused by wind, and surface gravity waves are also generated by the friction between wind and water. We use the multi-year mean significant wave height (SWH) as a feature. SWH is provided in the waveform data in the along-track satellite altimetry product.

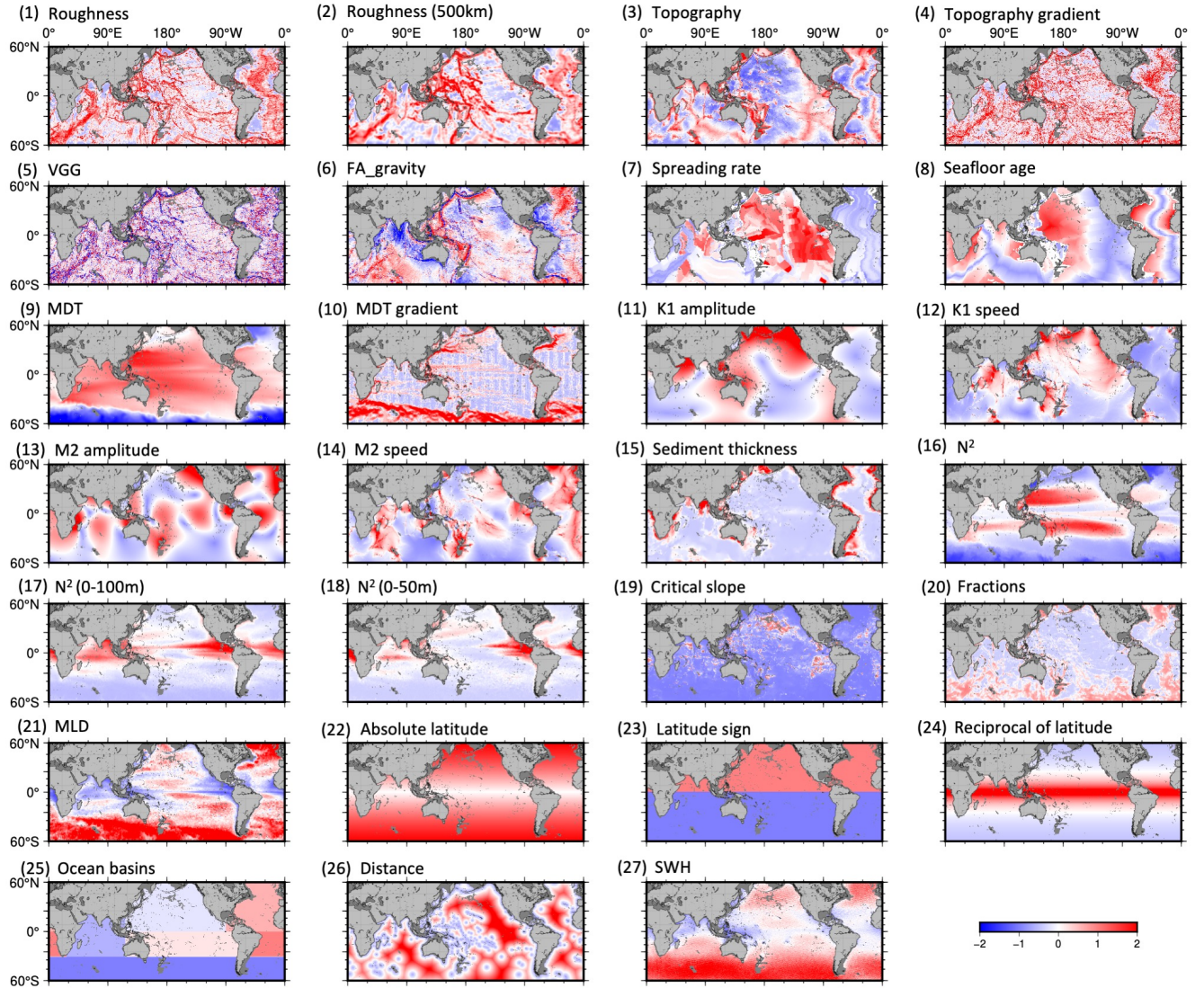


**Figure 3.2.** Normalized environmental parameters used in this study. Land is masked as light gray. All areas excluded (lakes, ponds, inland ocean and coastal areas) are masked as dark gray. All plots are at 7 by 5 arc minute resolution using a Mercator projection.

### 3.2.2 Methods

#### Correlation analysis: revisiting Gille et al. (2000)

Correlation is a statistical method that measures the strength of association between two linearly related variables and the direction of the relationship. Gille et al. (2000) calculated the Pearson correlation coefficients between seafloor roughness and eddy kinetic energy as a function of depth. Their analysis built on a hypothesis that seafloor roughness could serve either



to dissipate eddy kinetic energy by exerting friction at observed scales, or it could be a source of energy by generating lee waves or instabilities or steering eddies. Roughness was computed by band-pass filtering Smith and Sandwell (1997) bathymetry to retain wavelengths between 80 and 160 km and then computing RMS height. Eddy kinetic energy  $E_k$  was derived from along-track slopes of TOPEX, ERS-1/2 using the geostrophic relationship and assuming eddy variability to be isotropic. Along-track slopes were low-pass filtered to retain signals with wavelengths longer than 80 km, and data equatorward of  $20^\circ$  were omitted because of errors associated with small Coriolis parameter  $f$ . They found a positive correlation between roughness and  $E_k^{1/2}$  in regions shallower than 3000 m and a negative correlation at depths greater than 4800 m.

In this study, we repeat the correlation analysis of Gille et al. (2000) using updated SSS variability, bathymetry and roughness datasets as described in Section 3.2.1. We bin the roughness and SSS variability (30-100 km,  $>100$  km) by local depth in each 100 m range, and as a function of depth calculate the Pearson correlation coefficient between roughness and SSS variability. The result is shown in Figure 3.3.

For each 100 m depth range, we fit the corresponding 30-100 km SSS variability as a linear function of roughness and use this information to predict SSS variability. We then combine the predictions made over each depth range to map predicted SSS variability (Figure 3.4a) and the differences with the observed SSS variability (Figure 3.4b). We also predicted the large-scale SSS variability ( $>100$  km) (Figures 3.5a and 3.5b).

Mean squared error (MSE) and  $R^2$  serve as metrics of model performance. MSE is the second moment of the error (L2 norm) and incorporates both the variance of the estimator and its bias. It is computed as (Sammut and Webb, 2011):

$$MSE = \frac{1}{N} \sum_{i=1}^N (y_i - \hat{y}_i)^2 \quad (3.1)$$

The  $R^2$  score is a measure of the amount of variance in the predictions explained by the dataset.  $R^2$  values near 1 indicate better predictions.  $R^2$  is defined as (Devore, 2011):

$$R^2 = 1 - \sum_{i=1}^N (y_i - \hat{y}_i)^2 / \sum_{i=1}^N (y_i - \bar{y})^2 \quad (3.2)$$

where  $y_i$  is the  $i$ th observation,  $\hat{y}_i$  is the  $i$ th prediction, and  $\bar{y}$  is the mean value of observed SSS variability. The total number of observations,  $N$ , is 2,677,475 grid points in this study. We assume that the prediction at each data point has the same uncertainty.

### Linear Regression Model

Linear regression assumes linear relationships between the input features and the output labels. It can be computed via ordinary least squares fitting, which minimizes the sum of the squared residuals. Although SSS variability may have non-linear or high-order dependences on the environmental parameters, we do not consider higher-order terms and focus only on the linear correlation between SSS variability and environmental variables. We adopt the linear regression model from the scikit-learn library (Pedregosa et al., 2011) to build models between the SSS variability and 27 environmental parameters and to evaluate model performance as well as feature importance.

We compute a global mesoscale SSS variability (30-100 km) prediction map using the linear regression model and evaluate model performance using the  $R^2$  and MSE metrics. Steps to construct the predicted map are as follows: (1) First, we divide the ocean into 64 blocks of equal area (see Figure 3.8 in the appendix for the block separation). (2) We make predictions over each block. For each unique block that is used as a test set, we randomly select 44 out

of the remaining 63 blocks as training datasets (around 70%). We adopt all 27 environmental parameters as features and SSS variability (30-100km) as labels (i.e. the predicted variable) and train a linear regression model, then use the model to predict SSS variability over the selected block. (3) We then shuffle the training datasets 30 times. Each time we randomly select 44 out of 63 blocks as training datasets and repeat the above step to get predictions over the chosen block or test set. (4) We use the average of the 30 predictions, concatenate the averaged predictions over each unique block, and make a global prediction-only map (Figure 3.4c). The training strategy of splitting the data into 64 geographical bins and using the input from different separate regions to make predictions over a specific region ensures model generalizability and prevents the model from simply learning local information. The differences between predicted and observed SSS variability (30-100 km) are shown in Figure 3.4d. We also run the same processes to obtain the prediction map for the large-scale SSS variability ( $>100$  km; Figures 3.5c and 3.5d. Note that  $R^2$  and MSE are calculated using the prediction map (test sets only) and observations.

We use two methods to evaluate the feature importance of the linear regression model: (1) feature forward selection; (2) feature ablation. The details are described below:

(1) Forward selection:

The forward selection algorithm starts with a model with zero features and iterates through all single-feature models to find one that is most predictive (for example, with the smallest L2 norm); picks the feature; then for all the remaining features, considers adding each of them to build a two-feature model, by including whichever second feature is most predictive; always includes the feature giving the biggest marginal gain in predictive power in the presence of all other selected features. The order in which features are selected is a measure of feature importance. We use the sequential forward selection method from the scikit-learn library to select and rank features that are most relevant

to the SSS variability. We evaluate model performance using 5-fold cross-validation, in which data are split into 5 groups; each unique group will be used as a test set and remaining groups will be used as a training set; we train a model, retain the evaluation score (L2 norm), and then summarize the model performance using the 5 evaluation scores.

(2) Feature ablation:

Feature ablation measures how much the model performance is degraded by deleting one feature. First, we use all  $M$  (27 in this study) features and 70% of data as training datasets to train a linear regression model. (The process can also be applied with any other machine learning model.) Models with  $M-1$  features obtain worse performance over the test dataset, which comprises the remaining 30% of the data, for example, with increased MSE compared to the model using all available  $M$  features. The reduction in performance, as quantified by the L2 norm, provides a measure of the importance of the deleted feature.

### **Boosted Trees Algorithm**

The gradient boosted trees algorithm is an ensemble of decision trees as weak learners. Each tree tries to fit the residuals from previous models. All those trees are trained by propagating the gradients of errors throughout the system. We implement the boosted trees algorithm using the Light Gradient Boosted Machine (LightGBM, Ke et al., 2017). LightGBM is a fast and efficient framework. It splits the tree leaf-wise using a histogram-based method for selecting the best split and buckets continuous feature values into discrete bins thus lowering memory usage. It works with large datasets with ease and results in much better accuracy, which can rarely be achieved by any of the existing boosting algorithms. The main drawback of gradient boosted trees is that finding the best split points in each tree is time consuming.

We compute a global prediction-only SSS variability (30-100 km) map with the boosted trees model, again using 27 environmental parameters as features as described in Section 3.2.1. The steps to calculate predictions are basically the same as for the linear regression model (as discussed in Section 3.2.2) with the exception that for each model we randomly select 44 out of the remaining 63 blocks as training datasets, and the other 19 blocks as validation datasets. Figure 3.4e shows the prediction-only map, and Figure 3.4f shows differences with observations. We evaluate the model performance through the  $R^2$  score and the MSE.

We identify the dominant features in the boosted trees model using two methods: (1) feature ablation; (2) feature importance inbuilt by the boosted trees model. Feature ablation is introduced in Section 3.2.2. For method (2), we train a boosted trees linear regression model with feature sub-sampling (0.8) and bagging (bagging fraction 0.7 and bagging frequency 5) to avoid over-fitting and use the feature importance returned by the model’s split gain.

## 3.3 Results

### 3.3.1 Correlation with Roughness

As a baseline for the machine learning analyses, we first assess the skill of the roughness correlation of Gille et al. (2000) in predicting SSS. Figure 3.3 shows the correlation coefficients between SSS variability and seafloor roughness as a function of depth. The blue curve, indicating the correlation between roughness and full-scale SSS variability ( $>30$  km), resembles Figure 2a in Gille et al. (2000), which focused on the 80-160 km wavelength band. Both show that there is positive correlation between roughness and SSS variability in regions shallower than 3000 m and negative correlation in regions deeper than 5000 m. The correlation with large-scale SSS variability ( $>100$  km, green curve) is similar to the correlation with full-scale SSS variability (blue curve) in the deep ocean. It has reduced values at shallow water, and the correlation is

sometimes insignificant. The negative correlation between roughness SSS variability ( $>100\text{km}$ ) and roughness at depths greater than 5000 m are mostly attributed to the Argentine Basin, where the energetic Zapiola Anticyclone circulates counterclockwise over smooth abyssal plains (Saraceno et al., 2009). The negative correlation also indicates that the variation of geostrophic flows is not related to seafloor roughness. At mesoscales (30-100 km), the correlation between seafloor roughness and SSS variability is basically positive at all depth levels, and the correlation is much higher in shallow water compared with large-scale flows. This pattern of positive correlation suggests that the mesoscale oceanic variability is generated as a response to rough topography.

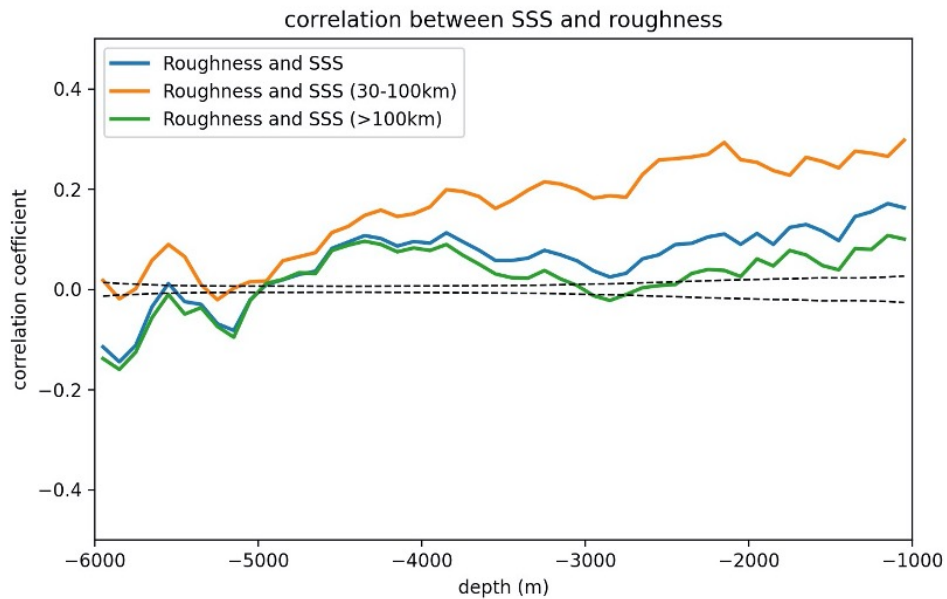


**Figure 3.3.** Correlation coefficients of seafloor roughness versus SSS variability in three wavelength bands ( $>30\text{km}$  or full band, 30-100km,  $> 100\text{km}$ ) as a function of ocean depth. Black dashed lines are the 95% confidence intervals beyond which correlation coefficients are statistically reliable.

### 3.3.2 Predicted SSS Variability

#### Mesoscale SSS variability prediction

We have introduced three statistical methods for producing predictions of SSS variability in Section 3.2.2. We show the predicted SSS variability and prediction errors for the mesoscale band in Figure 3.4.

Using the correlation between seafloor roughness and SSS variability as a function of ocean depth, we map global predicted mesoscale SSS variability (Figure 3.4a). The prediction is far from being realistic. It is only capable of capturing SSS variability over regions with rough topography, for example over the slow-spreading ridges (the southwest Indian Ridge and the Mid-Atlantic Ridge), fracture zones (the Challenger Fracture Zone), and hotspot chains (the Emperor Seamount Chain and the Louisville Seamount Chain). The difference with the observed SSS variability (30-100 km) is shown in Figure 3.4b. The prediction error is large over western boundary currents and the ACC. This model has an  $R^2$  score of 0.064 and an MSE of  $0.015 \mu\text{rad}^2$  on a global scale.

The linear regression model, which uses 27 features as variables to fit the SSS variability (30-100 km), makes predictions over each individual block. The prediction map that concatenates the predictions is shown in Figure 3.4c and the prediction errors in Figure 3.4d. This time the predicted variability map is able to capture signatures of most geostrophic flow instabilities, and unbalanced flows over rough topography. It has an  $R^2$  score of 0.362 and an MSE of  $0.010 \mu\text{rad}^2$ . It also shows significantly reduced prediction errors in the Southern Ocean compared with the correlation analysis (Figures 3.4d compared to 3.4b).

The non-linear boosted trees model provides the best prediction (Figure 3.4e) among the three models. On global scales, the  $R^2$  score is 0.563, the MSE is  $0.007 \mu\text{rad}^2$ , and the model

provides realistic predictions. For example, it predicts high SSS variability in the Mascarene Basin; the prediction in the tropical Pacific agrees well with observations. However, this model, like the other two models, fails to predict the internal tide variability in the Amazon outflow. We hypothesize that this local variability is related to physical processes that are not accounted for in our features. There are some discontinuities at the block edges (e.g. a zonal stripe above the Mascarene Ridge) arising from the fact that predictions for each block are independent. Using the average from 30 rounds of training/predicting greatly reduces the discontinuities.



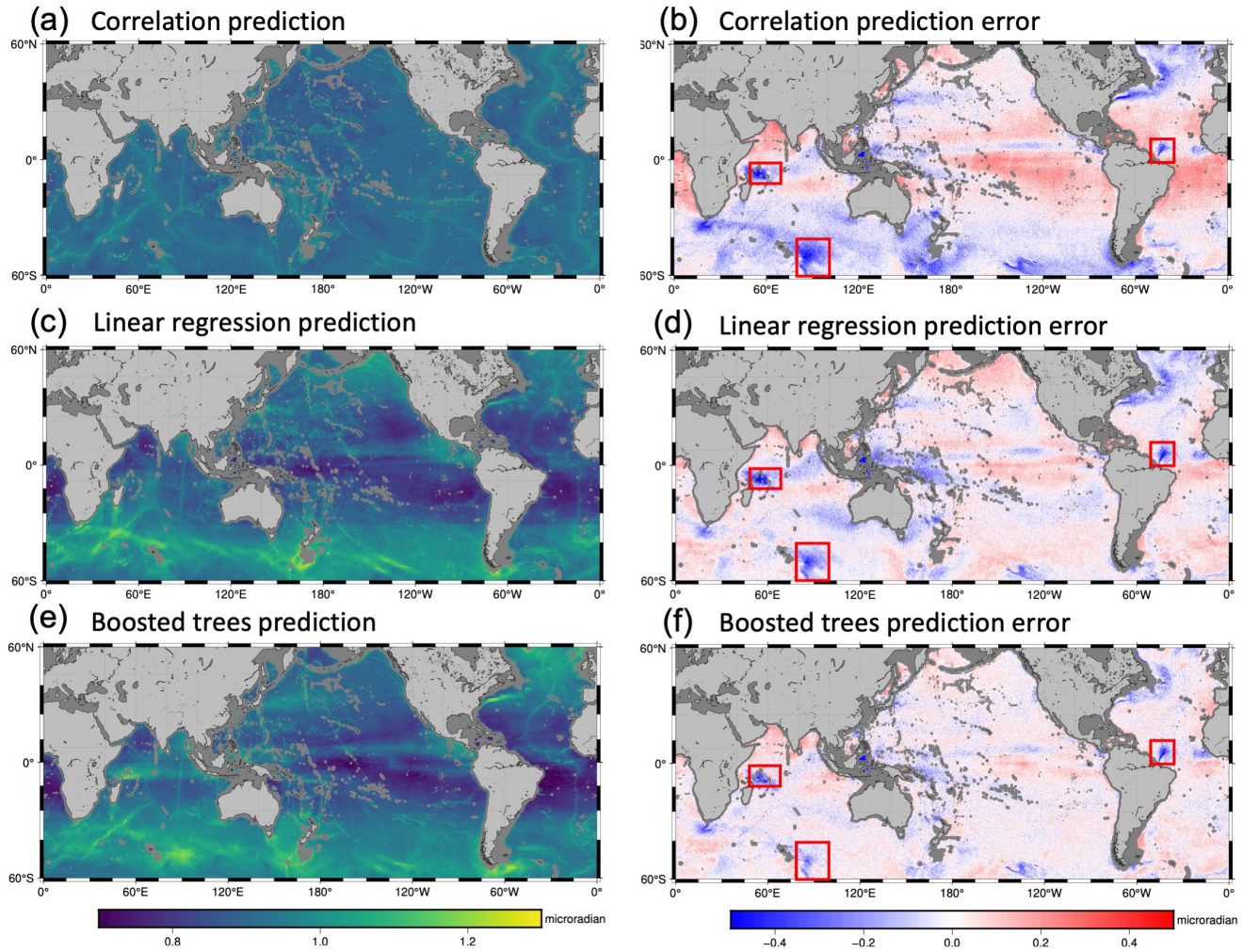


**Figure 3.4.** (a) The predicted mesoscale SSS variability map (30-100km) and (b) the associated prediction error using the correlation between seafloor roughness and SSS variability (30-100km) as a function of seafloor depth. (c) and (d) are the same as (a) and (b) except for using the linear regression model. (e) and (f) are the same as (a) and (b) except for using the boosted trees model. Regions with prediction failures are enclosed in red boxes in (b), (d) and (e).

### Large-scale SSS variability prediction

At large scales, SSS variability ( $>100$  km) is well categorized, and it is expected to be dominated by western boundary currents and the ACC, regions where the mean SSS is large. In general, large-scale SSS variability ( $>100$  km) is linearly related to the MDT gradient, which represents the strength of geostrophic flows. We expect that both the linear regression model and the boosted trees algorithm, which use MDT gradient as a feature, should capture the relations

with the large-scale SSS variability and make realistic predictions. We use the three models introduced in Section 3.2.2 to predict large-scale SSS variability ( $>100$  km) and to check if the model performance is consistent with our current knowledge. The prediction and associated errors are shown in Figure 3.5.

We expect that by employing the correlation between seafloor roughness and SSS variability, we will not be able to make good predictions since the MDT gradient is not correlated with seafloor roughness. This expectation is borne out in Figure 3.5a, which captures almost no large-scale SSS variability. The prediction has an  $R^2$  score of 0.010 and an MSE of  $0.208 \mu\text{rad}^2$ .

The linear model uses MDT gradient as one of the 27 input variables. Overall, it captures the variations of geostrophic flows relatively well and shows strong variability in the vicinity of strong geostrophic flow. The predicted SSS variability (Figure 3.5c) is somewhat biased: it is larger than observations over regions where the SSS is larger and smaller in background regions where SSS is small. This model has an  $R^2$  score of 0.667 and an MSE of  $0.070 \mu\text{rad}^2$ .

The boosted trees model makes the best predictions for the large-scale SSS variability ( $>100$  km). It makes realistic predictions (Figure 3.5e), and the prediction error (Figure 3.5f) is reduced and less biased, compared to the linear regression model (Figure 3.5d). This model has a  $R^2$  score of 0.776 and an MSE of  $0.047 \mu\text{rad}^2$ .





mesoscale SSS variability (30-100 km) in Figure 3.6. Features with smaller ranks have higher importance.

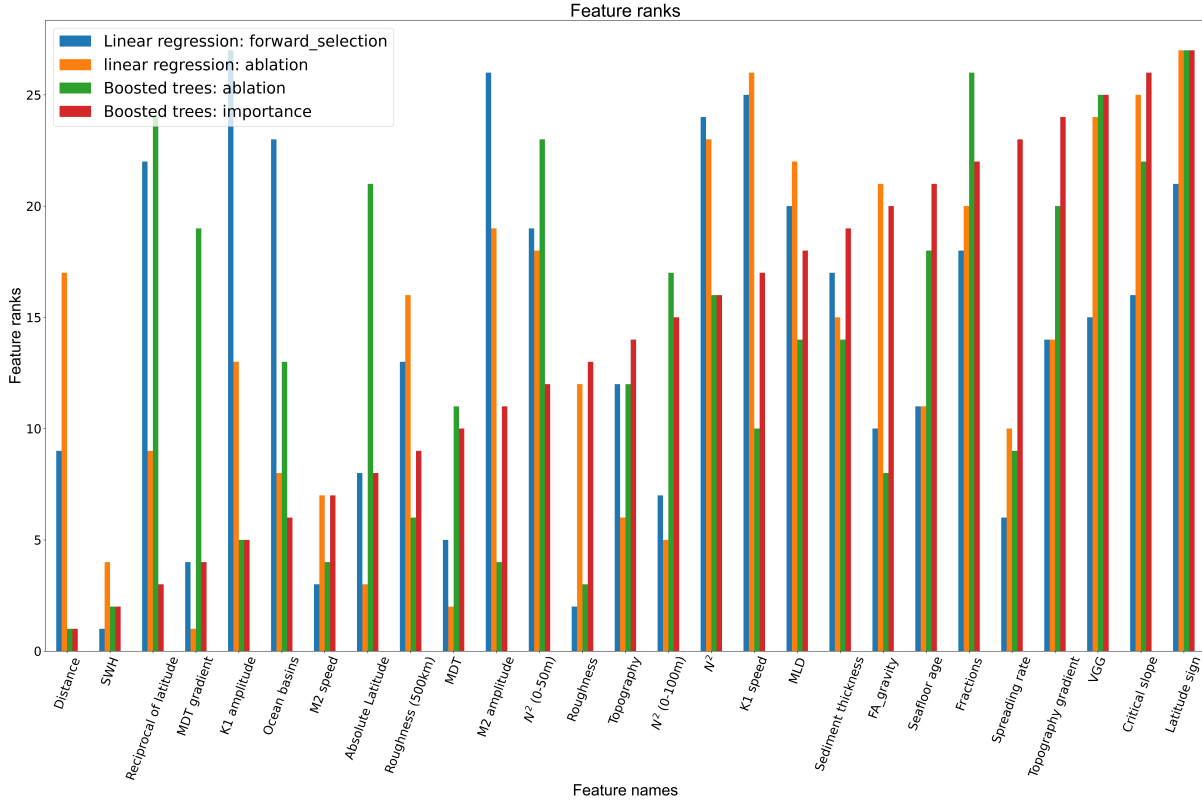


**Figure 3.6.** Ranks of features of the mesoscale SSS variability (30-100 km) from the linear regression model using the forward selection and the feature ablation; from the boosted trees model using the feature ablation and the feature importance returned by the model. Features with smaller ranks have higher importance. Features and their full name are introduced in Section 3.2.1.

These four methods provide different ranks of feature importance. At least two out of four show that distance to the nearest thermocline boundary, SWH, MDT, MDT gradient, absolute latitude, seafloor roughness, ocean basins and  $M_2$  tidal speed,  $K_1$  tidal amplitude, and  $N^2(0-100m)$  are the governing features in predicting the mesoscale SSS variability. The boosted trees ablation methods show that the model performance would decrease the most when removing SWH as a feature (L2 norm increases by 35.6%). The sign of latitude, the critical slope of the  $M_2$  tide, VGG, topography gradient, and fractions of slope above critical, are not

important in any of the four methods. While SSS variability is relevant to ocean basins, it is not hemispherically related. Note that the lack of correlation with VGG is an indication that the mean SSS model removed from the profiles accurately captures the small-scale gravity features that are represented by VGG. The remaining SSS variability, which is used as a label in this study, represents oceanic signals, a main assumption of the entire analysis.

At large scales ( $>100$  km), feature rankings in Figure 3.7 indicate that all methods show MDT gradient to be the most dominant feature in predicting SSS variability, in accord with our initial expectation. Large-scale SSS variability can be represented by the strength of the geostrophic flow, which scales with MDT gradient. Where the mean flow is large, the variation is large as well.

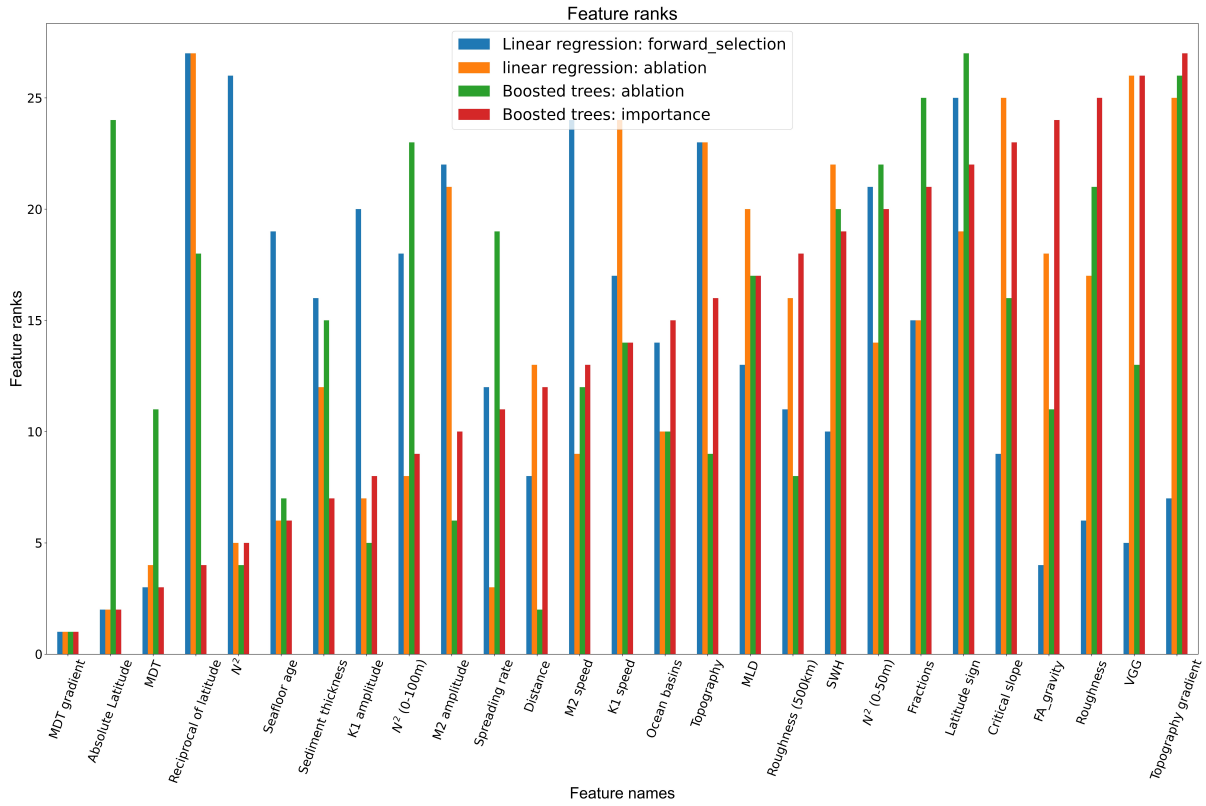


**Figure 3.7.** Same as Figure 3.6 but for ranks of features of the large-scale SSS variability ( $>100$  km).

### 3.4 Discussion and Conclusions

We have used three statistical methods to build models and predict the SSS variability in the mesoscale band (30-100 km) and in the large-scale band ( $>100$  km). We have revisited the correlation analysis of Gille et al. (2000) and then extended our analysis to incorporate more environmental parameters and to test additional methods to understand the governing factors of sea surface variability. Both the linear regression model and the boosted trees model incorporate 27 features, and they significantly outperform the correlation analysis that only accounts for the seafloor roughness and ocean depth. The boosted trees model also has advantages over the linear regression model in that it is capable of building more complicated non-linear relations between environmental parameters and the mesoscale SSS variability. Thus it has a higher  $R^2$  score (0.563 compared to 0.381) and results in a smaller MSE in prediction errors ( $0.007 \mu\text{rad}^2$  compared to  $0.010 \mu\text{rad}^2$ ) for the mesoscale SSS variability. The large-scale SSS variability is largely consistent with geostrophy, with both the linear regression and the boosted trees model able to explain more than 60% of the variance, and MDT gradient serving as the leading order predictor.

We divide data into 64 geographical blocks and use data from separate blocks to train models and make predictions. This approach is essential for the boosted trees model because it prevents the model from simply using local information to make unrealistically good predictions. Although this approach is unnecessary for the linear regression model, for consistency, we use it for both the boosted trees model and the linear regression model to train the models, make predictions, and evaluate model performance. For each test block, we train the model 30 times as introduced in Section 3.2.2. The prediction map concatenated from 30-realization average greatly reduces the discontinuities at block edges and has little impact on evaluating model performance. The variance of 30-realization of predictions is a measure of model uncertainty. We calculate the standard deviation (std) and use  $1/\text{std}$  as weights to recalculate the  $R^2$  score. The updated

$R^2$  scores using  $1/\text{std}$  as weights are 0.407 for the linear regression model, and 0.583 for the boosted trees model, which are similar to  $R^2$  scores assuming uniform weights (0.381 for the linear regression model and 0.563 for the boosted trees model).

Although the machine learning models in this study predict SSS variability, our fundamental goal is to use machine learning to identify the physical processes governing SSS variability. There are two categories of conclusions that we can reach from this study: (1) what environmental parameters matter in predicting SSS variability? (2) in which regions of the ocean do our models fall short, and why? We hypothesize that processes or regions that are not readily represented by a simple model might indicate the presence of unusual or complicated physical mechanisms.

We have used four methods to rank the importance of environmental parameters, that is to calculate the feature importance. Rankings from the four methods can diverge substantially, although the linear regression and the boosted trees model show some overlap. Overall, the rankings show that distance to the nearest thermocline boundary, SWH, MDT, MDT gradient, seafloor roughness, ocean basins and  $M_2$  tidal speed,  $K_1$  tidal amplitude, and  $N^2$  (0-100m) are key features in predicting the mesoscale SSS variability (30-100 km). For large scales ( $>100$  km), all methods show that MDT gradient is the dominant feature in predicting SSS variability.

The high feature importance assigned to the distance to the nearest thermocline boundary suggests that internal wave generation plays a role in generating SSS variability. This is because internal waves have the largest amplitudes at the base of the thermocline. They can be generated when tides disturb water to move up and down the steep seafloor boundary, so waves are larger close to the boundary and dissipate as they move away. Tidal wave beams interact with the thermocline and will generate large-amplitude solitary waves (Akylas et al., 2007).

The role of SWH in governing mesoscale SSS variability (30-100 km) could have two interpretations: first it could mean that wave height noise leaks into the 30-100 km wavelength band; alternatively, it could indicate that SWH reflects increased wind forcing, which produces more mesoscale ocean variability. We correlate the mean SWH with multiple band-pass filtered SSS variability and find that they are highly correlated (coefficients  $> 0.5$ ) when the SSS variability has a wavelength less than 30 km (Figure 3.9 in Section 3.6). The correlation coefficient drops below 0.5 where the SSS wavelength is longer than 30 km, which indicates SWH noise is not the dominant force anymore, but its influence cannot be ruled out.

There are straightforward relations between mesoscale SSS variability and MDT gradient, seafloor roughness, absolute latitude, ocean basins, stratification  $N^2$  (0-100m),  $M_2$  tidal speed and  $K_1$  tidal amplitude. MDT gradient represents the strength of geostrophic flows. The mesoscale eddies emerging from the instabilities of strong geostrophic flows could appear in smaller spatial scales. Thus, there is strong mesoscale SSS variability in the vicinity of western boundary currents and the ACC, and the MDT gradient is highly correlated with mesoscale SSS variability. As discussed by Gille et al. (2000), seafloor roughness could dissipate eddy kinetic energy in the deep ocean, or it could be a source of energy by generating internal waves or instabilities in the shallow ocean. Some ocean activities, e.g. ocean eddies, are tied to the latitude. The physical processes and the generation mechanisms are different in different dynamical zones or ocean basins. The  $M_2$  and  $K_1$  barotropic tides can convert to internal tides when they impinge on a steep seafloor in stratified water.

We have identified a number of regions where machine learning consistently fails to yield good predictions for the mesoscale SSS variability: (1) the Amazon outflow ( $310^\circ/325^\circ/0^\circ/15^\circ$ ) in the tropical Atlantic Ocean; (2) the Mascarene Ridge ( $45^\circ/63^\circ/-15^\circ/-3^\circ$ ) in the Indian Ocean; (3) the Kerguelen Plateau ( $75^\circ/95^\circ/-60^\circ/-45^\circ$ ) in the Southern Ocean. Each of these regions displays large negative prediction errors (red boxes in Figures 3.4b, 3.4d and 3.4f). The Amazon



outflow is associated with strong local and seasonal freshwater input. This freshwater input affects stratification, likely in ways that are not replicated elsewhere in the global stratification data that we use in the study. There is also a strong tidal impact that is not necessarily well captured. The Mascarene Ridge is located in an area of energetic barotropic tidal currents that are normal to the ridge (Lozovatsky et al., 2003; Morozov 2006). The ridge is characterized by guyots with flat summits straddled by channels. The shallow banks, the shallow channel between the banks, and deep waters around the Mascarene Ridge provide unique conditions for the generation of intense internal tides (Morozov, 2006). The Kerguelen Plateau is a major topographic feature in the Southern Ocean where the main fronts of the ACC encounter rough topography. The strong geostrophic flow converts to upward-propagating internal waves over rough bottom topography. Strong wind forcing generates near-initial downward-propagating internal waves (Meyer et al., 2015).

The difficulties that the boosted trees approach encounters in modeling these three regions, suggest that they are unusual areas relative to the training data sets, and in the language of machine learning can be considered to be “out of distribution” (Hendrycks and Gimpel, 2016) unless they are specifically included as training data. The  $R^2$  scores excluding the above three outlier regions are 0.407 and 0.579 for the linear regression and the boosted trees model, which are slightly better than  $R^2$  scores for the global ocean (0.381 and 0.563, respectively). The outlier regions have little impact on skewing model accuracy. The physical processes within these regions are possibly strongly governed by regionally specific environmental parameters that are not in our features. Local parameters like freshwater input are hard to incorporate, because they are concentrated near the coast and sparsely distributed in space. Our model has no temporal resolution, and some important environmental parameters, i.e., wind stress, are also not included. This is consistent with findings in other studies showing that machine learning algorithms are less likely to succeed when validation or test data do not lie within the distribution of the training data (Liang et al., 2017; Partee et al., 2022; Sonnewald et al., 2021; Sinha and Abernathey, 2021).

In these regions, a physical model that incorporates existing physical knowledge may have better predictive skills.

Other than the linear regression and the boosted trees model, we also tested the possibility of training with the lasso regularization, and the random forest models. The regularization parameter for the lasso model is too small to make it different from the linear regression. The performance of random forest proved to be worse than boosted trees, and thus we discarded its use as a non-linear model in this study. Deep learning or neural networks can also be a potential class of models to explore. We adopted the boosted trees model as our preferred nonlinear machine learning model because it is efficient, it converges well compared to random forests, and it provides enough flexibility to test multiple inputs and multiple scenarios efficiently.

Data quality goes a long way toward determining the performance of the machine learning model and the predictions. Machine learning algorithms are not able to train a good model by identifying all possible connections between poorly selected input features. To explore the importance of using physically relevant input features, we chose as features 27 pictures of animals that have no relation to the SSS variability, although the animal pictures do have large-scale patterns of spatial variability that are comparable to our environmental parameters. We used these pictures to train a linear regression model and a boosted trees model to predict SSS variability following the same procedures that we used with the environmental parameters (see Figure 3.10 in Section 3.6). Since the animal pictures have no physical relation to environmental parameters, we would expect a large MSE and an  $R^2$  of 0. Indeed, if we use 27 pictures of Gaussian noise as inputs, the MSE and  $R^2$  are  $0.025 \mu\text{rad}^2$  and  $-0.007$  for both models. However, counter to expectations, when we use animal pictures for the linear regression model the MSE and  $R^2$  are  $0.023 \mu\text{rad}^2$  and  $0.08$ , and for the boosted trees model they are  $0.018 \mu\text{rad}^2$  and  $0.273$ . Overall, with unphysical data, both models perform worse than they do when using environmental parameters. For the boosted trees model, the fact that irrelevant data with feature

scales comparable to observed spatial scales can explain 0.273 of the variance should serve as a cautionary warning that spatially correlated irrelevant fields can yield artificially high skill metrics.

The swath Surface Water and Ocean Topography (SWOT) mission to be launched in late 2022, will have the ability to resolve scales of a few tens of kilometers where internal tides/waves are mixed with geostrophic currents (Morrow et al., 2019). SWOT's spatial resolution capabilities call for understanding unbalanced waves and mesoscale ocean activities. Our study shows both the potential and limitations of using machine learning to unveil the driving forces and to make global predictions of mesoscale SSS variability. Machine learning is a powerful tool, and this study is a step forward in using machine learning to advance our understanding of Earth system science.

### **3.5 Acknowledgements**

This work was supported by the NASA SWOT program (NNX16AH64G, NNX16AH67G and 80NSSC20K1136), the NASA Ocean Surface Topography Science Team (NNX17AH53G and 80NSSC21K1822) and the Office of Naval Research (N00014-17-1-2866). The Generic Mapping Tools (GMT, Wessel et al., 2013) were extensively used in data processing.

Links to the open accessible data are provided here:

SYNBATH:

<https://topex.ucsd.edu/pub/synbath/>

STRM15+:

[https://topex.ucsd.edu/pub/srtm15\\_plus/](https://topex.ucsd.edu/pub/srtm15_plus/)

VGG and free-air gravity:

[https://figshare.com/articles/online\\_resource/Tozer\\_et\\_al\\_2019\\_SRTM15\\_GMT\\_Grids/7979780](https://figshare.com/articles/online_resource/Tozer_et_al_2019_SRTM15_GMT_Grids/7979780)

Seafloor spreading rate and oceanic crustal age:

<https://earthbyte.org/webdav/ftp/earthbyte/agegrid/2020/>

mean dynamic topography:

[https://www.space.dtu.dk/english/Research/Scientific\\_data\\_and\\_models/downloaddata/](https://www.space.dtu.dk/english/Research/Scientific_data_and_models/downloaddata/)

Salinity and temperature data:

<https://www.ncei.noaa.gov/access/world-ocean-atlas-2018/>

Mixed-layer depth:

<http://mixedlayer.ucsd.edu>

Sediment thickness:

<http://earthdynamics.org/data>

All other data including the sea surface slope variability and processed features are available upon requesting the corresponding author.

### 3.6 Appendix

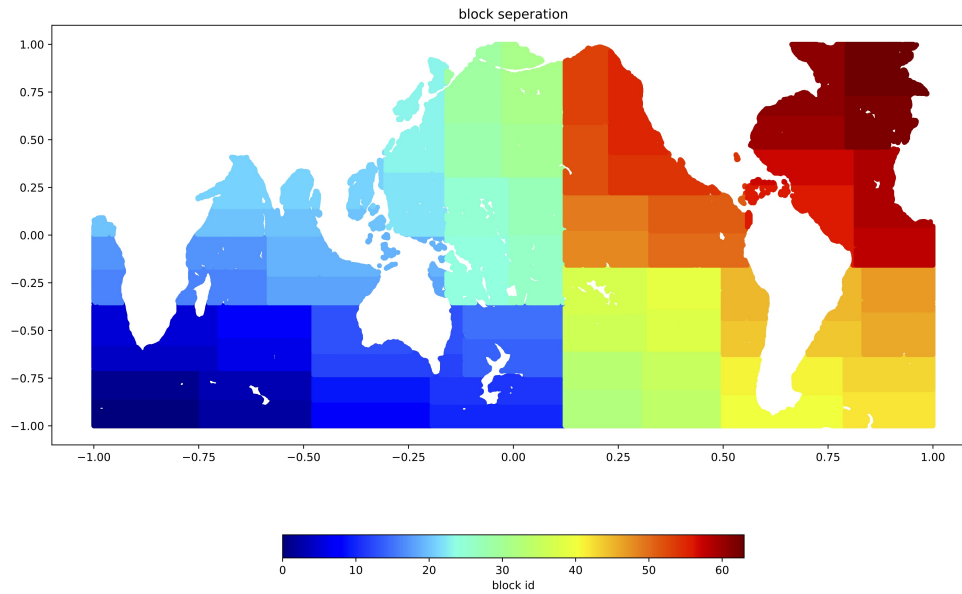


**Figure 3.8.** Equal-area block separation. Each block is assigned with a unique ID from 0 to 63. The longitude ( $0^{\circ}$  to  $360^{\circ}$ ) and latitude ( $-60^{\circ}$  to  $60^{\circ}$ ) are linearly normalized to -1 and 1.

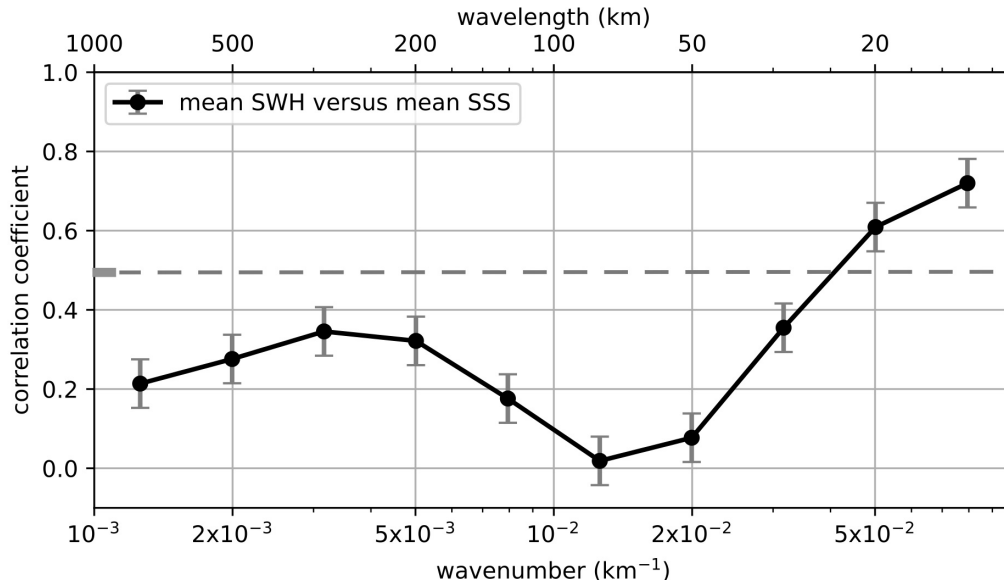


**Figure 3.9.** The Pearson correlation coefficient for the mean significant wave height and the SSS variability in multiple sub-bands (10-15 km, 15-25 km, 25-39 km, 39-63 km, 63-100 km, 100-158 km, 158-251 km, 251-398 km, 398-630 km, 630-1000 km). A coefficient of  $\pm 0.5$  means strong correlation.

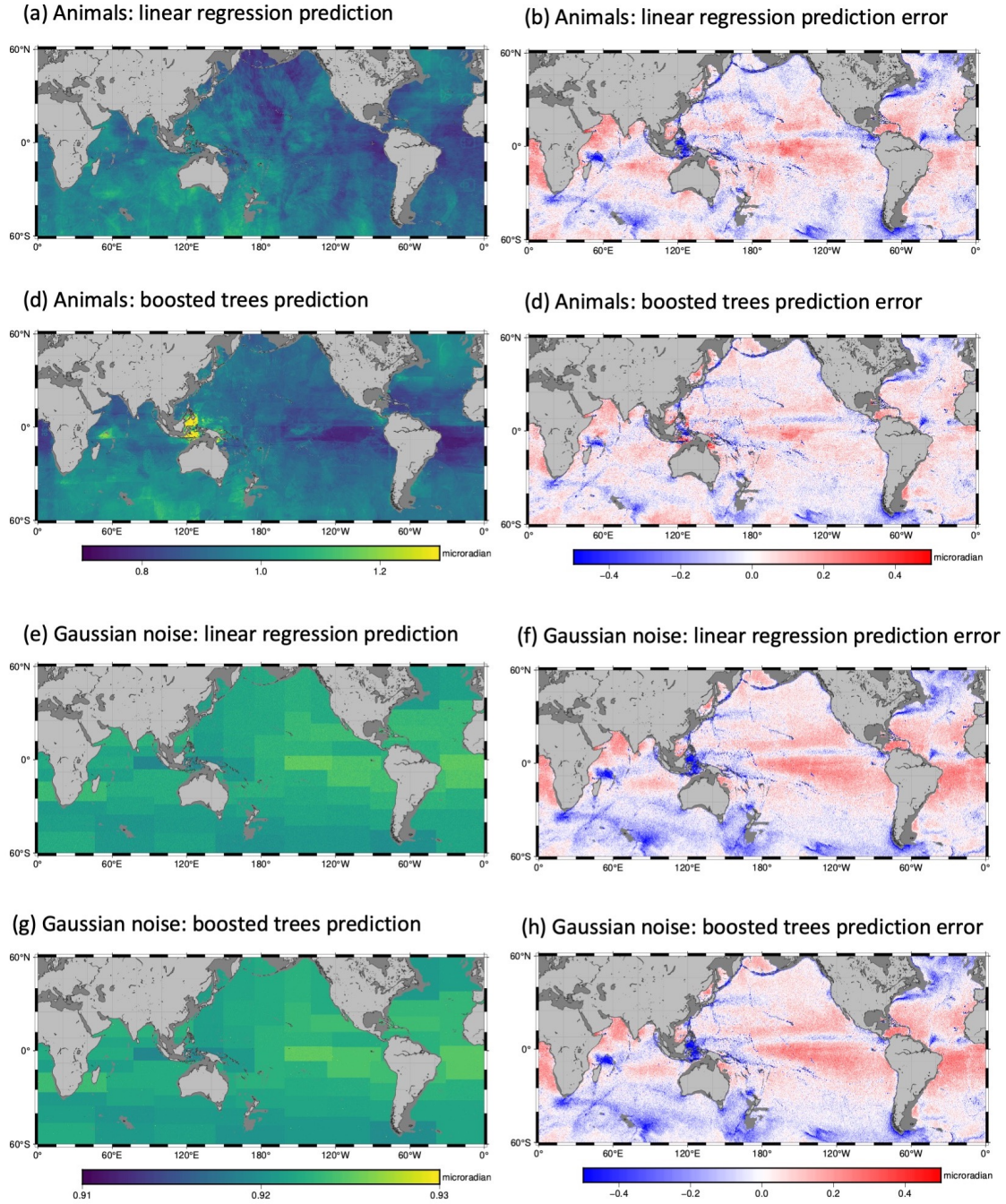


**Figure 3.10.** (a) The predicted SSS variability map (30-100km) and (b) the associated prediction error using the linear regression model with 27 features of random animals. (c) and (d) are the same as (a) and (b) except for using the boosted trees model. The MSE and  $R^2$  for the linear regression model are  $0.023 \mu\text{rad}^2$  and  $0.080$ , for the boosted trees model are  $0.018 \mu\text{rad}^2$  and  $0.273$ . (e) The predicted SSS variability map (30-100km) and (f) the associated prediction error using the linear regression model with 27 features of random gaussian noise. (g) and (h) are the same as (e) and (f) except for using the boosted trees model. The MSE and  $R^2$  for both models are  $0.025 \mu\text{rad}^2$  and  $-0.007$ .

## Chapter 4

# Seasonality of the Sub-Mesoscale to Mesoscale Sea Surface Variability from Multiple Satellite Altimetry

Sea surface slope (SSS) varies in response to a range of physical processes: tides, geostrophic flows, surface and internal waves, etc. We present the sea surface variation in the form of the SSS variability using 30 years of heterogeneous satellite altimetry measurements. We apply band-pass filters to the along-track SSS, and derive the mean and seasonal (annual and semi-annual) components of SSS variability in multiple wavelength sub-bands from 10 to 1000 km. We show that the seasonal components are generally small ( $\sim 10\%$  in amplitude) compared to the mean variability. Through correlation analysis, we show evidence that SSS variability with wavelengths less than 30 km is dominated by wave height noise. At sub-mesoscale to mesoscale (30-100 km) wavelengths, we identify high variability over western boundary currents and regions of rough topography. In this band, the high-latitude Northern Hemisphere and the south Indian Ocean are associated with large annual cycles. The variability is higher in local wintertime except for a few regions, for example the Bay of Bengal, which shows high variability in the boreal spring and fall. Through power spectral density analysis of the seasonal SSS variability, we find that the energy differences between local winter and summer are stronger at smaller scales ( $< 100$  km). The Ka-band radar interferometry instrument on the Surface Water and Ocean Topography (SWOT) satellite mission will allow observation of ocean surface activities down to



$\sim 20$  km at submonthly time scales, but wave-related errors (sea state bias, aliasing, wind-driven activities, etc.) will still be a major challenge.

## 4.1 Introduction

Satellite altimetry has revolutionized our understanding of upper-ocean circulation dynamics and sea level change. However, we still have limited understanding of sub-mesoscale to mesoscale ocean activity, defined here as variability in the 30-100 km wavelength band. This band is less well observed and less understood compared to the geostrophic band. Motions in this band have smaller scales than the  $O(100$  km) resolution (Ballarotta et al., 2019) of the most commonly used gridded sea surface height (SSH) product, distributed by the Copernicus Marine Environment Monitoring Service (CMEMS). The spatial resolution of the CMEMS product are restricted by measurement noise and the wide separation between nadir tracks for satellite altimeters. SSH in the 30-100 km band is associated with strong eddy kinetic energy and plays an important role in the dynamics of ocean energy transfer and mixing (Ferrari and Wunsch, 2009). It contains both unbalanced wave motions (internal tides/waves, near-inertial flows) and balanced geostrophic flows. In the 30-100 km band, there are pronounced seasonal sea surface height variations, which are about 10% of the mean variability in amplitude (Chen and Qiu, 2021). The average variability of SSH is related primarily to the mean dynamic topography, significant wave height (SWH), lunar semi-diurnal ( $M_2$ ) tides, thermocline depth, and seafloor roughness (Yu et al., 2022). Among those factors, the SWH and thermocline depth have strong seasonality. Previous studies have proposed that the seasonal variability stems from (i) changes in inertia-gravity waves from the seasonally changing upper-ocean stratification (Rocha et al., 2016); or (ii) changes in eddy kinetic energy from seasonally varying mixed-layer instability (Qiu et al., 2014; Callies et al., 2016; Uchida et al., 2017). These seasonality studies have the limitations of being either regional or based on model output. Our study takes a global

approach, based on satellite data, using the SSS from along-track altimetry to study seasonal ocean variability and to investigate the influence from surface waves and thermocline depth change. With more than 30 years of high-quality, repeat and non-repeat satellite altimetry data collected, the dense ground track coverage and diverse track orientations allow us to create sea surface slope (SSS) variability maps with  $\sim 10$  km spatial sampling and to investigate mean, annual and semi-annual variability.

The major objective of this work is to estimate the seasonal variations (the annual and semi-annual components) of SSS variability with wavelengths from 30 km to 100 km and to study the seasonal spectral characteristics of SSS variability. We try to understand the influence of the SWH and the thermocline depth on the SSS variability. We compute the SSS variability using the block median value of the absolute SSS anomaly from multiple altimeter profiles, referenced to the mean sea surface slope. Compared to SSH, along-track slopes amplify high-wavenumber signals and “whiten” the power spectral density (PSD) by  $k^2$ , because slope is the spatial derivative of SSH. The kinetic energy tends to fall off like  $k^{-2}$  in the submesoscale range (Callies and Wu, 2019), which results in a near white PSD of SSS in the 30-100 km wavelength range. We divide the SSS variability into multiple sub-bands to investigate the seasonal spectral characteristics.

As discussed by Chen and Qiu (2021), altimeter SSH data have a white noise floor. This noise floor intersects the red-spectrum of the ocean SSH variability at wavelengths somewhat greater than 30 km. Chen and Qiu (2021) use along-track altimetry data to study the SSH in the 30-120 km band after subtracting a white noise floor for the Jason and SARAL/ALtiKa (Satellite with ARgos and ALtiKa) data (Xu and Fu, 2012). Similarly, to study the wavenumber spectra from recent missions, (Vergara et al., 2019) remove a white noise floor from Jason-2 and SARAL/ALtiKa and a red noise floor from Sentinel-3. However, extrapolating the high-frequency noise floor back to lower frequencies could provide the wrong value of SSH if the

white noise assumption is not valid. Moreover, it could introduce a false seasonal variation if the noise floor is linked to SWH (Lawrence and Callies, 2022), which has a large seasonal component. A major focus of our analysis is to reduce the noise by a factor  $> 1.6$  through two-pass waveform retracking (García-García and Ummenhofer, 2015; Zhang and Sandwell, 2017) and careful editing. This enables us to retain shorter wavelengths in the ocean variability analysis and hopefully reduce the seasonal contamination.

The SSS variability map constructed in this study has a spatial sampling of about 10 km, and we show through correlation analysis that SSS variability is highly correlated with wave height noise at wavelengths less than 30 km (Pearson coefficient  $> 0.5$ ) and that the correlation is close to zero at 50-km wavelength. Thus we adopt 30 km as the shortest wavelength used in the seasonality analysis. Nevertheless there is still some correlation between SSS and SWH in the 30–50 km band. This could have two causes: (1) residual wave height noise leaks into SSS variability or (2) surface gravity waves are wind-driven, and part of the SSS variability is also wind-generated, thus leading to a strong correlation without a direct mechanistic connection between surface waves and SSS variability. We use the surface wind stress data from the version 2 Cross-Calibrated Multi-Platform (CCMP2) to help understand the impact of waves from the above two sources. A definitive understanding of the correlation between SSS and SWH will be provided by the Surface Water and Ocean Topography (SWOT) altimeter mission which will have dramatically lower SWH contamination (Fu and Ubelmann, 2014).

This paper is structured as follows: in the next section, we describe the data sets used in the study, including the SSS from satellite altimetry, high-resolution model output (Rocha et al., 2016), the SWH, the surface wind speed (WSP), and the thermocline depth. We show that SWH contaminates the shortest wavelengths ( $< 30$  km) of SSS variability. In the result section, we present the mean, annual, and semi-annual components of SSS variability in the sub-mesoscale to mesoscale bands (30–100 km). We also show the seasonal power spectra of

SSS and investigate the influence of SWH and thermocline depth on the SSS variability. In Section 4.4 we discuss the details of the spatial and temporal variations in SSS variability, and investigate the latitude variations in terms of solar forcing and oceanographic processes.

## **4.2 Datasets**

### **4.2.1 Sea Surface Slope from Altimetry**

We use the along-track profiles from Envisat, Cryosat-2, Jason 1/2, SARAL/ALtiKa and Sentinel-3A/B collected from 2001 to 2022. The altimeter data have two modes. The older altimeters operate in the standard low-resolution mode (LRM), where the radar footprint is circular and several km in diameter depending on SWH. Cryosat-2 and Sentinel-3 can operate in the synthetic aperture radar (SAR) mode, where the along-track footprint is reduced to  $\sim 250$  m through synthetic aperture analysis. The noise level of the Sentinel-3 SAR altimeter is 1–2 times lower than other LRM altimeters (Ranndal et al., 2020). However, as shown in previous studies ((Garcia et al., 2014), 2014; Zhang and Sandwell, 2017), the noise floor of all the LRM altimeters can be reduced by a factor of 1.5–1.7 through two-step retracking to match the precision of SAR data. Moreover these studies provide a spectral comparison between the standard 3-parameter retracking (CMEMS) and the two-step retracking. The two-step retracking method provides the largest noise reduction in the 10–45 km wavelength band which is the band of the spectral hump (Dibarboure et al., 2014). Note that the noise floor of the SARAL/ALtiKa data is nearly 2 times lower than the best SAR data from Sentinel-3 (Zhang and Sandwell, 2017). This retracking combined with careful editing, discussed next, is essential for resolving 30 km ocean variability without having to shape the spectra of the LRM data as was needed in the Chen and Qiu (2021) analysis. We push the limits to 30 km by applying a two-step waveform retracking, which makes the radar data match the precision of SAR data.

After retracking the raw waveforms, we re-estimate, and correct, sea state bias by removing 8%–10% (dependent on satellites) of SWH in the range measurements. There are two steps to edit outliers, which further improve the spatial resolution of the profiles. First, we edit 20-Hz waveform data using flags supplied with the level-1 product. In addition, waveforms having a large misfit from the Brown model and large SWH ( $>10$  m) are excluded. These 20-Hz data are low-pass filtered using a Parks-McClellan filter with a half gain at 6.7 km wavelength and down-sampled to 5 Hz. Standard geophysical corrections are applied, including wet and dry troposphere delay, inverse barometer effect, and solid Earth and barotropic ocean tides (FES2014, Carrère et al., 2016). The corresponding slopes from geophysical corrections are small ( $<1$   $\mu$ rad) except for the barotropic ocean tide at coastal areas (Zhang et al., 2018), which are excluded in this study. Second, the 5 Hz along-track slopes are compared with the best mean SSS model (Sandwell et al., 2019), and outliers more than 3 standard deviations (typically  $>30$   $\mu$ rad) are removed. These data are further low-pass filtered with a second Parks-McClellan derivative filter with a half gain at 8.3 km wavelength to form along-track SSS. We apply local slope geoid corrections (Sandwell et al., 2014) and remove the mean SSS to obtain SSS anomaly profiles that reflect oceanic variability, wave height noise, and tide model error.

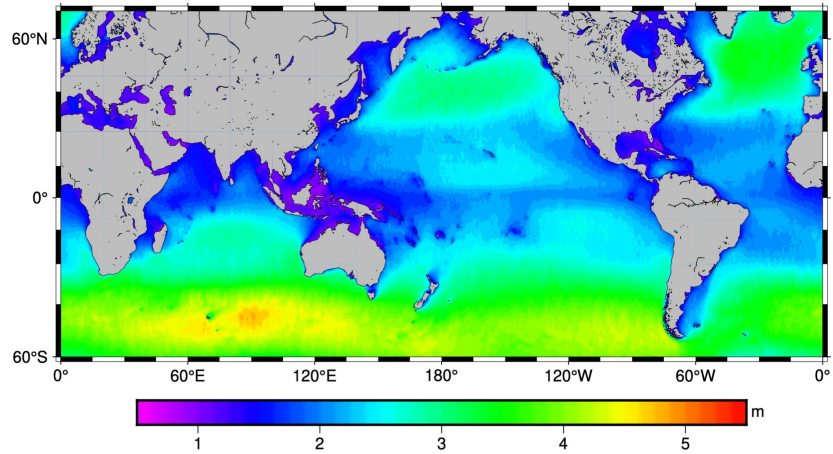
We are interested in the spectral characteristics and seasonality of the SSS variability. To allow for spectral analysis, we decompose the SSS variability into 10 sub-bands that are evenly spaced in the logscale wave-number domain (10.00–15.84 km, 15.84–25.12 km, 25.12–39.81 km, 39.81–63.09 km, 63.09–100.00 km, 100.00–158.48 km, 158.48–251.18 km, 251.18–398.10 km, 398.10–630.95 km, and 630.95–1000.00 km) using 1-D band-pass Gaussian filters applied to the along-track profiles. Ideally we should apply a 2-D filter to the surface slope anomalies, but only 1-D profiles are available, so our band-pass filters are sub-optimal. The results are further subdivided into 12 months for the temporal analysis assuming that the interannual variations are small. We then calculate the median of the absolute value of the filtered slope anomalies in 7 by 5 arc minute spatial bins, which represent SSS variability. These block median compilations are

weighted by a polynomial function of the SWH for each satellite mission. Finally the 7' by 5' median absolute deviations are smoothed spatially using a low-pass Gaussian filter having a half gain at 200 km wavelength to further suppress noise in the monthly maps. We generate a mask to exclude regions poleward of 66°N or 60°S, land, and shallow water areas with depths less than 100 m (because of the inaccuracy of tide models around coasts). We calculate the mean, annual, and semi-annual components of the monthly SSS variability in the 30–100 km wavelength band (which roughly combines three sub-bands that have similar spatial patterns: 25–39 km, 39–63 km, and 63–100 km), and screen out regions associated with large standard deviation ( $>0.4 \mu\text{rad}$ ) or large mean values ( $>0.4 \mu\text{rad}$ ), where seasonal variabilities are mostly from ice change. We update the mask and apply it to all monthly data sets in the following analysis.

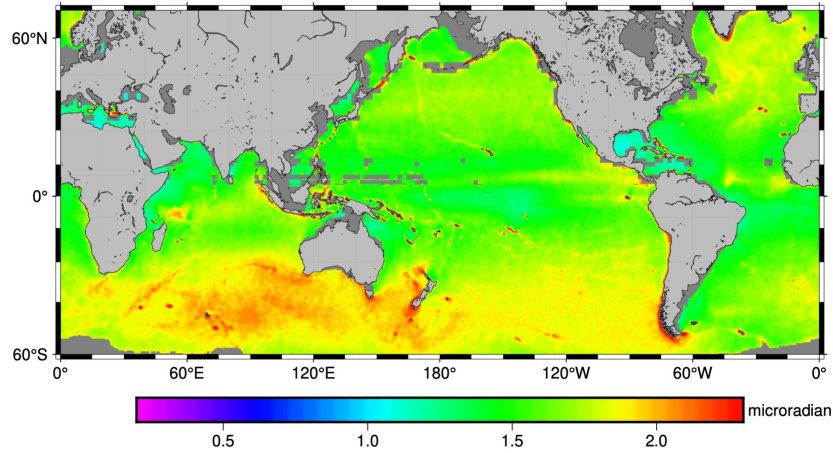
#### 4.2.2 Impacts from Wave Height Noise

As shown in previous studies (Zhang and Sandwell, 2017), noise from ocean surface gravity waves dominates the SSH and slope for wavelengths less than 20–50 km depending on the amplitude of the SWH as well as the retracking method used for the low-level processing. To assess this SWH contamination, we compile the SWH estimates from along-track profiles using block medians in 7' by 5' bins. These are further low-pass filtered at 200 km to reduce noise. The mean SWH map (Figure 4.1a) shows the expected features with typically large waves  $>4$  m in the Southern Ocean (latitudes:  $-60^\circ$  to  $-35^\circ$ ) and low wave height ( $<1.5$  m) in regions that are sheltered by islands from waves generated by high-latitude storms (such as the Southern California Bight or the Gulf of Mexico). We are concerned that the noise from waves will contaminate the small-spatial scale SSS variability (e.g., Figure 4.1b), and especially their seasonal variations. We have no independent way to assess this contamination so we perform a spatial correlation based on a linear regression between the band-pass filtered SSS and SWH, as shown in Figure 4.1c. The SWH is highly correlated (Pearson correlation coefficient  $>0.5$ ) with SSS variability for wavelengths shorter than about 30 km but poorly correlated at longer

wavelengths. The high correlation suggests that the SSS variability map is dominated by noise due to ocean waves, and we exclude wavelengths less than 30 km. The same high correlation between SSS and SWH has been noted in studies where gravity anomaly has been derived from multi-mission altimetry data (Zhang et al., 2017). Those studies typically low-pass filter the SSS data at 14–18 km to reduce SWH noise while still retaining the relatively large gravity signals ( $\sim 1.0 \mu\text{rad}$ ). The expected oceanographic signals are much smaller ( $\sim 0.1 \mu\text{rad}$ ) than the gravity signals so the SWH contamination will extend to longer wavelengths, and more filtering is needed.



(b) mean SSS variability (10-15 km)



(c) Correlation

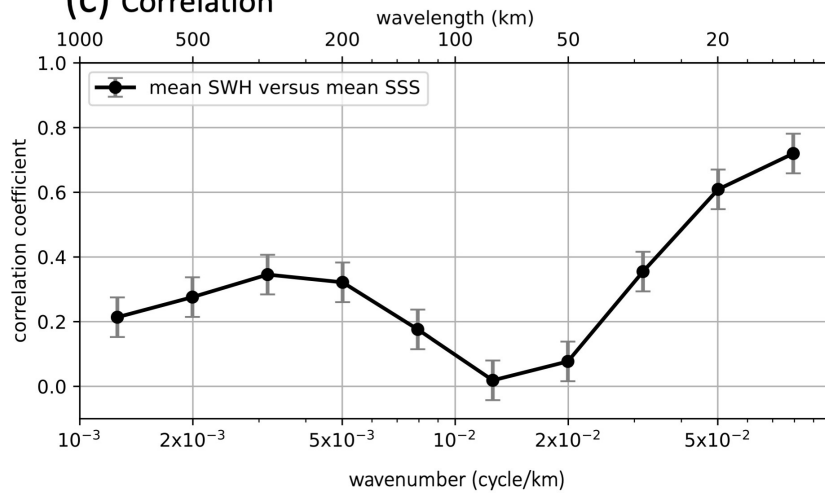


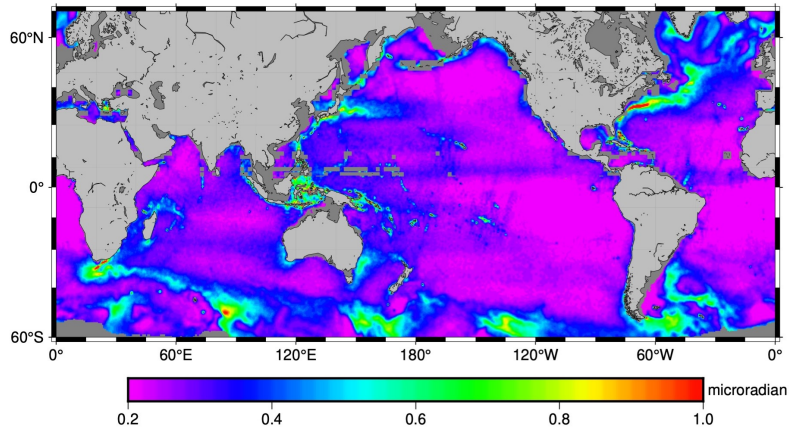
**Figure 4.1.** (a) Long-term average significant wave height (SWH) is large in the Southern Ocean and high-latitude Northern Hemisphere. (b) SSS variability in the 10-15 km wavelength band shows similar patterns as (a), yet with more detailed patterns. (c) Correlation between average SWH and band-pass filtered SSS variability. Correlation is higher than 0.5 at wavelengths shorter than 30 km. Error bars indicate the 99% confidence interval.



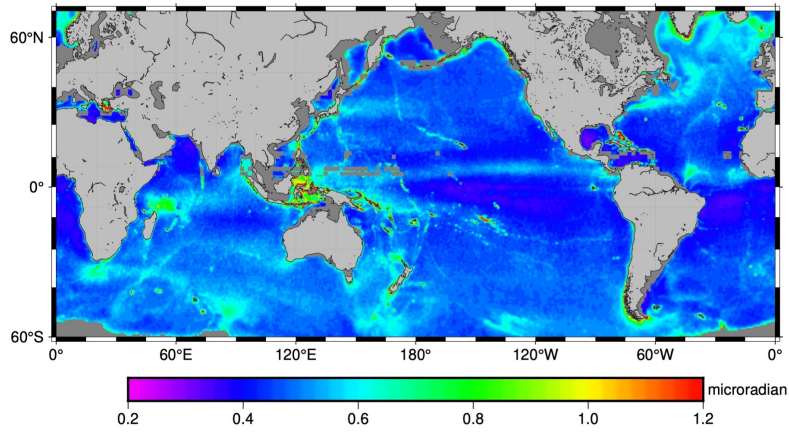
Mean slope variability in all the sub-bands is shown in the Appendix (Figure 4.8). Here we focus on two of the sub-bands at 100–158 km and 39–63 km wavelengths (Figure 4.2). The longer wavelength band (100–158 km, Figure 4.2a) shows all the usual features of mesoscale variability (Fu et al., 2010; Pascual et al., 2006) such as the western boundary currents, the Antarctic Circumpolar Current, and low variability in the centers of the gyres. The units of slope are in  $\mu\text{rads}$  ( $10^{-6}$ ), where 1  $\mu\text{rad}$  of slope corresponds to 63 mm of height change over a 1/2 wavelength of 63 km in horizontal distance, at the center of the 100–158 km wavelength band. In this band, the smallest resolvable variation is about 0.1  $\mu\text{rad}$ , which corresponds to the slope of a 1 cm/s geostrophic flow in the midlatitude with a typical value of Coriolis parameter of  $10^{-4}$  rad/s.

Many of the features seen in the shorter wavelength sub-band are new (39–63 km, Figure 4.2b). As expected there is high variability over eddy-intensified western boundary currents where large-scale fronts generate sub-mesoscale variance. In addition, there is high variability associated with prominent topographic features (locations labeled in Figure 2c) such as: fracture zones (Eltanin Fracture Zone, Diamantina Fracture Zone); trenches (Aleutian Trench, Mariana Trench, Tonga Trench), spreading ridges (mid-Atlantic Ridge, Pacific-Antarctic Ridge, Southwest Indian Ridge); seamount chains (Hawaiian-Emperor seamount chain, Salas y Gómez Ridge); and continental margins (Amazon Outflow, and Mascarene plateau). While this band shows certain similarities to the  $M_2$  internal tide signatures from model output (Arbic et al., 2012), there are differences over mid-ocean ridges as well as with the intensity of internal tides. This relatively narrow band captures only part of the unbalanced wave motions from satellite altimetry observations. We also notice the strong variability in the Inter Tropical Convergence Zone (ITCZ) and the North Equatorial Countercurrents.

(a) SSS variability (100-158 km)



(b) SSS variability (39-63 km)



(c) Bathymetry

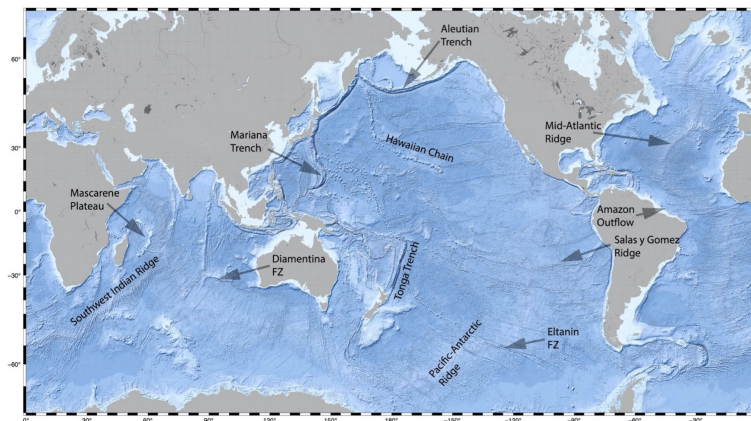


**Figure 4.2.** (a) SSS variability in the 100-158 km wavelength band shows high variability associated with western boundary currents and the Antarctic Circumpolar current. (b) SSS variability in the 39-63 km wavelength band shows high variability over mid-ocean ridges, large seamounts chains, trenches and the Amazon shelf. Regions masked out are in gray. (c) Locations of prominent bathymetric features mentioned in text. Land is in gray and blue shading illuminates ocean topography.

### 4.2.3 Sea Surface Slope from llc4320

We use the Estimating the Circulation and Climate of the Ocean (ECCO) Project's  $1/48^\circ$  MIT general circulation model with Latitude-Longitude-polar-Cap grid layout (aka llc4320, Rocha et al., 2016; Torres et al., 2018). The model is forced by 6-hourly ERA-Interim atmospheric reanalysis (Menemenlis et al., 2008) and 16 tidal components. The model has a  $1/48^\circ$  horizontal resolution and 90 vertical levels. We use the simulated SSH anomaly, which is referenced to the equipotential field and is noise free. We take the north-south spatial derivative of the SSH anomaly to construct the SSS anomaly, which can be directly compared with our processed SSS anomaly from satellite altimetry. We apply a 2-D bandpass filter to the hourly llc4320 SSS anomaly maps. This filter resembles the 30–100 km 1-D filter applied to the altimetry along-track SSS. We use data simulated from October 2011 to September 2012 and divide the hourly SSS data into 12 months. For each month of data, we use the median value of the absolute slope anomaly in each  $7'$  by  $5'$  grid to represent the slope variability. We further apply a 200 km wavelength Gaussian low-pass filter in space and obtain the monthly SSS variability maps in the 30–100 km band from llc4320 output.

### 4.2.4 Surface Wind Speed

We adopt the CCMP2 gridded surface vector winds analysis product (Atlas et al., 2011) to create monthly WSP maps. CCMP2 is produced using satellites, moored buoys, and model wind data. We use the monthly averaged WSP provided over a  $0.25^\circ$  by  $0.25^\circ$  grid, collected from 1990 to 2018, to calculate the multi-year mean monthly WSP then downsample to  $7'$  by  $5'$  grids. We apply a 200 km low-pass Gaussian filter in space and apply the geographical mask to obtain monthly WSP maps that will be used in Section 4.3.5 in this study.

### 4.2.5 Thermocline Depth

We use a climatology of monthly maximum mixed-layer depth (Holte et al., 2017) to construct the thermocline depth maps. The original data are monthly averages over the entire Argo record up to April 2022 on  $1^\circ$  bins, presenting an annual cycle of monthly mixed-layer properties. We apply a 200 km low-pass Gaussian filter to the maximum mixed-layer depth in space, sample the data to  $7'$  by  $5'$  grids, and apply the geographical mask to make the monthly thermocline depths. It has the same sampling and coverage as other data sets used in this paper.

## 4.3 Results

### 4.3.1 Seasonality: Annual Variability

For each  $7'$  by  $5'$  cell, we perform a point-wise least-square fit to a 5-parameter model consisting of the mean, and the sine and cosine components of the annual and semi-annual terms. We derive the amplitudes and phases, which are the months when the local periodicities reach their maxima, of the SSS variability in the 30–100 km range. We also derive the annual cycles for the SWH and the thermocline depth. At locations where amplitudes are small, the corresponding phases are not well defined.

In Figures 4.3a and 4.3b, we show the annual cycles of the SSS variability from satellite altimetry in the 30–100 km wavelength band. Here  $0.1 \mu\text{rad}$  in SSS variability corresponds to 5 mm in SSH variation over a 50 km half wavelength. The annual cycle amplitude (Figure 4.3a) is large in the high-latitude Northern Hemisphere and the southern Indian Ocean, and their maxima are reached in local winter months (December–January in the Northern Hemisphere, June–July in the Southern Hemisphere; Figure 4.3b). This indicates that winter storms might be the major driving force of the SSS seasonal variability. A few regions deviate from this hemispheric-scale seasonal pattern, for example, the Philippine Sea, the Arabian Sea, the Bay of

Bengal, the Mascarene Ridge, and the Northeastern Australian coasts. These regions might be driven by other strong forces that differ from the global ocean. Our altimetry annual variability (Figures 4.3a and 4.3b) resembles the annual SSH variability (30–120 km) in Chen and Qiu (2021) (see their Figures 6a and 6e) using the Sentinel-3A along-track data set, where there is no noise floor removal. There are fewer similarities compared to the SARAL/ALtiKa and Jason results in Chen and Qiu (2021), where a white noise floor was subtracted from the power spectra of along-track data.

Figures 4.3c and 4.3d present the annual variability results from the llc4320 simulation data. Compared to satellite altimetry results, llc4320 shows clear signatures of individual eddies, mainly because only 1 year of simulated data is available, so long-lived eddies are visible. There are both agreements and mismatches between the annual cycles from satellite altimetry and from llc4320 (Figures 4.3a and 4.3c). For example, they both show high annual variability in regions of high geostrophic variability, in the north Atlantic Ocean and in the Southwest Indian Ridge (Figure 4.3a, vs. Figure 4.3c). The altimetry results show strong annual signals in the ITCZ and south Indian Ocean around 30°S (Figure 4.3a) where there are strong salinity changes, while these patterns are missing in the llc4320 annual cycle (Figure 4.3c). The discrepancies between satellite altimetry and llc4320 could be partially related to different sampling time spans as well as slightly different along-track directions. In llc4320, SSS is computed in the north-south direction, while satellite altimetry combines along-track slopes from multiple directions ranging from 66° to 88°. The fundamental reasons could be related to the lack of surface wave forcing and the weak constraints of large-scale features in the llc4320 simulation. The spatial patterns of the llc4320 SSS annual variability and phase (30–100 km) shown in Figures 4.3c and 4.3d are similar to spatial patterns of llc4320 SSH variability and phase (30–120 km wavelength band) found by Chen and Qiu (2021).

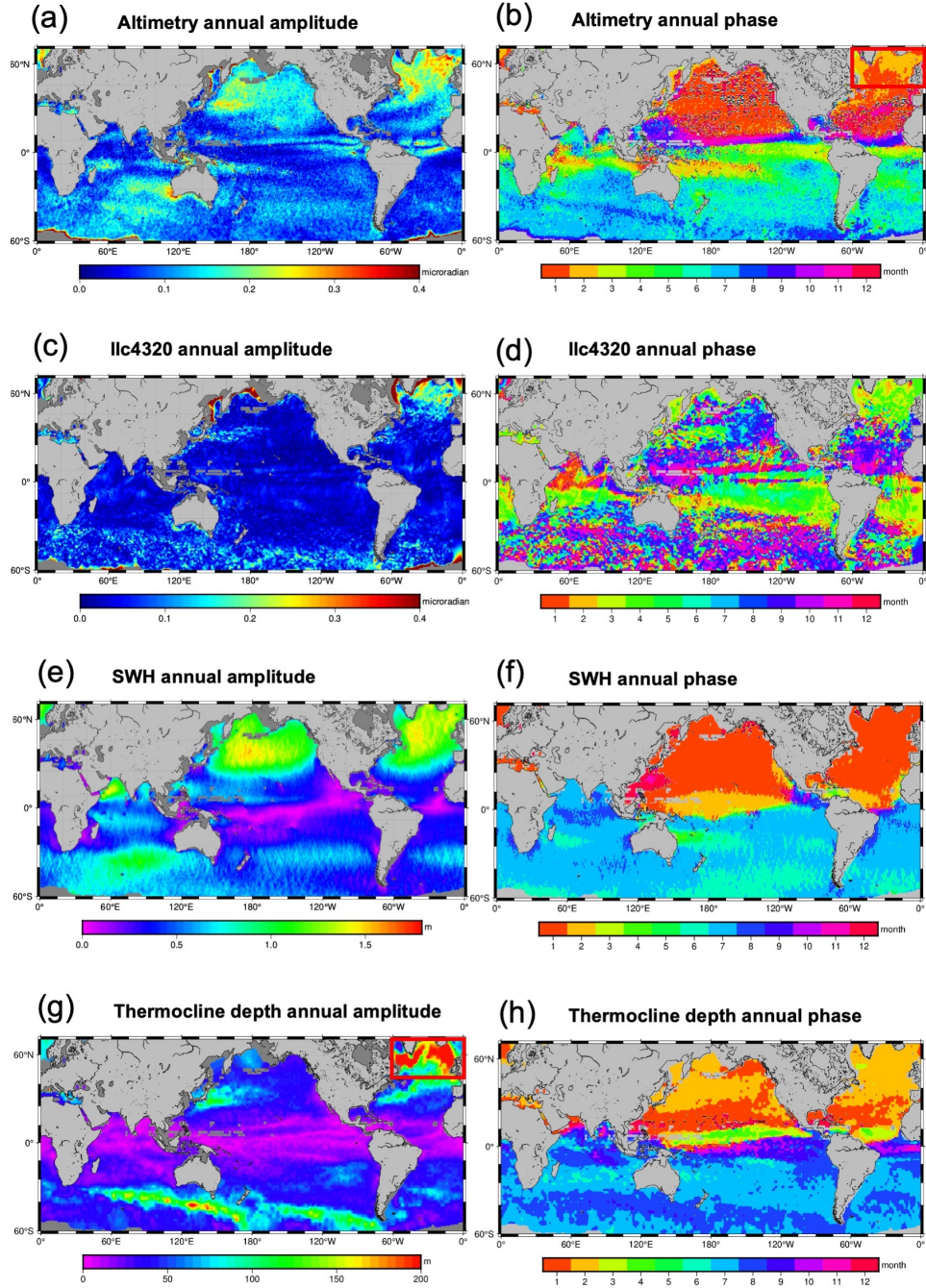


**Figure 4.3.** (a) Amplitude and (b) phase for annual SSS variability in the 30-100 km wavelength band from satellite altimetry. (c) and (d) are the same as (a) and (b) but from the Ilc4320 output. (e) and (f) for are the annual amplitude and phase for the SWH. (g) and (h) are the annual amplitude and phase for the thermocline depth. Streak patterns in (e) and (f) are artifacts of the altimeter sampling patterns. Regions masked out are in gray.



The annual amplitude of the SSS variability (30–100) from satellite altimetry (Figure 4.3a) is significantly correlated with both the annual amplitude of the SWH (Figure 4.3e) and the thermocline depth (Figure 4.3g), for example, strong amplitudes in the Kuroshio region, the north Atlantic Ocean, and the Southern Ocean. The annual phase of SSS variability (Figure 4.3b) is closer to the SWH (Figure 4.3f) than the thermocline depth (Figure 4.3g) except for a few regions where the thermocline depth has the largest annual changes, which implies a generally stronger link between SWH and SSS variability. Special attention should be given to the north Atlantic Ocean, where the annual amplitude of SWH is spatially uniform and reaches a maximum in January, while the thermocline annual change is significantly larger north of 50°N (red box in Figure 4.3g) than in mid-latitudes and peaks in February. The thermocline annual cycle maximum region (red box in Figure 4.3g) agrees well with the region where SSS variability reaches a maximum in February north of 50°N in the Atlantic Ocean (red box in Figure 4.3b). Our north Atlantic results support the hypothesis that under the same wave conditions (implying comparable wind forcing), a deeper thermocline promotes more sub-mesoscale SSS variability. Under this hypothesis, we expect to see that the time series of thermocline depth leads the sub-mesoscale SSS variability in time, probably on the order of a few weeks, in regions like the Atlantic Ocean north of 50°N. In contrast, within the ITCZ in the tropical Pacific and Atlantic Oceans, both the SWH and the thermocline depth show low annual variability, which disagrees with the high SSS variability.

### **4.3.2 Seasonality: Semi-Annual Variability**

We present the semi-annual cycle of the SSS variability (30–100 km) from satellite altimetry in Figures 4.4a and 4.4b. Semi-annual variations are mostly confined within  $\pm 15^\circ$  latitude (Figure 4.4a), and they are highly correlated with principal monsoon regions (Saha, 2009). We identify strong semi-annual variations in the Arabian Sea and the Bay of Bengal, and the driving forces could be related to the South Asian monsoon's semi-annual occurrence and

the salinity variability (Drushka et al., 2019).

In the Pacific and Indian Ocean tropics, the annual and semi-annual components of the SSS variability are strong and orthogonal in space. We show the annual/semi-annual amplitude and phase along a meridional profile zonally averaged over  $150^{\circ}\text{W}$ – $90^{\circ}\text{W}$  in Figures 4.4c and 4.4d. The annual cycle shows double peaks around  $4^{\circ}\text{N}$  and  $11^{\circ}\text{N}$ , with maxima in March or September. The semi-annual cycle peaks around  $7^{\circ}\text{N}$  in June and December. These results are consistent with a spatially oscillating pattern in SSS variability, centered around  $7^{\circ}\text{N}$  and migrating in the meridional direction at an annual period. It is highly correlated with the marine ITCZ, which undergoes a regular seasonal migration reaching its northernmost position during late boreal summer (August–September) and approaching the equator during boreal winter (February–March), passing the central latitude twice a year (Koutavas and Lynch-Stieglitz, 2004).

In contrast to the altimeter results, in the llc4320 model, the semi-annual amplitude resembles the annual amplitude, and the phase has no clear pattern. The annual and semi-annual cycles with poorly defined phases might be hard to differentiate given that only 1 year of data is available. We show the comparison of the mean SSS variability (30–100 km) from satellite altimetry and llc4320 (Figure 4.9) and show the semi-annual variations from llc4320 (Figure 4.10) in Appendix.



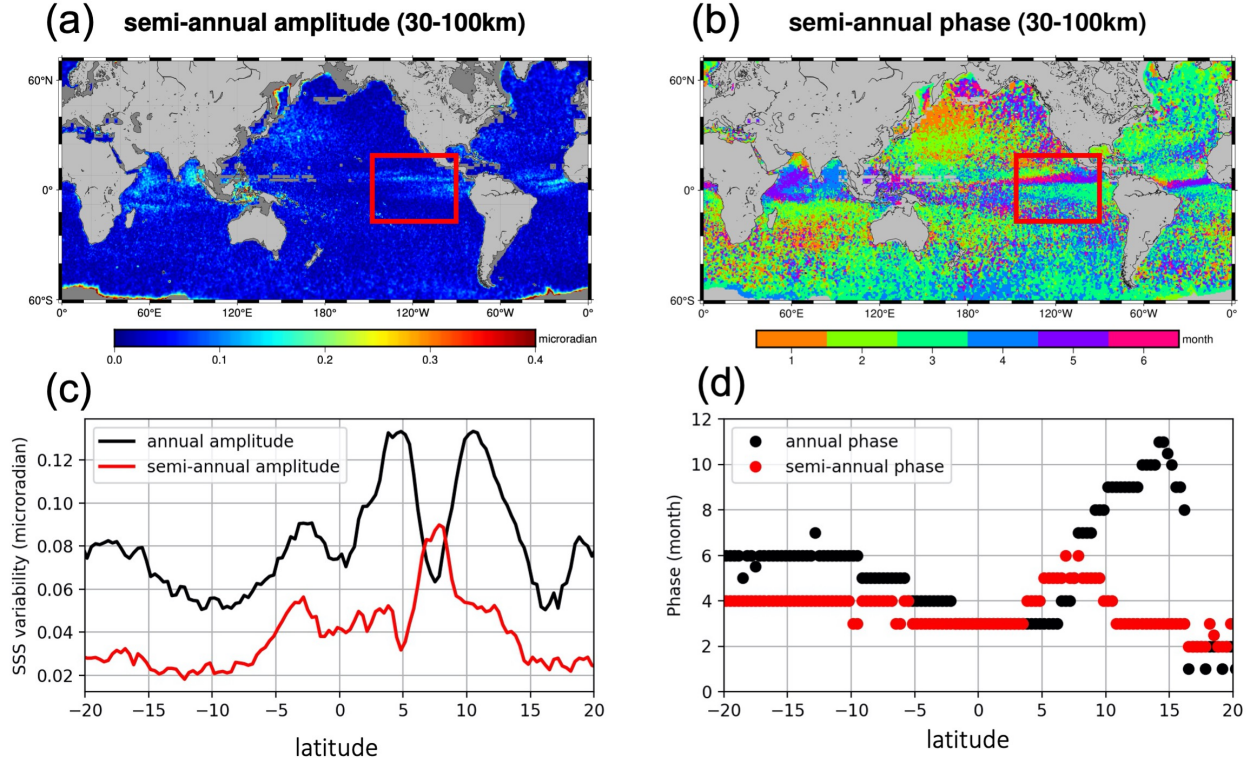


**Figure 4.4.** The amplitude (a) and phase (b) for semi-annual SSS variability in the 30-100 km wavelength band from satellite altimetry. Regions masked out are in gray. Panels (c) and (d) show the amplitude and phase along a meridional profile averaged over 150°W to 90°W as shown in the red boxes in (a) and (b).

### 4.3.3 Seasonality: Assessment

We next assess the success of our fitted seasonal cycles. We run the 5-parameter least-squares fitting with the assumption that the annual and semi-annual variations contain the majority of SSS variance and they undergo sinusoidal cycles. To evaluate the least-squares fitting, we adopt the metric of fraction of variance explained (FVE) (Colosi et al., Colosi et al.; Draper and Smith, 1998), defined as:

$$FVE = 1 - \frac{\sum_{i=1}^N (y_i - \hat{y}_i)^2}{\sum_{i=1}^N (y_i - \bar{y})^2} \quad (4.1)$$

where  $y_i$  is the  $i$ th observation,  $\hat{y}_i$  is the  $i$ th estimate, and  $\bar{y}$  is the mean value.  $N$  is

the number of total observations, which is 12 in this study. We assume that each estimate has the same uncertainty. The global maps of FVE for each sub-band of the SSS variability from satellite altimetry are provided in Figure 4.11 of the Appendix. In general, the percent of variance explained by the least-squares fit is high in regions of high variability and low in regions of small annual amplitude. SSS variability with shorter wavelengths is associated with higher FVE, indicating that the sub-mesoscale to mesoscale bands (30–100 km) are mostly governed by annual and semi-annual cycle processes. The complete set of plots showing the mean, the annual and semi-annual amplitudes of SSS variability using satellite altimetry data, as well as the FVE maps are provided in Figures 4.8, 4.11, 4.12, and 4.13 of the Appendix.

#### 4.3.4 Spectral analysis

In this section, in order to highlight different dynamical features, we present the PSD from satellite altimetry as well as time series in six selected regions. Table 1 summarizes representative statistics for the global median value of the mean, annual/semi-annual amplitude of the SSS variability, and the FVE in three wavelength bands: the 10–30 km band which is contaminated by waves; the 30–100 km submesoscale band; and the  $>100$  km mesoscale band. Table ?? allows magnitude comparisons between the annual, semi-annual, and mean SSS variability. Because we use different bandwidths, we avoid comparison across different wavelength bands. We find that the seasonal components are small: the annual amplitude is  $\sim 10\%$ , and semi-annual amplitude is  $\sim 4\%$  of the mean variability. The median FVE by the annual and semi-annual least-squares fit is 85.7% at the short wave band, then decreases to 58.0% at mesoscales. This means that mesoscale SSS variability is more complicated than a simple seasonal cycle.

**Table 4.1.** The Global Median Value of the Mean, the Annual/Semi-Annual Amplitude of the Sea Surface Slope Variability, and the Median Fraction of Variance Explained in Three Wavelength Bands.

SSS band (km)	Mean ( $\mu\text{rad}$ )	Annual ( $\mu\text{rad}$ )	Semi-annual ( $\mu\text{rad}$ )	FVE(%)
10-30	2.52	0.27	0.083	85.7%
30-100	0.91	0.096	0.036	79.0%
>100	0.65	0.057	0.037	58.0%

We discuss the seasonal PSD in six selected regions: the Kuroshio region ( $140^\circ/190^\circ/30^\circ/45^\circ$ ); the North Atlantic Ocean ( $320^\circ/350^\circ/56^\circ/66^\circ$ ); the California coast ( $23^\circ/239^\circ/29^\circ/42^\circ$ ); the Bay of Bengal ( $80^\circ/100^\circ/0^\circ/20^\circ$ ); the west of Australia ( $60^\circ/120^\circ/-45^\circ/-30^\circ$ ); and the Atlantic equatorial area ( $320^\circ/345^\circ/0^\circ/15^\circ$ ) and present the PSD in Figure 4.5. The six regions are selected to highlight a range of specific dynamical features: (a) there are consistent strong geostrophic currents over the Kuroshio region; (b) the Atlantic Ocean north of  $50^\circ\text{N}$  is associated with the largest thermocline depth change; (c) there are strong local winds in late boreal spring at the California coast; (d) the semi-annual SSS cycle dominates the Bay of Bengal; (e) the west of Australia demonstrates intense SSS variability and salinity change; (f) both the annual and semi-annual SSS cycles are strong in the Atlantic equatorial area.

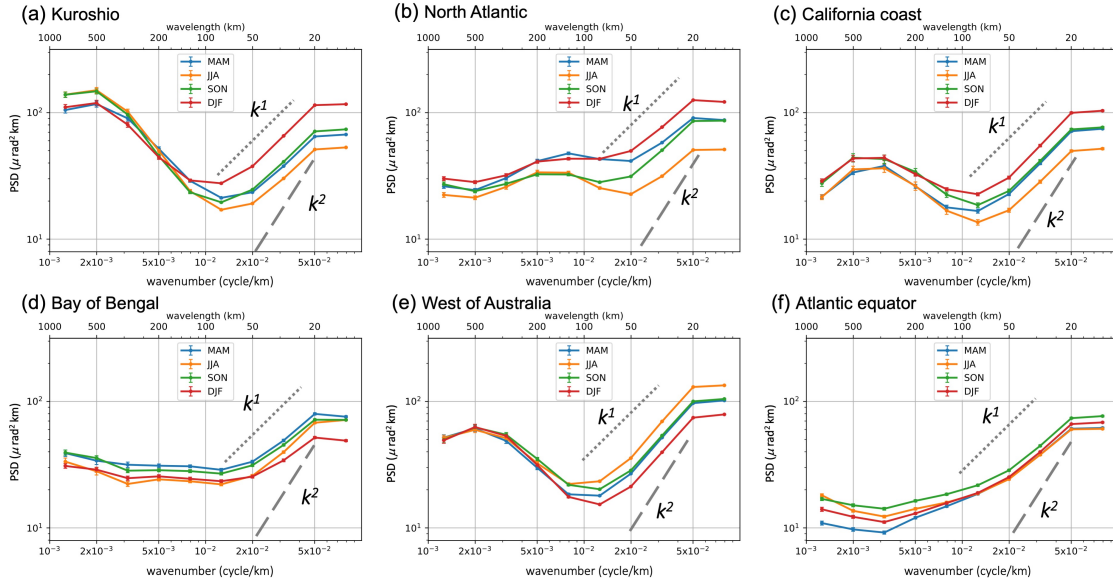


**Figure 4.5.** The PSD of the seasonal SSS variability in (a) the Kuroshio region; (b) the north Atlantic Ocean; (c) the California coast; (d) the Bay of Bengal; (e) the west of Australia; and (f) the Atlantic equatorial area. The 99% confidence intervals are provided at the center of each band. The  $k$  and  $k^2$  spectral slopes are indicated for reference.

We use 3-month intervals to compute the seasonal SSS variability, that is, December-January-February for winter, March-April-May for spring, June-Jul-August for summer, and September-October -November for fall in the Northern Hemisphere. For each wavelength band, we square the median value of the absolute seasonal SSS anomaly in the selected area, then divide it by the bandwidth to represent the seasonal PSD. The 10 wavelength sub-bands (10.00–15.84 km, 15.84–25.12 km, 25.12–39.81 km, 39.81–63.09 km, 63.09–100.00 km, 100.00–158.48 km, 158.48–251.18 km, 251.18–398.10 km, 398.10–630.95 km, and 630.95–1000.00 km) are equally spaced in the logscale wavenumber domain, and the band widths are larger at high wavenumbers. The result is shown in Figure 3.5, where PSD has units of  $\mu\text{rad}^2 \text{ km}$ . PSD does not depend on the choice of bandwidth, so we can compare the energy across different wavelengths. Error bars indicate the 99% confidence interval in the selected area, and the  $k$  and  $k^2$  spectral slopes are labeled in the 20–100 km range.

The six selected regions show blue spectra at high wavenumbers ( $> 10^{-2}$  cycles/km), which means that the SSS variability in the 30–100 km band is dominated by energy in the shortest wavelengths. The PSD of SSS in the 20–50 km wavelength range basically follows a  $k$  or even smaller spectral slope, which suggests a roughly  $k^{-1}$  SSH spectrum. This means that our data processing method has effectively reduced the white measurement noise in the satellite altimetry along-track observations. At high wavenumbers ( $> 10^{-2}$  cycles/km), the energy in general reaches a maximum in local winter and minimum in local summer (Figures 4.5a, 4.5b, 4.5c, and 4.5e). This agrees with Figure 4.2b showing that the annual cycles reach their maxima in local winter within the 30–100 km band with a few exceptions including the Bay of Bengal (Figure 4.5d). At the Bay of Bengal where semi-annual variability dominates, the energy is high in the boreal spring and fall. The Bay of Bengal also demonstrates higher energy in the summer at high wavenumbers ( $> 10^{-2}$  cycles/km), possibly under the influence of strong surface winds. The cross-season energy differences are smaller at low wavenumbers ( $< 10^{-2}$  cycles/km) in general.

### 4.3.5 Impacts from SWH

While the high correlation between SWH and SSS ( $< 30$  km) is suggestive of SWH noise leakage into the SSS variability, there are also good physical reasons why SSS variability could be correlated with SWH. Winds and wave heights are highly correlated. Surface gravity waves are generated by the friction between wind and water, and upper-ocean geostrophic currents are established in response to winds (e.g., Stommel, 1948). If both the SSS and SWH are responding to wind forcing then there should be a strong correlation in their time series. The thermocline depth as a secondary driving factor, as shown in Section 4.3.1, promotes SSS variability by storing potential energy, which can be converted to eddy kinetic energy (Callies et al., 2016; Qiu et al., 2014; Uchida et al., 2017). To further understand the impact from waves and the

thermocline depth, in Figure 4.6 we plot the normalized time series of the mean SSS variability in the 30–100 km wavelength band, SWH, WSP, and thermocline depths in the six regions as introduced in Section 4.3.4.

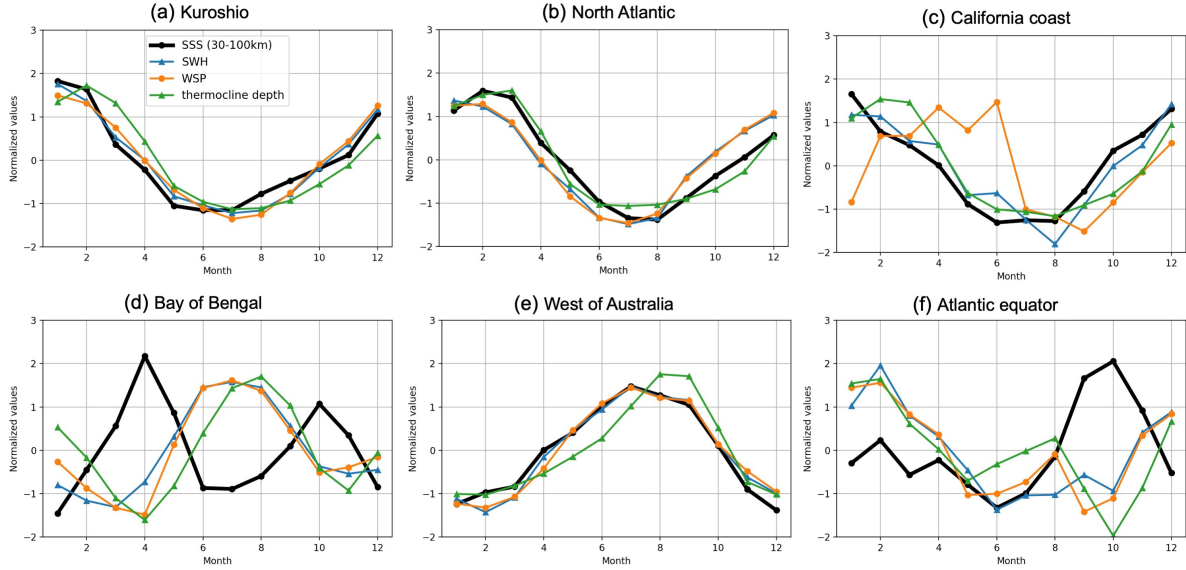


**Figure 4.6.** The normalized time series of the mean SSS variability (30-100 km, thick black line with rounds dots), SWH (blue line with triangle dots), WSP (orange line with round dots), and the thermocline depth (green line with triangle dots) in (a) the Kuroshio region; (b) the north Atlantic Ocean; (c) the California coast; (d) the Bay of Bengal; (e) the west of Australia; and (f) the Atlantic equatorial area.

For each region, we compare the time series of SSS variability (30–100 km) from satellite altimetry, SWH, WSP, and the thermocline depth. In the west of Australia, the SSS variability, SWH, and WSP undergo correlated annual cycles that peak in July (Figure 4.6e). The Kuroshio region (Figure 4.6a) and the North Atlantic Ocean (Figure 4.6b) show similar patterns except that there are phase differences between the SSS and SWH/WSP (leading/lagging by 1 month). In the Kuroshio region (Figure 4.6a), the thermocline depth leads the SSS by 1 month, which agrees with the numerical study of Dong et al. (2020). The Atlantic Ocean north of 50°N (Figure 4.6b) witnesses the largest thermocline depth annual cycle, reaching its minimum around July.

Shallower thermocline depths are hypothesized to be less effective at storing potential energy and thus less effective in promoting sea surface variability. This is consistent with the fact that SSS variability reaches its minimum 1 month afterward. Regions with weak thermocline depth changes may not be impacted as much and are thus not discussed here. The California coast experiences strong local winds in late spring, yet the SWH and SSS are not affected (Figure 4.6c). In the Bay of Bengal (Figure 4.6d), the SSS variability shows semi-annual cycles peaking in boreal spring and fall, while the SWH and WSP reach maxima in July. The anti-correlation indicates that winds and surface waves are not the sole drivers of the ocean sub-mesoscale variability, and local factors might have stronger influences. For example, the northern Bay of Bengal has strong submesoscale salinity variability, influenced by the Ganges-Brahmapputra River outflows (Gordon et al., 2016). This region is also influenced by the South Asian monsoon's semi-annual occurrence. The Atlantic equatorial area shows a strong SSS peak in October which is in phase neither with SWH nor with WSP. The different variability patterns between the SSS variability and SWH/WSP in the Bay of Bengal (Figure 4.6d) and the Atlantic equator (Figure 4.6f) indicate that surface waves/winds are not the only driving factor of the SSS variability. The different timing between SSS and SWH in the Kuroshio (Figure 4.6a) and the north Atlantic Ocean (Figure 4.6b) shows that there are real energetics in the upper ocean other than signal leakage from SWH in the 30–100 km wavelength band.

## 4.4 Discussion and Conclusions

Repeat-pass altimetry cannot resolve the small wavelength ( $<150$  km) spatial variations in ocean surface height/slope variability for three reasons: first, the smallest track spacing is  $\sim 80$  km (Envisat) at the equator; second, errors in the marine geoid/slope can dominate the residual SSH/SSS in the gaps between the repeat tracks; and third, ocean waves produce white noise in the SSH/SWH, known as a noise hump in the PSD of SSH, which commonly dominates the

signal at wavelengths  $< \sim 50$  km. Since 2014, the marine geoid/gravity community (Andersen and Knudsen, 2020; Li et al., 2022, Sandwell et al., 2019, Zhang et al., 2020) has been focused on improvements in spatial resolution and accuracy by addressing each of these issues. The quantity and quality of non-repeat and gap-filling altimeter data has increased dramatically with CryoSAT-2, Jason-1/2 geodetic phases, the SARAL/AltiKa geodetic mission, and the new repeat track of the Sentinel-3A/B satellites. In addition, the short-wavelength altimeter noise for the standard LRM products can be reduced to the noise level of the latest SAR mission products through 2-pass retracking (Garcia et al., 2014; Zhang and Sandwell, 2017) and careful editing. Of course, the recent launched SWOT altimeter mission will, hopefully, resolve 20 km spatial wavelengths at a high temporal sampling to reveal a wealth of new ocean dynamics (Fu and Uebelmann, 2014). Here we reprocessed the available repeat and non-repeat altimeter data, collected over the past 30 years, using the 2-step retracking to reduce the noise hump, to begin to resolve the small spatial patterns at a low temporal resolution (mean, 12, 6 months). We worked with the original trackline altimeter data, as residual SSS, to pre-whiten the red spectrum of the ocean dynamic signals which enables along-track, band-pass filtering.

Our overall analysis has 10 spatial bands between wavelengths of 10 and 1,000 km and three temporal bands: mean, annual, and semi-annual (i.e., 5 coefficients). In many cases, the individual bands have low signal-to-noise ratios so we combined the spatial bands into three groups. Spatial variations in mesoscale variability ( $> 100$  km wavelength) are discussed and analyzed in many previous publications (e.g., Qiu et al., 2014; Sasaki et al., 2017) so they are not repeated here. We showed through correlation analysis that SWH noise dominates the residual SSS between wavelengths of 10–30 km, so these bands are not considered further. The remaining bands from 30 to 100 km wavelength have sufficient signal-to-noise ratios to reveal new signals at mean, annual, and semi-annual timescales. The three sub-bands in the 30–100 km range (25–39 km, 39–63 km, and 63–100 km) all have similar spatial patterns, so they were combined to improve the recovery of the annual/semi-annual signals. We also calculate the



seasonal components of other wavelength bands (39–100 km and 50–100 km) and they show similar spatial patterns as the 30–100 km. Thus, we think that 30–100 km is a robust choice. The 30–100 km submesoscale band contains both unbalanced wave motions (internal tides/waves, near-inertial flows) and balanced geostrophic flows, and which one dominates is geographically dependent (Chen and Qiu, 2021; Chereskin et al., 2019; Qiu et al., 2017; Qiu et al., 2018).

#### **4.4.1 Interpretation of the Mean SSS**

The analysis of the long-term average of the SSS variability in the 30–100 km wavelength band is more completely discussed in a related publication (Yu et al., 2022), so only the highlights are discussed here. That study used a machine learning approach to rank the dominant environmental factors that influence the SSS variability over the 30–100 km band, which are distance to the nearest thermocline boundary, SWH, MDT, MDT gradient, seafloor roughness,  $M_2$  tidal speed,  $K_1$  tidal amplitude, and stratifications. The stratification is closely related to the thermocline depth. The correlation with the SWH and the thermocline depth, and especially the annual variations, will be discussed more completely below. In this study, we also investigate the annual and semi-annual variations (amplitude and phase) in SSS in the 30–100 km wavelength band. An initial finding is that the annual amplitude is one tenth the mean amplitude, and the semi-annual amplitude is 1/25th the mean amplitude. This makes the interpretation of these temporal signals both challenging and new.

#### **4.4.2 Interpretation of the Annual SSS**

One new finding of our seasonal analysis is that SSS variability is correlated with both the SWH and the thermocline depth. We expect there will be some SWH noise leakage into SSS at longer wavelengths ( $>30$  km). To address this issue, we present the spatial correlation between the SSS variability and SWH as well as the thermocline depth in Figure 4.7. The

SSS variability at smaller wavelengths is associated with more seasonal variability as summarized in Table 4.1. The correlations between annual components are higher compared to the mean components at short wavelengths ( $<100$  km), and lower at longer wavelengths ( $>100$  km). The correlation with thermocline depth is smaller compared to the correlation with SWH at sub-mesoscales ( $<100$  km), which supports Figure 4.3 result that the annual phase of the SSS variability agrees better with SWH. The differences in the annual phase (Figure 4.3) and the time series of SSS and SWH/WSP (Figure 4.6) indicate that the SSS variability (30–100 km) is not entirely driven by wind or surface waves, nor is it contaminated by SWH leakage. In the future, in situ measurements from wave buoys can help to evaluate the influence from SWH.

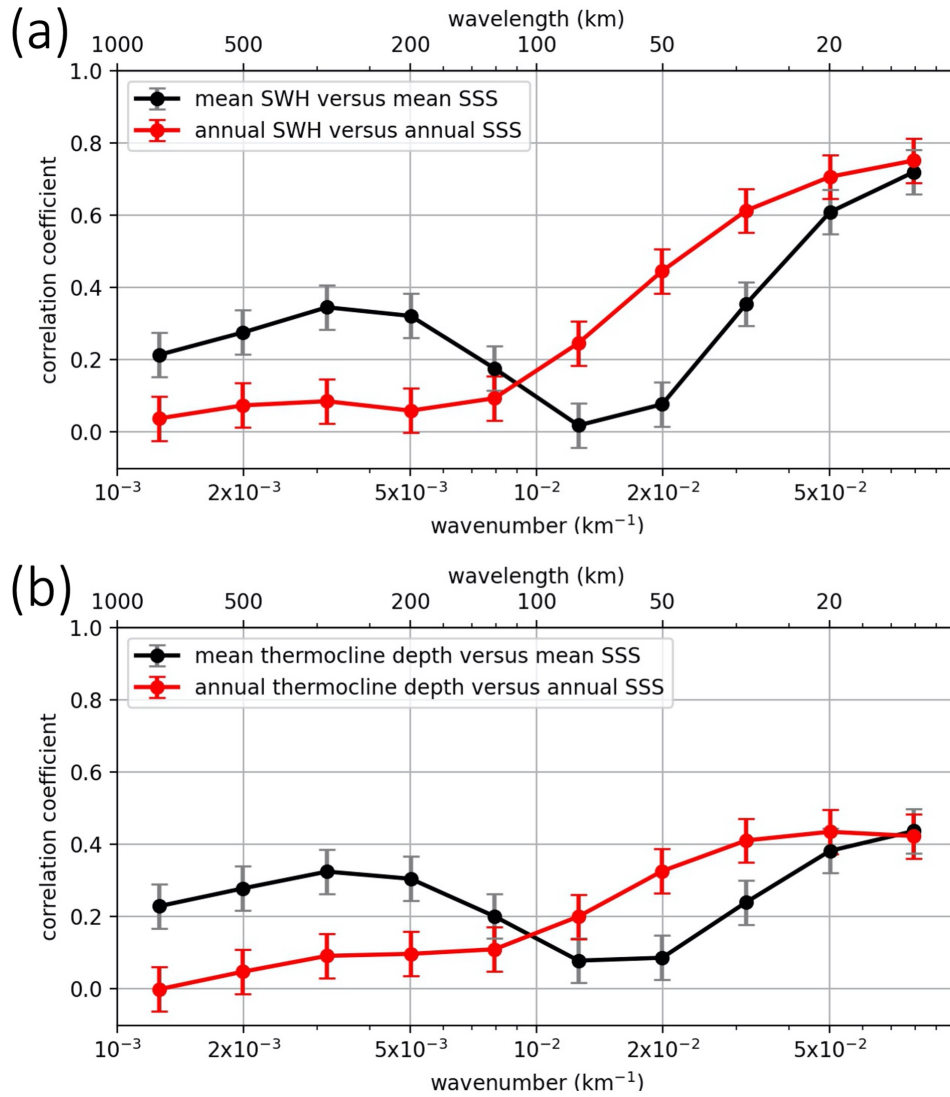


**Figure 4.7.** (a) Correlation between the mean SWH and mean band-pass filtered SSS (black curve); correlation between the annual amplitude of SWH and annual amplitude of the band-pass filtered SSS (red curve); (b) same as (a) but for the correlation between the thermocline depth and the SSS. Error bars indicate the 99% confidence interval.

There are two competing hypotheses for the influence of the thermocline depth on the ocean surface variability. One hypothesis predicts that the deeper thermocline associated with less stratified water stores more potential energy, which can be transferred to more eddy kinetic energy and create more small-scale surface motions (Callies et al., 2016; Qiu et al., 2014; Sasaki et al., 2014; Uchida et al., 2017). The second hypothesis is that shallower thermoclines have

thinner upper layers. Momentum from the atmosphere can be transferred to a thinner upper layer in a more effective way and make the ocean surface move faster (Peng et al., 2022). For geostrophic motions represented by SSS variability and for the time scales resolved in the altimeter record, our results support the first hypothesis that in the local winter when the thermocline is deeper, the SSS variability is stronger, though the thermocline depth is a secondary driving factor compared to the SWH. Baroclinic mixed-layer instabilities, arising from density gradients, can restratify the system and lead to turbulence, converting potential energy into eddy kinetic energy. In this study we focus on the seasonality in the 30-100 km spatial scale and our attention is not on any specific ocean activities in this band.

#### **4.4.3 Interpretation of the Semi-Annual SSS**

A significant new finding of our combined annual/semi-annual analysis is that there is an equatorial region of high SSS variability that essentially follows the atmospheric ITCZ. This signal is most prominent in the Pacific and Atlantic Oceans, where it appears as a north-south annual migration of the high variability bands. When this is modeled as combined annual and semi-annual signals, the two components have spatially orthogonal patterns. At the central latitude ( $\sim 7^\circ\text{N}$ ) where the SSS variability peak passes twice a year in June and December, the semi-annual amplitude is the largest; at the two boundaries ( $\sim 4^\circ\text{N}$  and  $\sim 11^\circ\text{N}$ ) where the peak passes once a year in February–March and August–September, separately, there are strong annual signals. We propose that this pattern is related to the seasonal marine ITCZ shift, driven by interhemispheric solar heating differences and the cross-equatorial atmospheric energy heating (Bischoff and Schneider, 2016). The interannual migration of the ITCZ is related to El Niño-Southern Oscillation (Bischoff and Schneider, 2016), which modulates the sea surface temperature at interannual scales, but our analysis has not been constructed to analyze interannual time scales.

#### 4.4.4 Future Work Needed to Resolve These Issues

The SWOT wide-swath altimetry mission, which was launched in late 2022, will characterize the ocean sub-mesoscale activities at spatial scales larger than 20 km and answer some fundamental questions about the formation and dynamics of sub-mesoscale activities and ocean circulation (Fu and Ubelmann, 2014). But wave-related errors (sea state bias, aliasing, wind-driven activities, etc.) will still be a major issue that SWOT has to face. SWOT's an initial phase of 90 1-day repeats will allows us to evaluate the along-track and cross-track slope accuracy over wellcharted, large seamounts (i.e., Foundation seamounts, South Pacific), where we have a mean SSS model with accuracy better than  $1 \mu\text{rad}$  at wavelengths at a 10 km wavelength resolution. We expect the accuracy will primarily depend on the SWH, and studying the accuracy under different wave conditions will help us to understand the influence of wave-related errors.

### 4.5 Acknowledgements

This work was supported by the NASA SWOT program (NNX16AH64G and NNX16AH67G) the NASA Ocean Surface Topography Science Team (NNX17AH53G) and the Office of Naval Research (N00014-17-1-2866). The Generic Mapping Tools (GMT) (Wessel et al., 2013) were extensively used in data processing. We appreciate the discussion with Saulo Muller Soares and Duncan Agnew, and the internal review feedback from Teresa Chereskin.

The sea surface slope and significant wave height data are available through:

<https://doi.org/10.5281/zenodo.7311420> The surface wind speed data are from:

<https://www.remss.com/measurements/ccmp/> The thermocline depth data are from:

<http://mixedlayer.ucsd.edu/> The llc4320 model output is downloaded using the python llcreader module (<https://xmitgcm.readthedocs.io/en/latest/llcreader.html>) via the ECCO data portal:

[https://data.nas.nasa.gov/ecco/data.php?dir=/eccodata/llc\\_4320](https://data.nas.nasa.gov/ecco/data.php?dir=/eccodata/llc_4320)



## 4.6 Appendix

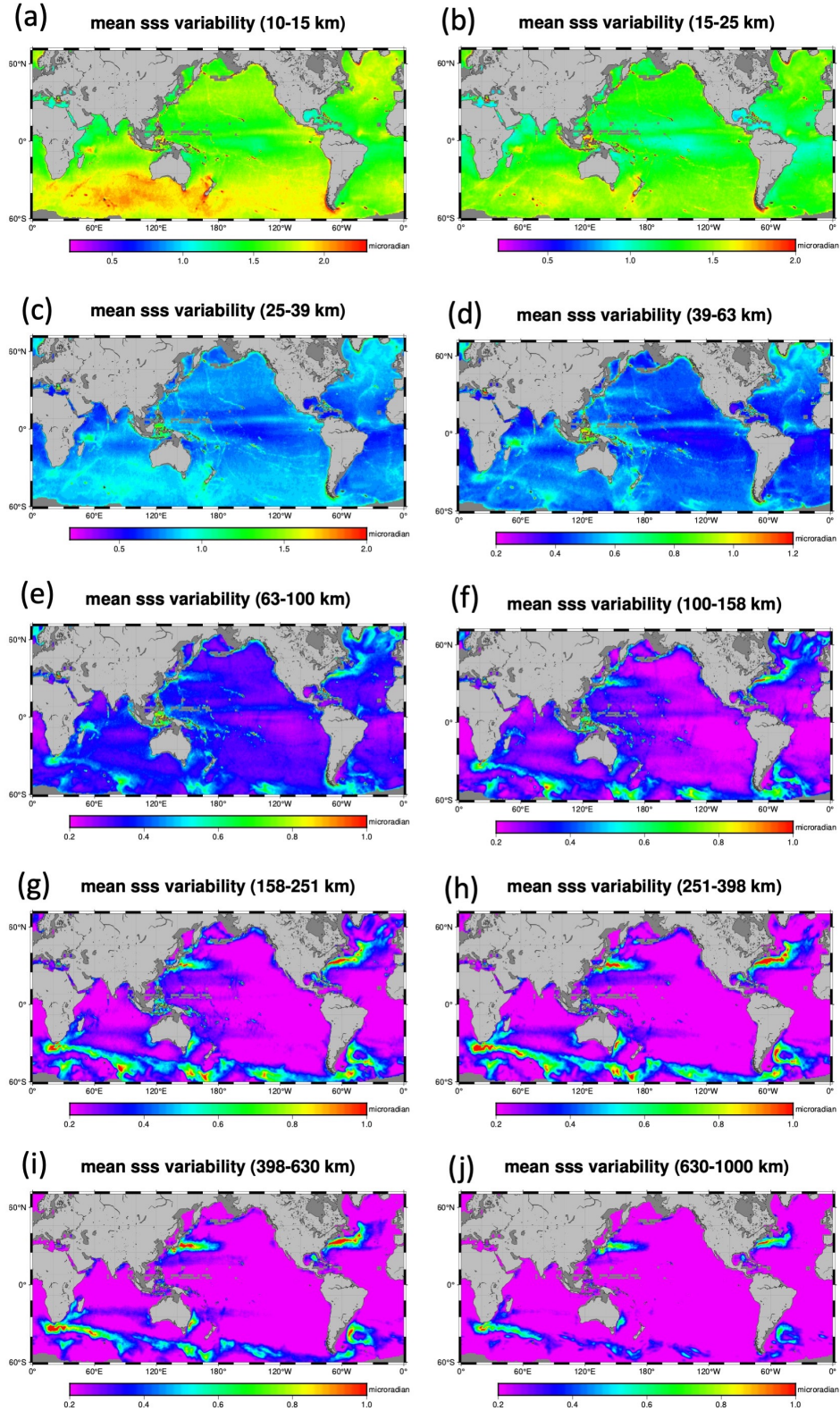


**Figure 4.8.** Mean SSS variability in the 10 sub-bands.

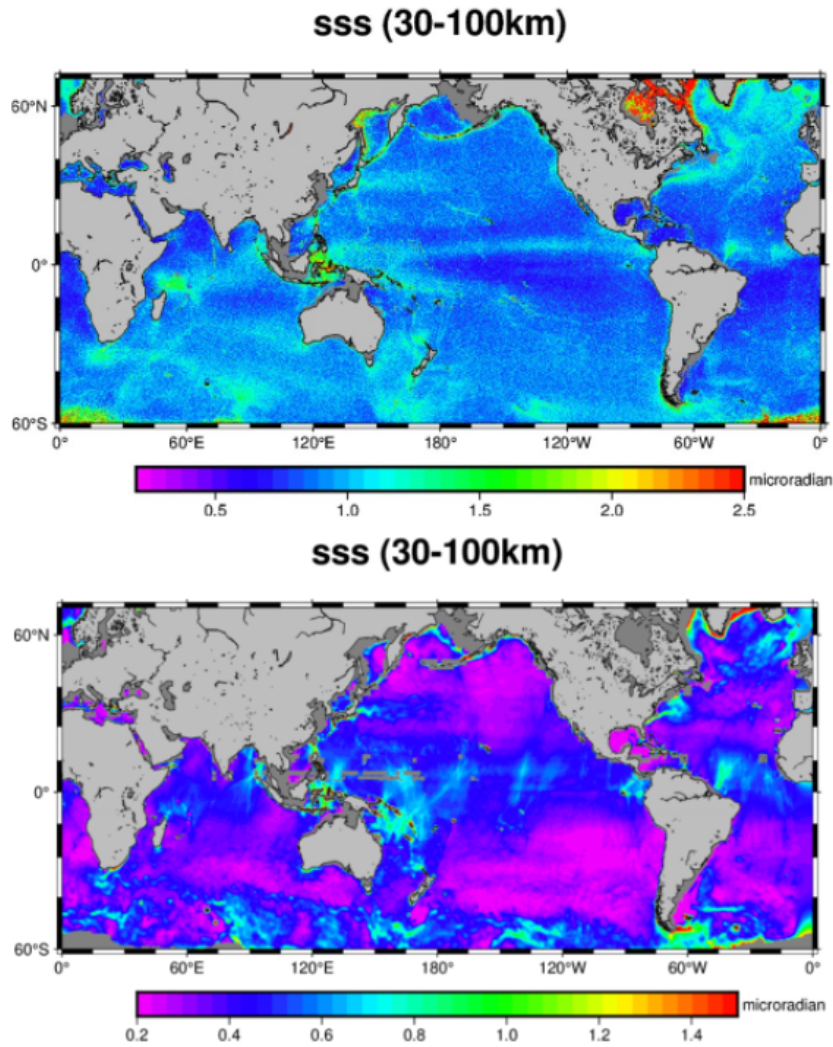


**Figure 4.9.** The mean SSS variability in the 30-100 km wavelength band from (a) multi-year satellite altimetry along track data and (b) llc4320. The color scales are different. Llc4320 shows much smaller signals in general. Both show high variabilities in the western boundary currents, the north Atlantic ocean, and highly-stratified zones by river flows (Amazon outlet, Gulf of Bengal). Satellite altimetry shows strong variabilities over rough topography (Hawaiian Seamount chains, Mid-Atlantic Ocean Ridge) and the ITCZ which are missing in the llc4320. Llc4320 shows strong variability in several regions on the Pacific equatorial area (longitude centers are around 165° E, 165° W, 135° W) that are invisible in the satellite altimetry results.



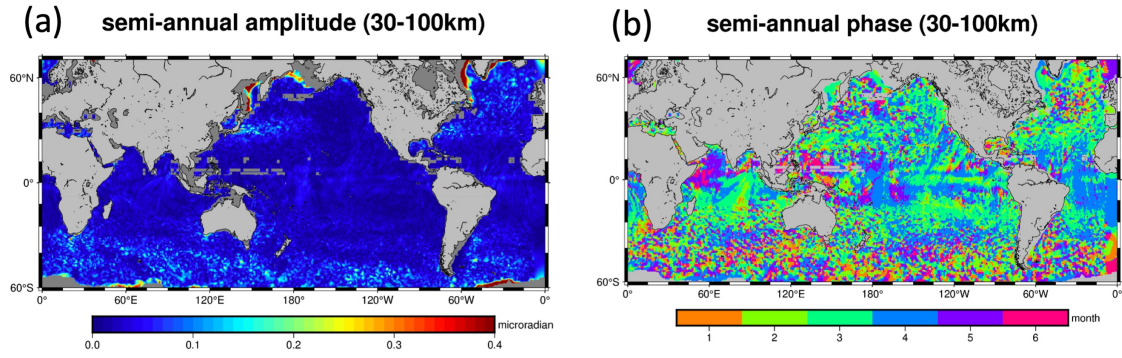


**Figure 4.10.** The semi-annual (a) amplitude and (b) phase of the SSS variability from 30 km to 100km wavelength bands using llc4320 model outputs.

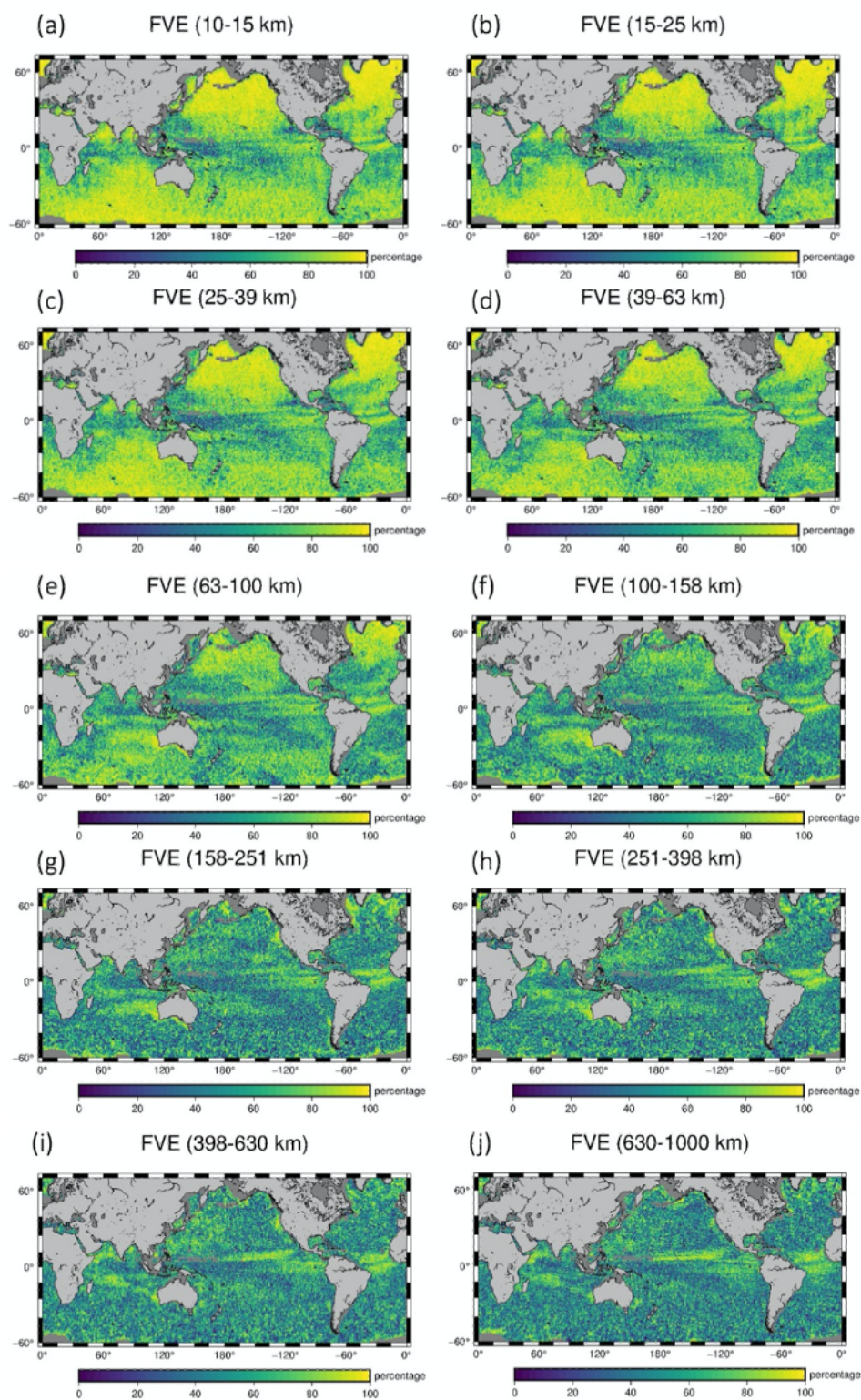


**Figure 4.11.** Fractions of variance explained by the annual and semi-annual least-squares fit for 10 sub-bands.



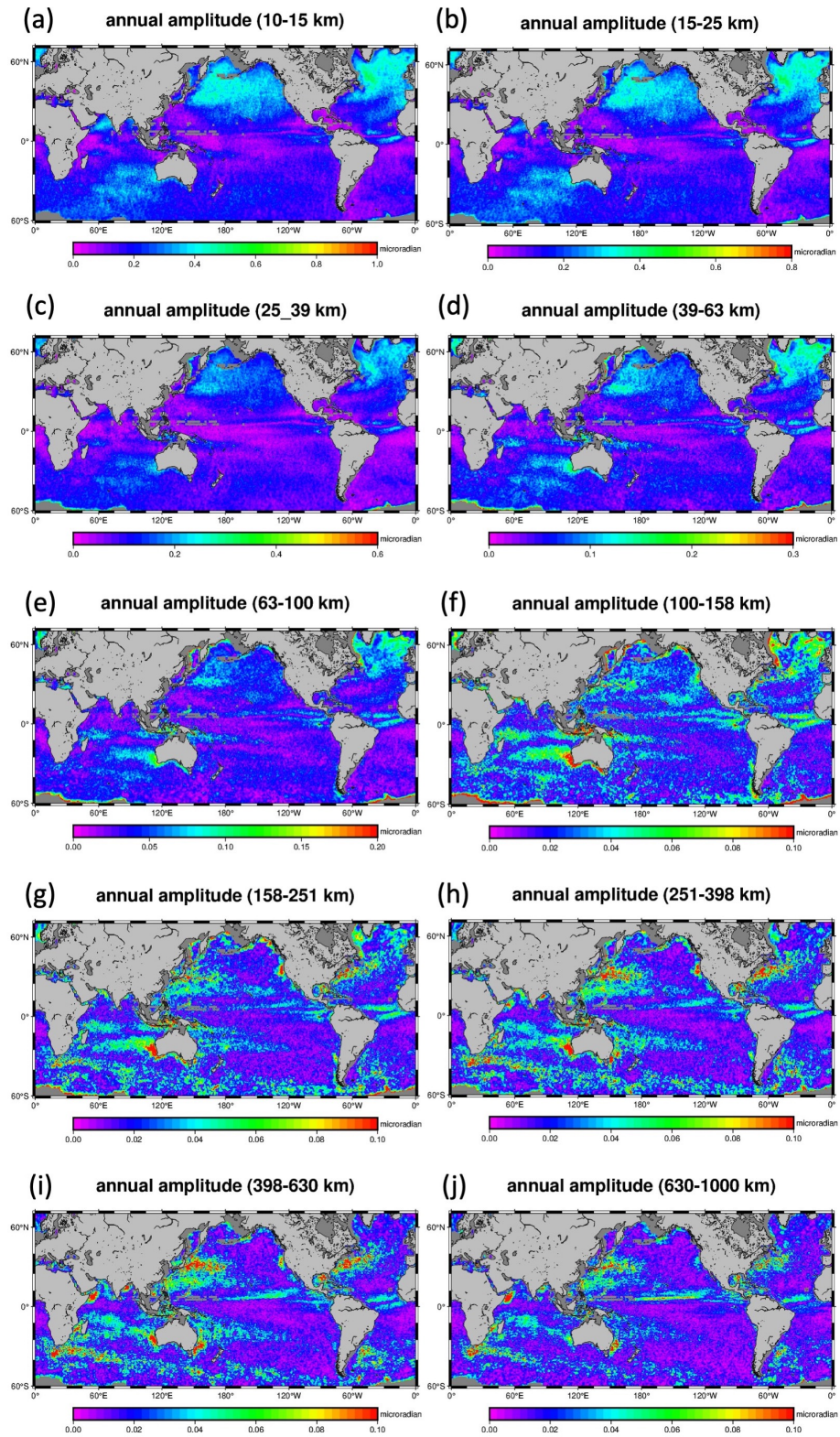


**Figure 4.12.** The annual amplitudes of SSS variability in the 10 sub-bands. Note the reduction in the color scale as the wavelength band increases.

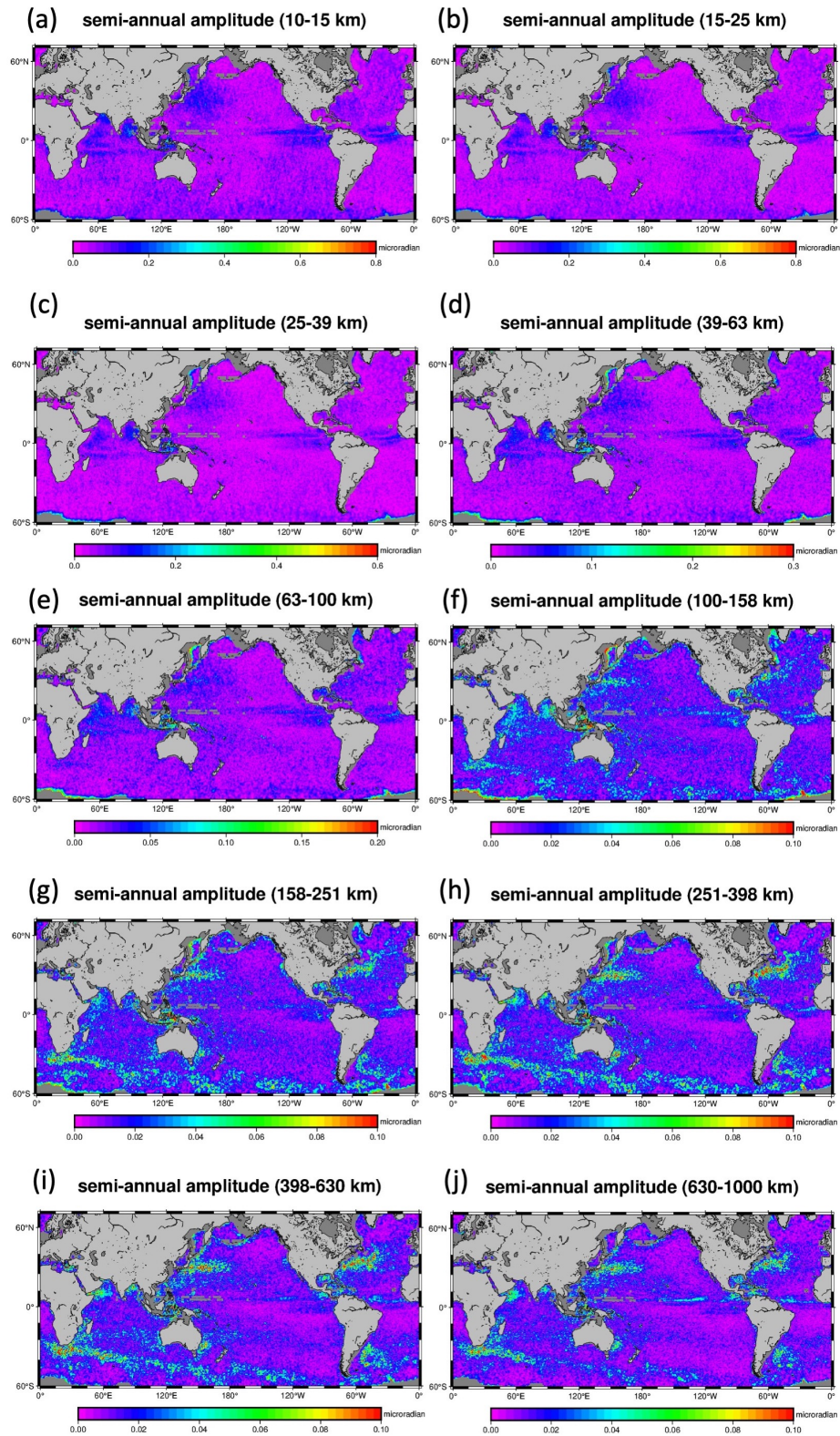


**Figure 4.13.** The semi-annual amplitudes of SSS variability in the 10 sub-bands.



# Chapter 5

## Future work

This chapter introduces two future projects. One is to investigate SWOT data to be collected over the Foundation Seamounts in the South Pacific during the “fast sampling” phase. The other is to study the tidal conversion rate over rough topography.

### **5.1 High-resolution small-scale variability at the Foundation Seamounts from SWOT**

#### **5.1.1 First glimps of SWOT images**

SWOT was launched on December 16, 2022 from Vandenberg Space Force Base, California, and has since entered the commissioning phase for engineering checkout and adjustment. During this phase, an issue was encountered with KaRIn’s power amplifier shutdown, which was later resolved by turning on the cold unit. In April 2023, SWOT moved into the “fast-sampling” phase, where specific areas are revisited once per day for calibration and validation purposes. Following the 1-day repeat phase, SWOT will enter the operational phase, which is expected to last 3 years. During this phase, SWOT will have a 21-day repeat orbit to balance global coverage and frequent sampling. On March 24, 2023, the SWOT team released the first images of the KaRIn data, revealing ocean currents such as the Gulf Stream in unprecedented detail (Figures 5.1 and 5.2).

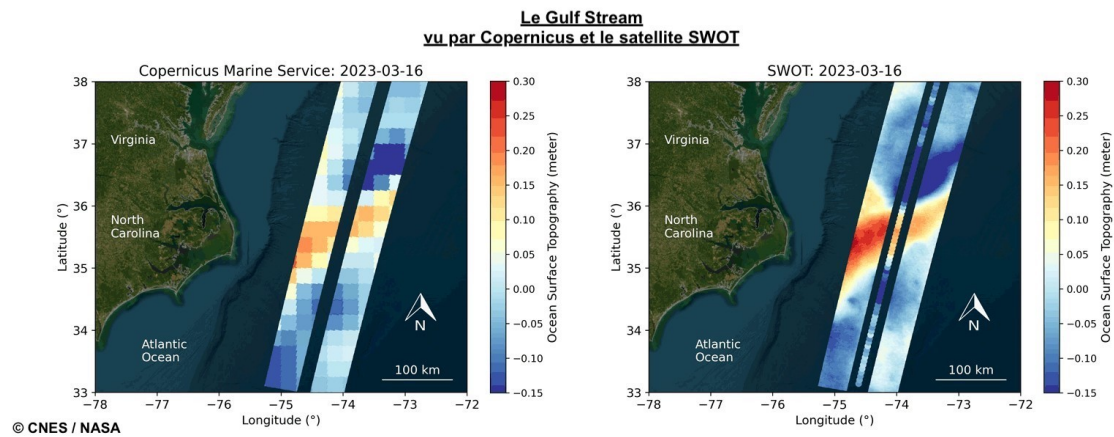


**Figure 5.1.** Sea level data gathered March 16, 2023 in the Gulf Stream by SWOT’s KaRIn instrument, visualized at right, has 10 times the spatial resolution of data taken over the same area by altimeters on seven other satellites, visualized at left. Red represents sea levels higher than the global average, while blue is lower. Credit: left: NASA/JPL-Caltech/Copernicus Marine Service of ESA; right: NASA/JPL-Caltech.

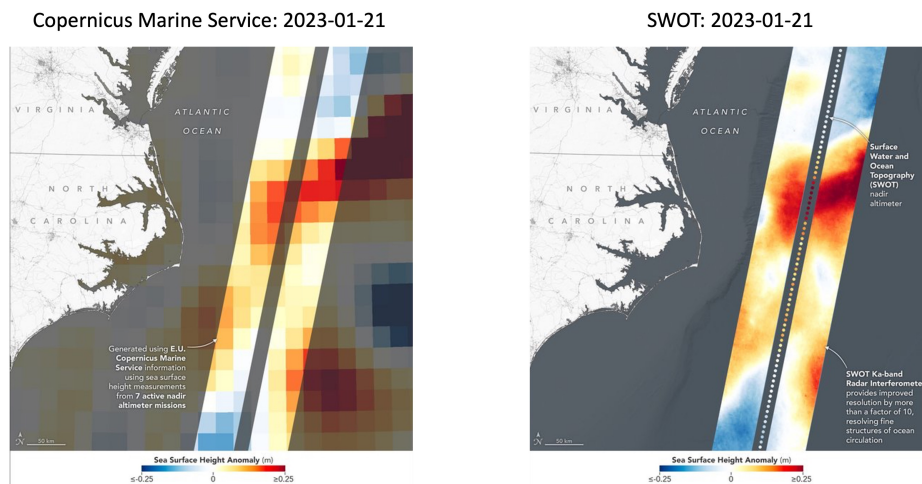


**Figure 5.2.** Same as Figure 5.1 but collected in January 21, 2023. Credit: left: NASA/JPL-Caltech/Copernicus Marine Service of ESA; right: NASA/JPL-Caltech.

The SWOT ocean measurements have a spatial resolution that is 10 times higher than the composite of sea surface height data collected over the same area by seven other satellites,

including Sentinel-6 Michael Freilich, Jason-3, Sentinel-3A and 3B, Cryosat-2, SARAL/Altika, and Hai Yang 2B. The pixel size for SWOT is 2 km by 2km and early images show that SWOT is able to recover the marine gravity field at better than  $\sim 16$  km wavelength.

### **5.1.2 Foundation Seamounts investigation plan**

We aim to investigate SWOT data collected over the Foundation Seamounts in the South Pacific (as shown in Figure 5.3a) during the “fast sampling” phase. This analysis is crucial for our SWOT investigation and serves as an essential validation site for SWOT. Our primary focus is on the crossover point at  $\sim 35^\circ\text{S}$  in the South Pacific region, where ocean SSS variability is relatively low ( $\text{RMS} < 1 \mu\text{rad}$ ). This remote region has several vast seamounts that were initially identified using Seasat and Geosat altimetry data (Mammerickx, 1992) and later surveyed by French scientists aboard the RV L’Atlante in 1997 (Maia et al., 2000). The complete multibeam coverage has enabled us to construct a sea surface slope model with an accuracy of better than  $1 \mu\text{rad}$  at wavelengths as small as 10 km (Figure Figure 5.3b).

We will evaluate the along-track and across-track slope from SWOT as a function of the number of repeats, using the known small-scale signal. Our primary expectation is that the accuracy of the SWOT data will depend on SWH. If SWOT can achieve better than  $1 \mu\text{rad}$  accuracy at 10 km wavelength resolution, it will have the potential to detect all uncharted seamounts in the ocean taller than 1 km. This estimated number is more than 100,000 (Wessel, 2001). Furthermore, this study will provide a significant improvement in the resolution of detailed tectonics of ocean basins and better bathymetric estimation, which is the ultimate focus of our investigation.

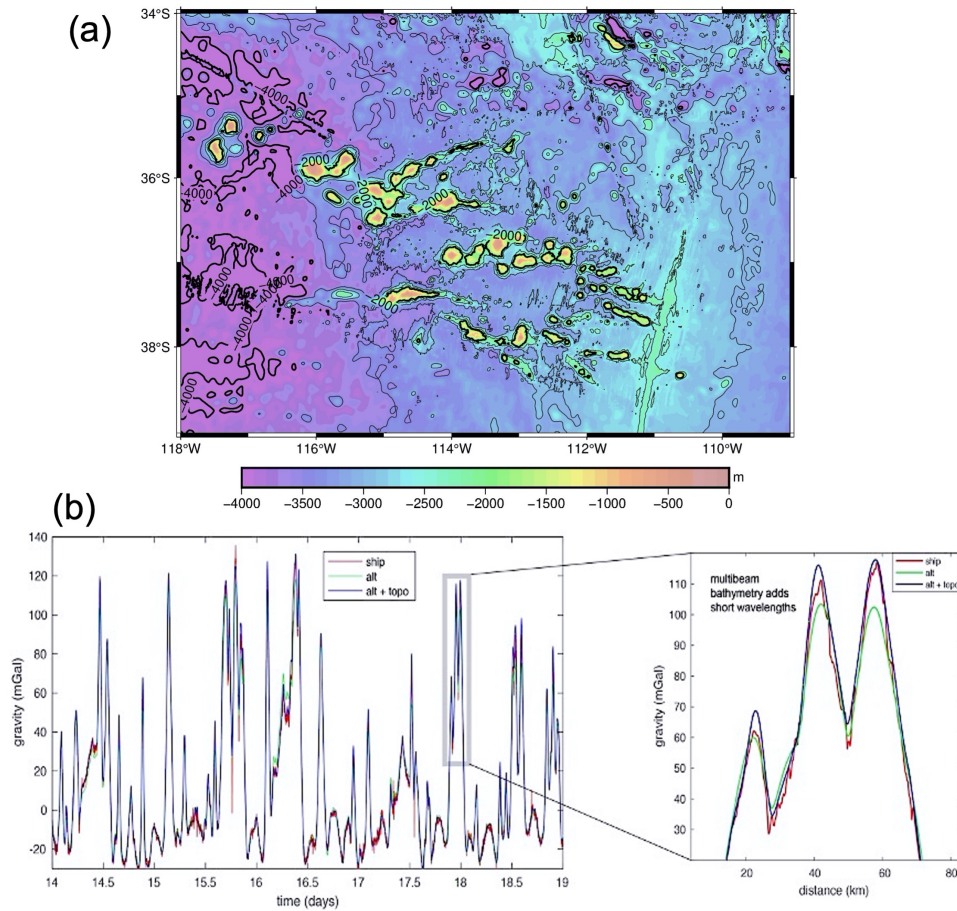


**Figure 5.3.** Bathymetry of Foundation seamounts first mapped in 1997 using multibeam sonar (a) and shipboard gravity (b) (Maia et al., 2000). Many of these seamounts are more than 3000 m tall and produce gravity anomalies (b) and sea surface slopes of more than 100 mGal and 100  $\mu$ rad, respectively. The satellite-derived gravity (green) does not completely resolve the shipboard gravity (red) at the tops of the seamounts. The full amplitude gravity (and SSS) can be reconstructed using a combination of altimeter-derived gravity for wavelengths  $> 40$  km and gravity calculated from the multibeam bathymetry for the shorter wavelengths (blue). Note the very small spatial scale wiggles in the ship data are errors due to unmodeled ship motions.

## 5.2 Tidal conversion over rough topography

### 5.2.1 Motivation

The conversion from barotropic ocean tides to internal tides is a classic geophysical problem (Bell, 1975a; Bell, 1975b; Llewellyn Smith and Young, 2002). When a tide sloshes over an uneven bottom in stratified ocean, it transfers energy from the spin of the Earth into internal



gravity waves. This tidal conversion process plays a vital role in mixing the deep ocean and energy exchange. By investigating the one-day repeat from the SWOT mission over the Foundation Seamounts, which have depths as shallow as 600 meters, we can gain new insights into the interaction between tidal flow and these large structures (Noble and Mullineaux, 1989; Gerkema and Van Haren, 2007; Zeiden et al.. The tidal flow may be evident in the small-scale residual SSS related to oceanographic processes. Since SWOT has the ability to detect small-scale ocean variability down to approximately 16 km, internal tides, particularly the non-stationary internal tides, pose a significant challenge. We believe that that this research will aid in the interpretation of SWOT data.

### **5.2.2 Research plan**

In our treatment of the tidal conversion problem, we assume a simple harmonic flow over a stratified fluid with non-uniform stratification in a realistic ocean bottom with finite depth. We follow the analytic estimate proposed by Llewellyn Smith and Young (2002) and keep the three approximations to simplify the situation: (i) hydrostatic approximations; (ii) small topography amplitude assumption; (iii) quasistatic limit.

The major questions we have are:

1. What is the global barotropic tidal conversion energy estimate using an updated synthetic bathymetry model (SYNBATH; Sandwell et al., 2022) and the FES2014 tide model (Lyard et al., 2021)?
2. To what extent is it affected by uncertainties in tidal directions?
3. To what extent is it affected by different modelings of seamounts and ridges?

We will calculate the tidal conversion rate over the global ocean and do sensitivity tests to help understand the above questions. We will also extract hourly and the aliased daily output from the MITgcm llc4320 1/48 degree model (Marshall et al., 1997b; Adcroft et al., 2004) as well as the one-day repeat data from SWOT to study the tidal propagation over the Foundation Seamounts.

# Bibliography

- Alistair Adcroft, Jean-Michel Campin, Chris Hill, and John Marshall. Implementation of an atmosphere–ocean general circulation model on the expanded spherical cube. *Monthly Weather Review*, 132(12):2845–2863, 2004.
- TR Akylas, Roger HJ Grimshaw, Simon R Clarke, and Ali Tabaei. Reflecting tidal wave beams and local generation of solitary waves in the ocean thermocline. *Journal of Fluid Mechanics*, 593:297–313, 2007.
- OB Andersen and P Knudsen. The dtu17 global marine gravity field: First validation results. In *Fiducial Reference Measurements for Altimetry: Proceedings of the International Review Workshop on Satellite Altimetry Cal/Val Activities and Applications*, pages 83–87. Springer, 2020.
- Ole Andersen, P Knudsen, S Kenyon, JK Factor, and S Holmes. Global gravity field from recent satellites (dtu15)—arctic improvements. *First Break*, 35(12), 2017.
- Ole B Andersen and Per Knudsen. Dnsc08 mean sea surface and mean dynamic topography models. *Journal of Geophysical Research: Oceans*, 114(C11), 2009.
- Brian K Arbic, James G Richman, Jay F Shriver, Patrick G Timko, E Joseph Metzger, and Alan J Wallcraft. Global modeling of internal tides: Within an eddying ocean general circulation model. *Oceanography*, 25(2):20–29, 2012.
- Randi A Arinaga and Kwok Fai Cheung. Atlas of global wave energy from 10 years of reanalysis and hindcast data. *Renewable Energy*, 39(1):49–64, 2012.
- Robert Atlas, Ross N Hoffman, Joseph Ardizzone, S Mark Leidner, Juan Carlos Jusem, Deborah K Smith, and Daniel Gombos. A cross-calibrated, multiplatform ocean surface wind velocity product for meteorological and oceanographic applications. *Bulletin of the American Meteorological Society*, 92(2):157–174, 2011.
- Jerôme Aucan and Fabrice Ardhuin. Infragravity waves in the deep ocean: An upward revision. *Geophysical Research Letters*, 40(13):3435–3439, 2013.

- Maxime Ballarotta, Clément Ubelmann, Marie-Isabelle Pujol, Guillaume Taburet, Florent Fournier, Jean-François Legeais, Yannice Faugère, Antoine Delepoulle, Dudley Chelton, Gérald Dibarboure, et al. On the resolutions of ocean altimetry maps. *Ocean Science*, 15(4): 1091–1109, 2019.
- Joseph J Becker and David T Sandwell. Global estimates of seafloor slope from single-beam ship soundings. *Journal of Geophysical Research: Oceans*, 113(C5), 2008.
- TH Bell. Lee waves in stratified flows with simple harmonic time dependence. *Journal of Fluid Mechanics*, 67(4):705–722, 1975a.
- TH Bell. Topographically generated internal waves in the open ocean. *Journal of Geophysical Research*, 80(3):320–327, 1975b.
- Julius S Bendat and Allan G Piersol. *Random data: analysis and measurement procedures*. John Wiley & Sons, 2011.
- Tobias Bischoff and Tapio Schneider. The equatorial energy balance, itcz position, and double-itz bifurcations. *Journal of Climate*, 29(8):2997–3013, 2016.
- Jörn Callies and Weiguang Wu. Some expectations for submesoscale sea surface height variance spectra. *Journal of Physical Oceanography*, 49(9):2271–2289, 2019.
- Jörn Callies, Glenn Flierl, Raffaele Ferrari, and Baylor Fox-Kemper. The role of mixed-layer instabilities in submesoscale turbulence. *Journal of Fluid Mechanics*, 788:5–41, 2016.
- Loren Carrère, F Lyard, M Cancet, A Guillot, N Picot, et al. Fes 2014, a new tidal model—validation results and perspectives for improvements. In *Proceedings of the ESA living planet symposium*, pages 9–13, 2016.
- Eric P Chassignet, Linda T Smith, George R Halliwell, and Rainer Bleck. North atlantic simulations with the hybrid coordinate ocean model (hycom): Impact of the vertical coordinate choice, reference pressure, and thermobaricity. *Journal of Physical Oceanography*, 33(12): 2504–2526, 2003.
- Arun Chawla, Deanna Spindler, and Hendrik Tolman. 30 year wave hindcasts using wavewatch iii with cfsr winds, phase 1. *NOAA/NWS/NCEP/MMAB. Maryl. USA*, 23, 2012.
- Shuiming Chen and Bo Qiu. Sea surface height variability in the 30–120 km wavelength band from altimetry along-track observations. *Journal of Geophysical Research: Oceans*, 126(4): e2021JC017284, 2021.
- Teresa K Chereskin, Cesar B Rocha, Sarah T Gille, Dimitris Menemenlis, and Marcello Passaro. Characterizing the transition from balanced to unbalanced motions in the southern california

- current. *Journal of Geophysical Research: Oceans*, 124(3):2088–2109, 2019.
- Luke V Colosi, Ana B Villas Bôas, and Sarah T Gille. The seasonal cycle of significant wave height in the ocean: Local versus remote forcing. *Journal of Geophysical Research: Oceans*, 126(8):e2021JC017198, 2021.
- S Desai, LL Fu, S Cherchali, and P Vaze. Surface water and ocean topography mission (swot) project science requirements document. *NASA/JPL technical document D–61923 Revision B*, 29, 2018.
- Jay L Devore. *Probability and Statistics for Engineering and the Sciences*. Cengage learning, 2011.
- G Dibarboure, F Boy, JD Desjonqueres, S Labroue, Y Lasne, N Picot, JC Poisson, and P Thibaut. Investigating short-wavelength correlated errors on low-resolution mode altimetry. *Journal of Atmospheric and Oceanic Technology*, 31(6):1337–1362, 2014.
- Guillaume Dodet, Jean-François Piolle, Yves Quilfen, Saleh Abdalla, Mickaël Accensi, Fabrice Ardhuin, Ellis Ash, Jean-Raymond Bidlot, Christine Gommenginger, Gwendal Marechal, et al. The sea state cci dataset v1: towards a sea state climate data record based on satellite observations. *Earth System Science Data*, 12(3):1929–1951, 2020.
- Jihai Dong, Baylor Fox-Kemper, Hong Zhang, and Changming Dong. The seasonality of submesoscale energy production, content, and cascade. *Geophysical Research Letters*, 47(6):e2020GL087388, 2020.
- Norman R Draper and Harry Smith. *Applied regression analysis*, volume 326. John Wiley & Sons, 1998.
- Kyla Drushka, William E Asher, Janet Sprintall, Sarah T Gille, and Clifford Hoang. Global patterns of submesoscale surface salinity variability. *Journal of Physical Oceanography*, 49(7):1669–1685, 2019.
- Raffaele Ferrari and Carl Wunsch. Ocean circulation kinetic energy: Reservoirs, sources, and sinks. *Annual Review of Fluid Mechanics*, 41:253–282, 2009.
- Lee-Lueng Fu and Anny Cazenave. *Satellite altimetry and earth sciences: a handbook of techniques and applications*. Elsevier, 2000.
- Lee-Lueng Fu and Clement Ubelmann. On the transition from profile altimeter to swath altimeter for observing global ocean surface topography. *Journal of Atmospheric and Oceanic Technology*, 31(2):560–568, 2014.
- Lee-Lueng Fu, Dudley B Chelton, Pierre-Yves Le Traon, and Rosemary Morrow. Eddy dynamics

- from satellite altimetry. *Oceanography*, 23(4):14–25, 2010.
- Emmanuel S Garcia, David T Sandwell, and Walter HF Smith. Retracking cryosat-2, envisat and jason-1 radar altimetry waveforms for improved gravity field recovery. *Geophysical Journal International*, 196(3):1402–1422, 2014.
- David García-García and Caroline C Ummenhofer. Multidecadal variability of the continental precipitation annual amplitude driven by amo and enso. *Geophysical Research Letters*, 42(2): 526–535, 2015.
- Chris Garrett and Eric Kunze. Internal tide generation in the deep ocean. *Annu. Rev. Fluid Mech.*, 39:57–87, 2007.
- T Gerkema and H Van Haren. Internal tides and energy fluxes over great meteor seamount. *Ocean Science*, 3(3):441–449, 2007.
- Julie Gevorgian, David Sandwell, Yao Yu, Seung-Sep Kim, and Paul Wessel. Global distribution and morphology of seamounts. In *AGU Fall Meeting Abstracts*, volume 2021, pages T45D–0273, 2021.
- Sarah T Gille, Mara M Yale, and David T Sandwell. Global correlation of mesoscale ocean variability with seafloor roughness from satellite altimetry. *Geophysical Research Letters*, 27(9):1251–1254, 2000.
- John A Goff. Global prediction of abyssal hill root-mean-square heights from small-scale altimetric gravity variability. *Journal of Geophysical Research: Solid Earth*, 115(B12), 2010.
- John A Goff. Identifying characteristic and anomalous mantle from the complex relationship between abyssal hill roughness and spreading rates. *Geophysical Research Letters*, 47(11): e2020GL088162, 2020.
- Arnold L Gordon, Emily L Shroyer, Amala Mahadevan, Debasis Sengupta, and Mara Freilich. Bay of bengal: 2013 northeast monsoon upper-ocean circulation. *Oceanography*, 29(2):82–91, 2016.
- Marijan Grgić and Tomislav Bašić. Radar satellite altimetry in geodesy-theory, applications and recent developments. *Geodetic Sciences-Theory, Applications and Recent Developments*, 2021.
- Dennis L Hartmann. *Global physical climatology*, volume 103. Newnes, 2015.
- Dan Hendrycks and Kevin Gimpel. A baseline for detecting misclassified and out-of-distribution examples in neural networks. *arXiv preprint arXiv:1610.02136*, 2016.

- James Holte, Lynne D Talley, John Gilson, and Dean Roemmich. An argo mixed layer climatology and database. *Geophysical Research Letters*, 44(11):5618–5626, 2017.
- Guolin Ke, Qi Meng, Thomas Finley, Taifeng Wang, Wei Chen, Weidong Ma, Qiwei Ye, and Tie-Yan Liu. Lightgbm: A highly efficient gradient boosting decision tree. *Advances in neural information processing systems*, 30, 2017.
- Bradley W Klotz, Amy Neuenschwander, and Lori A Magruder. High-resolution ocean wave and wind characteristics determined by the icesat-2 land surface algorithm. *Geophysical Research Letters*, 47(1):e2019GL085907, 2019.
- Athanasios Koutavas and Jean Lynch-Stieglitz. Variability of the marine itcz over the eastern pacific during the past 30,000 years: Regional perspective and global context. *The Hadley circulation: Present, past and future*, pages 347–369, 2004.
- Albion Lawrence and Jörn Callies. Seasonality and spatial dependence of mesoscale and submesoscale ocean currents from along-track satellite altimetry. *Journal of Physical Oceanography*, 52(9):2069–2089, 2022.
- PY Le Traon and G Dibarboure. Mesoscale mapping capabilities of multiple-satellite altimeter missions. *Journal of Atmospheric and Oceanic Technology*, 16(9):1208–1223, 1999.
- PY Le Traon, F Nadal, and N Ducet. An improved mapping method of multisatellite altimeter data. *Journal of atmospheric and oceanic technology*, 15(2):522–534, 1998.
- Zhen Li, Jinyun Guo, Bing Ji, Xiaoyun Wan, and Shengjun Zhang. A review of marine gravity field recovery from satellite altimetry. *Remote Sensing*, 14(19):4790, 2022.
- Shiyu Liang, Yixuan Li, and Rayadurgam Srikant. Enhancing the reliability of out-of-distribution image detection in neural networks. *arXiv preprint arXiv:1706.02690*, 2017.
- Stefan G Llewellyn Smith and WR Young. Conversion of the barotropic tide. *Journal of Physical Oceanography*, 32(5):1554–1566, 2002.
- Nicholas R Lomb. Least-squares frequency analysis of unequally spaced data. *Astrophysics and space science*, 39:447–462, 1976.
- Iossif D Lozovatsky, Eugene G Morozov, and HJS Fernando. Spatial decay of energy density of tidal internal waves. *Journal of Geophysical Research: Oceans*, 108(C6), 2003.
- Florent H Lyard, Damien J Allain, Mathilde Cancet, Loren Carrère, and Nicolas Picot. Fes2014 global ocean tide atlas: design and performance. *Ocean Science*, 17(3):615–649, 2021.
- Asle Lygre and Harald E Krogstad. Maximum entropy estimation of the directional distribution

- in ocean wave spectra. *Journal of Physical Oceanography*, 16(12):2052–2060, 1986.
- M Maia, R Hékinian, D Ackermann, A Dehghani, P Gente, D Naar, J O’Connor, K Perrot, J Phipps Morgan, G Ramillien, et al. The foundation seamounts-pacific antarctic ridge interaction: A case study of a ridge approaching a hotspot. *Marine Geology*, 167:61–84, 2000.
- J Mammerickx. The foundation seamounts: tectonic setting of a newly discovered seamount chain in the south pacific. *Earth and planetary science letters*, 113(3):293–306, 1992.
- Karen M Marks and Richard V Sailor. Comparison of geos-3 and seasat altimeter resolution capabilities. *Geophysical research letters*, 13(7):697–700, 1986.
- KM Marks and WHF Smith. An evaluation of publicly available global bathymetry grids. *Marine Geophysical Researches*, 27:19–34, 2006.
- John Marshall, Alistair Adcroft, Chris Hill, Lev Perelman, and Curt Heisey. A finite-volume, incompressible navier stokes model for studies of the ocean on parallel computers. *Journal of Geophysical Research: Oceans*, 102(C3):5753–5766, 1997b.
- Nikolai A Maximenko, Bohyun Bang, and Hideharu Sasaki. Observational evidence of alternating zonal jets in the world ocean. *Geophysical research letters*, 32(12), 2005.
- Trevor J McDougall and Paul M Barker. Getting started with teos-10 and the gibbs seawater (gsw) oceanographic toolbox. *Scor/Iapso WG*, 127(532):1–28, 2011.
- Dimitris Menemenlis, Jean-Michel Campin, Patrick Heimbach, Chris Hill, Tong Lee, An Nguyen, Michael Schodlok, and Hong Zhang. Ecco2: High resolution global ocean and sea ice data synthesis. *Mercator Ocean Quarterly Newsletter*, 31(October):13–21, 2008.
- Amelie Meyer, Bernadette M Sloyan, Kurt L Polzin, Helen E Phillips, and Nathaniel L Bindoff. Mixing variability in the southern ocean. *Journal of Physical Oceanography*, 45(4):966–987, 2015.
- JH Morison, D Hancock, S Dickinson, J Robbins, L Roberts, R Kwok, SP Palm, B Smith, and MF Jasinski. Atlas/icesat-2 l3a ocean surface height, version 1. *Boulder Colo. USA NASA Natl. Snow Ice Data Cent. Distrib. Act. Arch. Cent*, 2019.
- Eugene Morozov. *Internal tides. Global field of internal tides and mixing caused by internal tides*. Springer, 2006.
- Rosemary Morrow, Lee-Lueng Fu, Fabrice Ardhuin, Mounir Benkiran, Bertrand Chapron, Emmanuel Cosme, Francesco d’Ovidio, J Thomas Farrar, Sarah T Gille, Guillaume Lapeyre, et al. Global observations of fine-scale ocean surface topography with the surface water and ocean topography (swot) mission. *Frontiers in Marine Science*, 6:232, 2019.



- R Dietmar Müller, Sabin Zahirovic, Simon E Williams, John Cannon, Maria Seton, Dan J Bower, Michael G Tetley, Christian Heine, Eline Le Breton, Shaofeng Liu, et al. A global plate model including lithospheric deformation along major rifts and orogens since the triassic. *Tectonics*, 38(6):1884–1907, 2019.
- Robert S Nerem, Brian D Beckley, John T Fasullo, Benjamin D Hamlington, Dallas Masters, and Gary T Mitchum. Climate-change–driven accelerated sea-level rise detected in the altimeter era. *Proceedings of the national academy of sciences*, 115(9):2022–2025, 2018.
- Amy L Neuenschwander and Lori A Magruder. The potential impact of vertical sampling uncertainty on icesat-2/atlas terrain and canopy height retrievals for multiple ecosystems. *Remote Sensing*, 8(12):1039, 2016.
- TA Neumann, A Brenner, D Hancock, J Robbins, J Saba, K Harbeck, A Gibbons, J Lee, SB Luthcke, T Rebold, et al. Atlas/icesat-2 12a global geolocated photon data, version 3. *Boulder, CO: NASA National Snow and Ice Data Center Distributed Active Archive Center*. Retrieved from, 10, 2020.
- Marlene Noble and Lauren S Mullineaux. Internal tidal currents over the summit of cross seamount. *Deep Sea Research Part A. Oceanographic Research Papers*, 36(12):1791–1802, 1989.
- Sam Partee, Matthew Ellis, Alessandro Rigazzi, Andrew E Shao, Scott Bachman, Gustavo Marques, and Benjamin Robbins. Using machine learning at scale in numerical simulations with smartsim: An application to ocean climate modeling. *Journal of Computational Science*, 62:101707, 2022.
- Ananda Pascual, Yannice Faugère, Gilles Larnicol, and Pierre-Yves Le Traon. Improved description of the ocean mesoscale variability by combining four satellite altimeters. *Geophysical Research Letters*, 33(2), 2006.
- Fabian Pedregosa, Gaël Varoquaux, Alexandre Gramfort, Vincent Michel, Bertrand Thirion, Olivier Grisel, Mathieu Blondel, Peter Prettenhofer, Ron Weiss, Vincent Dubourg, et al. Scikit-learn: Machine learning in python. *the Journal of machine Learning research*, 12:2825–2830, 2011.
- Qihua Peng, Shang-Ping Xie, Dongxiao Wang, Rui Xin Huang, Gengxin Chen, Yeqiang Shu, Jia-Rui Shi, and Wei Liu. Surface warming–induced global acceleration of upper ocean currents. *Science Advances*, 8(16):eabj8394, 2022.
- Bo Qiu, Shuiming Chen, Patrice Klein, Hideharu Sasaki, and Yoshikazu Sasai. Seasonal mesoscale and submesoscale eddy variability along the north pacific subtropical countercurrent. *Journal of Physical Oceanography*, 44(12):3079–3098, 2014.

- Bo Qiu, Toshiya Nakano, Shuiming Chen, and Patrice Klein. Submesoscale transition from geostrophic flows to internal waves in the northwestern pacific upper ocean. *Nature Communications*, 8(1):14055, 2017.
- Bo Qiu, Shuiming Chen, Patrice Klein, Jinbo Wang, Hector Torres, Lee-Lueng Fu, and Dimitris Menemenlis. Seasonality in transition scale from balanced to unbalanced motions in the world ocean. *Journal of Physical Oceanography*, 48(3):591–605, 2018.
- J. Ross Quinlan. Induction of decision trees. *Machine learning*, 1:81–106, 1986.
- Heidi Rannal, Ole B Andersen, and Per Knudsen. Global and regional evaluation of the first year of sentinel-3: Possibilities and challenges for mss determination. In *Fiducial Reference Measurements for Altimetry: Proceedings of the International Review Workshop on Satellite Altimetry Cal/Val Activities and Applications*, pages 89–96. Springer, 2020.
- Cesar B Rocha, Sarah T Gille, Teresa K Chereskin, and Dimitris Menemenlis. Seasonality of submesoscale dynamics in the kuroshio extension. *Geophysical Research Letters*, 43(21): 11–304, 2016.
- Kshudiram Saha. *Tropical circulation systems and monsoons*. Springer Science & Business Media, 2009.
- Claude Sammut and Geoffrey I Webb. *Encyclopedia of machine learning*. Springer Science & Business Media, 2011.
- David T Sandwell. *Advanced Geodynamics*. Cambridge University Press, 2022.
- David T Sandwell and Walter HF Smith. Retracking ers-1 altimeter waveforms for optimal gravity field recovery. *Geophysical Journal International*, 163(1):79–89, 2005.
- David T Sandwell and Walter HF Smith. Slope correction for ocean radar altimetry. *Journal of Geodesy*, 88(8):765–771, 2014.
- David T Sandwell, R Dietmar Müller, Walter HF Smith, Emmanuel Garcia, and Richard Francis. New global marine gravity model from cryosat-2 and jason-1 reveals buried tectonic structure. *Science*, 346(6205):65–67, 2014.
- David T Sandwell, Hugh Harper, Brook Tozer, and Walter HF Smith. Gravity field recovery from geodetic altimeter missions. *Advances in Space Research*, 68(2):1059–1072, 2019.
- David T Sandwell, John A Goff, Julie Gevorgian, Hugh Harper, Seung-Sep Kim, Yao Yu, Brook Tozer, Paul Wessel, and Walter HF Smith. Improved bathymetric prediction using geological information: Synbath. *Earth and Space Science*, 9(2):e2021EA002069, 2022.

- Martin Saraceno, Christine Provost, and Uriel Zajaczkovski. Long-term variation in the anti-cyclonic ocean circulation over the zapiola rise as observed by satellite altimetry: Evidence of possible collapses. *Deep Sea Research Part I: Oceanographic Research Papers*, 56(7): 1077–1092, 2009.
- Hideharu Sasaki, Patrice Klein, Bo Qiu, and Yoshikazu Sasai. Impact of oceanic-scale interactions on the seasonal modulation of ocean dynamics by the atmosphere. *Nature communications*, 5(1):1–8, 2014.
- Hideharu Sasaki, Patrice Klein, Yoshikazu Sasai, and Bo Qiu. Regionality and seasonality of submesoscale and mesoscale turbulence in the north pacific ocean. *Ocean Dynamics*, 67: 1195–1216, 2017.
- Anna C Savage, Brian K Arbic, Matthew H Alford, Joseph K Ansong, J Thomas Farrar, Dimitris Menemenlis, Amanda K O’Rourke, James G Richman, Jay F Shriver, Gunnar Voet, et al. Spectral decomposition of internal gravity wave sea surface height in global models. *Journal of Geophysical Research: Oceans*, 122(10):7803–7821, 2017.
- Jeffrey D Scargle. Studies in astronomical time series analysis. ii-statistical aspects of spectral analysis of unevenly spaced data. *Astrophysical Journal, Part 1, vol. 263, Dec. 15, 1982, p. 835-853.*, 263:835–853, 1982.
- P Schaeffer, MI Pujol, Y Faugere, E Charles, D Sandwell SIO, Q Dagneaux CELAD, R Baghi EUROGICIEL, and G Dibarboure. What do we need to improve the next mean sea surface. In *Ocean Surface Topography Science Team Meeting, Ponta Delgado, Portugal*, 2018.
- Andreas Schiller and Gary B Brassington. *Operational oceanography in the 21st century*. Springer Science & Business Media, 2011.
- Maria Seton, R Dietmar Müller, Sabin Zahirovic, Simon Williams, Nicky M Wright, John Cannon, Joanne M Whittaker, Kara J Matthews, and Rebecca McGirr. A global data set of present-day oceanic crustal age and seafloor spreading parameters. *Geochemistry, Geophysics, Geosystems*, 21(10):e2020GC009214, 2020.
- Alexander F Shchepetkin and James C McWilliams. The regional oceanic modeling system (roms): a split-explicit, free-surface, topography-following-coordinate oceanic model. *Ocean modelling*, 9(4):347–404, 2005.
- Anirban Sinha and Ryan Abernathey. Estimating ocean surface currents with machine learning. *Frontiers in Marine Science*, 8:672477, 2021.
- Ben Smith, Helen A Fricker, Alex S Gardner, Brooke Medley, Johan Nilsson, Fernando S Paolo, Nicholas Holschuh, Susheel Adusumilli, Kelly Brunt, Bea Csatho, et al. Pervasive ice sheet mass loss reflects competing ocean and atmosphere processes. *Science*, 368(6496):1239–1242,

2020.

Walter HF Smith and David T Sandwell. Global sea floor topography from satellite altimetry and ship depth soundings. *Science*, 277(5334):1956–1962, 1997.

Maïke Sonnewald, Redouane Lguensat, Daniel C Jones, Peter D Dueben, Julien Brajard, and Venkatramani Balaji. Bridging observations, theory and numerical simulation of the ocean using machine learning. *Environmental Research Letters*, 16(7):073008, 2021.

Louis St. Laurent and Chris Garrett. The role of internal tides in mixing the deep ocean. *Journal of Physical Oceanography*, 32(10):2882–2899, 2002.

Detlef Stammer, RD Ray, Ole Baltazar Andersen, BK Arbic, W Bosch, L Carrère, Yongcun Cheng, DS Chinn, BD Dushaw, GD Egbert, et al. Accuracy assessment of global barotropic ocean tide models. *Reviews of geophysics*, 52(3):243–282, 2014.

Henry Stommel. The westward intensification of wind-driven ocean currents. *Eos, Transactions American Geophysical Union*, 29(2):202–206, 1948.

Justin E Stopa. Seasonality of wind speeds and wave heights from 30 years of satellite altimetry. *Advances in Space Research*, 68(2):787–801, 2019.

Eivind Olavson Straume, Carmen Gaina, Sergei Medvedev, Katharina Hochmuth, Karsten Gohl, Joanne M Whittaker, Rader Abdul Fattah, Johannes Cornelis Doornenbal, and John R Hopper. Globbed: Updated total sediment thickness in the world’s oceans. *Geochemistry, Geophysics, Geosystems*, 20(4):1756–1772, 2019.

Harald Ulrik Sverdrup and Walter Heinrich Munk. *Wind, sea and swell: Theory of relations for forecasting*. Number 601. Hydrographic Office, 1947.

Guillaume Taburet, Antonio Sanchez-Roman, Maxime Ballarotta, Marie-Isabelle Pujol, Jean-François Legeais, Florent Fournier, Yannice Faugere, and Gerald Dibarboure. Duacs dt2018: 25 years of reprocessed sea level altimetry products. *Ocean Science*, 15(5):1207–1224, 2019.

Michel Tchilibou, Lionel Gourdeau, Rosemary Morrow, Guillaume Serazin, Bughsin Djath, and Florent Lyard. Spectral signatures of the tropical pacific dynamics from model;? xmltex\break? and altimetry: a focus on the meso-/submesoscale range. *Ocean Science*, 14(5):1283–1301, 2018.

Hector S Torres, Patrice Klein, Dimitris Menemenlis, Bo Qiu, Zhan Su, Jinbo Wang, Shuiming Chen, and Lee-Lueng Fu. Partitioning ocean motions into balanced motions and internal gravity waves: A modeling study in anticipation of future space missions. *Journal of Geophysical Research: Oceans*, 123(11):8084–8105, 2018.

- Brook Tozer, David T Sandwell, Walter HF Smith, C Olson, JR Beale, and P Wessel. Global bathymetry and topography at 15 arc sec: Srtm15+. *Earth and Space Science*, 6(10):1847–1864, 2019.
- Takaya Uchida, Ryan Abernathey, and Shafer Smith. Seasonality of eddy kinetic energy in an eddy permitting global climate model. *Ocean Modelling*, 118:41–58, 2017.
- Oscar Vergara, Rosemary Morrow, Isabelle Pujol, Gérald Dibarboure, and Clément Ubelmann. Revised global wave number spectra from recent altimeter observations. *Journal of Geophysical Research: Oceans*, 124(6):3523–3537, 2019.
- Ana B Villas Bôas, Sarah T Gille, Matthew R Mazloff, and Bruce D Cornuelle. Characterization of the deep water surface wave variability in the california current region. *Journal of Geophysical Research: Oceans*, 122(11):8753–8769, 2017.
- Paul Wessel. Global distribution of seamounts inferred from gridded geosat/ers-1 altimetry. *Journal of Geophysical Research: Solid Earth*, 106(B9):19431–19441, 2001.
- Paul Wessel, Walter HF Smith, Remko Scharroo, Joaquim Luis, and Florian Wobbe. Generic mapping tools: improved version released. *Eos, Transactions American Geophysical Union*, 94(45):409–410, 2013.
- Anne-Cathrin Wöfl, Helen Snaith, Sam Amirebrahimi, Colin W Devey, Boris Dorschel, Vicki Ferrini, Veerle AI Huvenne, Martin Jakobsson, Jennifer Jencks, Gordon Johnston, et al. Seafloor mapping—the challenge of a truly global ocean bathymetry. *Frontiers in Marine Science*, page 283, 2019.
- Yongsheng Xu and Lee-Lueng Fu. The effects of altimeter instrument noise on the estimation of the wavenumber spectrum of sea surface height. *Journal of Physical Oceanography*, 42(12):2229–2233, 2012.
- Mara M Yale, David T Sandwell, and Walter HF Smith. Comparison of along-track resolution of stacked geosat, ers 1, and topex satellite altimeters. *Journal of Geophysical Research: Solid Earth*, 100(B8):15117–15127, 1995.
- Ian R Young. *Wind generated ocean waves*. Elsevier, 1999.
- Yao Yu, Sarah T Gille, David T Sandwell, and Julian McAuley. Global mesoscale ocean variability from multiyear altimetry: An analysis of the influencing factors. *Artificial Intelligence for the Earth Systems*, 1(3):e210008, 2022.
- Edward D Zaron and Robert DeCarvalho. Identification and reduction of retracker-related noise in altimeter-derived sea surface height measurements. *Journal of Atmospheric and Oceanic Technology*, 33(1):201–210, 2016.

- Kristin L Zeiden, Daniel L Rudnick, and Jennifer A MacKinnon. Glider observations of a mesoscale oceanic island wake. *Journal of Physical Oceanography*, 49(9):2217–2235, 2019.
- Shengjun Zhang and David T Sandwell. Retracking of saral/altika radar altimetry waveforms for optimal gravity field recovery. *Marine Geodesy*, 40(1):40–56, 2017.
- Shengjun Zhang, David T Sandwell, Taoyong Jin, and Dawei Li. Inversion of marine gravity anomalies over southeastern china seas from multi-satellite altimeter vertical deflections. *Journal of Applied Geophysics*, 137:128–137, 2017.
- Shengjun Zhang, Jiancheng Li, Taoyong Jin, and Defu Che. Assessment of radar altimetry correction slopes for marine gravity recovery: A case study of jason-1 gm data. *Journal of Applied Geophysics*, 151:90–102, 2018.
- Shengjun Zhang, Ole Baltazar Andersen, Xiangxue Kong, and Hang Li. Inversion and validation of improved marine gravity field recovery in south china sea by incorporating hy-2a altimeter waveform data. *Remote Sensing*, 12(5):802, 2020.
- Zhengguang Zhang and Bo Qiu. Evolution of submesoscale ageostrophic motions through the life cycle of oceanic mesoscale eddies. *Geophysical Research Letters*, 45(21):11–847, 2018.